

UNIVERSITÉ DU QUÉBEC

**MÉMOIRE PRÉSENTÉ À
L'UNIVERSITÉ DU QUÉBEC À CHICOUTIMI
COMME EXIGENCE PARTIELLE
DU DOCTORAT EN INGÉNIERIE**

**PAR
MOHAMMAD SHAKIBA**

**EFFET DES ÉLÉMENTS D'ALLIAGE ET D'HOMOGENÉISATION SUR LE
COMPORTEMENT À LA DÉFORMATION À CHAUD DES ALLIAGES
D'ALUMINIUM DE LA SÉRIE 1XXX**

FÉVRIER 2015

UNIVERSITY OF QUEBEC

**A DISSERTATION PRESENTED TO
THE UNIVERSITY OF QUEBEC AT CHICOUTIMI
IN PARTIAL FULFILLMENT OF THE REQUIREMENTS FOR THE
DOCTOR OF PHILOSOPHY IN ENGINEERING**

**BY
MOHAMMAD SHAKIBA**

**EFFECT OF HOMOGENIZATION AND ALLOYING ELEMENTS ON HOT
DEFORMATION BEHAVIOUR OF 1XXX SERIES ALUMINUM ALLOYS**

FEBRUARY 2015

Dedicated to my parents for their unconditional love and support

RÉSUMÉ

Les séries 1xxx des alliages d'aluminium sont largement utilisées pour des applications où une excellente aptitude au formage et de la conductivité thermique et électrique sont nécessaires, tels que les tubes d'échangeur de chaleur et les câbles coaxiaux de revêtement. La demande pour une productivité élevée pendant le traitement conduit à une augmentation de l'aptitude au formage à chaud pour fournir une contrainte d'écoulement faible avec les propriétés mécaniques finales souhaitées. Commercialement, les billettes coulées sont généralement homogénéisés avant l'extrusion ou le laminage à chaud, afin d'améliorer leur fluidité et leurs propriétés mécaniques. Cependant, les travaux de recherche antérieurs restent limités au sujet de l'efficacité du traitement d'homogénéisation dans la production des alliages 1xxx. De plus, aucune étude systématique de l'influence des différents éléments d'alliage (Fe, Si, Mn et Cu) sur le comportement de déformation à chaud des alliages dilués Al-Fe-Si est disponible dans la littérature.

Dans la présente étude, l'effet des différents éléments d'alliage ainsi que le traitement d'homogénéisation sur le formage à chaud et la microstructure des alliages dilués Al-Fe-Si ont été étudiés en utilisant des tests de compression à chaud, la microscopie optique, SEM, EBSD, TEM, ainsi que les mesures de conductivité électrique.

L'effet du traitement d'homogénéisation sur la microstructure et le formage à chaud de deux alliages dilués Al-Fe-Si a été étudiée. L'homogénéisation a favorisé la transformation

de phase à partir de la phase métastable AlmFe ou $\alpha\text{-AlFeSi}$ vers la phase d'équilibre Al_3Fe , et induit un changement significatif des concentrations de soluté dans la solution solide. L'homogénéisation à 550°C a significativement réduit les niveaux de solution solide en raison de l'élimination de la sursaturation en provenance du lingot coulé et a produit une contrainte d'écoulement plus basse sous toutes les conditions de déformation étudiées. Une augmentation de la température d'homogénéisation de 550 à 630°C augmente la contrainte d'écoulement de 10 à 23% et de 15 à 45% pour les alliages Al-0.3Fe-0.1Si et Al-0.3Fe-0.25Si , respectivement, dans la plage des conditions de déformation examinées.

Le comportement à la déformation à chaud des alliages diluées Al-Fe-Si contenant diverses quantités de Fe ($0,1$ à $0,7\%$ en poids) et Si ($0,1$ à $0,25\%$ en poids) a été étudié par des tests de compression uniaxiale réalisés à différentes températures ($350\text{-}550^\circ\text{C}$) et des vitesses de déformation (de $0,01$ à 10 s^{-1}). La contrainte d'écoulement des alliages $1xxx$ augmente avec l'augmentation de la teneur en Fe et Si . L'augmentation de la teneur en Fe de $0,1$ à $0,7\%$ a augmenté la contrainte d'écoulement de 11 à 32% dans les alliages Al-Fe-0.1Si , tandis que la contrainte d'écoulement a augmenté de 5 à 14% lorsque la teneur en Si est portée de $0,1$ à $0,25\%$ dans les alliages Al-0,1 Fe-Si . Les données de contrainte-déformation expérimentales ont été utilisées pour dériver les équations constitutives en corrélation entre la contrainte d'écoulement, la température de déformation et la vitesse de déformation, compte tenu de l'influence de la composition chimique. Les résultats de l'analyse de la microstructure a révélé que le recouvrement dynamique est le seul mécanisme de ramollissement lors de la déformation à chaud des alliages diluées Al-Fe-Si .

L'augmentation de la teneur en Fe et Si a retardé le recouvrement dynamique et a entraîné une diminution de la taille des sous-grains et de la désorientation des joints des grains.

En outre, le comportement en déformation à chaud des alliages dilués Al-Fe-Si contenant diverses teneurs en Mn (0,1 et 0,2% en poids) et en Cu (0,05, 0,18 et 0,31% en poids) a également été étudié. Il a été constaté que le manganèse et le cuivre en solution solide ont une influence significative sur le formage à chaud des alliages dilués Al-Fe-Si. Sur une base de pourcentage massique, le Mn présente un effet de renforcement plus fort par rapport au Cu. Les énergies d'activation pour la déformation ont été calculés à partir de données expérimentales pour tous les alliages étudiés. Avec l'ajout de 0,2% en pourcentage massique de Mn, l'énergie d'activation augmente de 161 et 176 kJ / mol, à faible Fe (0,1% en pourcentage massique) et de haut Fe (0,5% en pourcentage massique) Les alliages à base de 181 et 192 kJ / mol, respectivement. L'addition de Cu jusqu'à 0,31% en pourcentage massique n'a que légèrement augmenté l'énergie d'activation de faible alliage à base de Fe de 161 à 166 kJ / mol. La diffusion du soluté a agi en tant que mécanisme de contrôle des taux de déformation dans ces alliages dilués. Les alliages contenant du Mn ont une contrainte d'écoulement plus élevée et une énergie d'activation plus élevée en raison de la vitesse de diffusion considérablement plus faible dans l'aluminium de Mn par rapport aux alliages contenant du cuivre. Une addition de Mn et Cu a aussi retardé le recouvrement dynamique et a généré une diminution de la taille des sous-grains et une désorientation des joints de grains.

En outre, sur la base des données expérimentales des essais de compression à chaud, un modèle basé sur les réseaux de neurones artificiels a été développé pour prédire le comportement en écoulement à haute température de l'alliages Al-0.12Fe-0.1Si-Cu en

fonction de la composition chimique (avec différentes teneurs en Cu de 0.002-0.31 en pourcentage massique) et les paramètres de procédé. Un réseau de neurones de type back-propagation à trois couches avec 20 neurones dans la couche cachée a été établi dans cette étude pour prédire le comportement de l'écoulement de l'alliage Al-0.12Fe-0.1Si avec différents niveaux de Cu (0.002-0.31 en pourcentage massique) à différentes conditions de déformation. Les paramètres d'entrée étaient la teneur en Cu, la température, la vitesse de déformation et la contrainte, tandis que la contrainte d'écoulement constitue la sortie. La performance du modèle proposé a été évaluée à l'aide des différents paramètres statistiques classiques. Un excellent accord entre les résultats expérimentaux et prédits a été obtenu. L'analyse de sensibilité a indiqué que le taux de déformation est le paramètre le plus important, tandis que la teneur en Cu présentait une influence modeste mais significatif sur la contrainte d'écoulement. Le modèle ANN proposé dans cette étude peut prédire avec précision le comportement de déformation à chaud des alliages Al-0.12Fe-0.1Si.

ABSTRACT

The 1xxx series of aluminum alloys are widely used for applications in which excellent formability and thermal and electrical conductivity are required such as heat-exchanger tubing and coaxial cable sheathing. The demand for high productivity during processing leads to the requirement for an increase in hot workability to provide low flow stress with desirable final mechanical properties. Commercially, D.C cast billets are typically homogenized prior to extrusion or rolling to improve hot workability and mechanical properties. However, there is very limited prior work on the effectiveness of the homogenization treatment in 1xxx alloy production. Furthermore, no systematic investigation of the influence of different alloying elements (Fe, Si, Mn and Cu) on the hot deformation behavior of dilute Al-Fe-Si alloys is available in the literature.

In the present study, the effect of different alloying elements as well as the homogenization treatment on the hot workability and microstructure of dilute Al-Fe-Si alloys was investigated using hot compression tests, optical microscopy, SEM, electron EBSD, TEM, electrical conductivity measurements.

The effect of the homogenization treatment on the microstructure and hot workability of two dilute Al-Fe-Si alloys was first investigated. Homogenization promoted the phase transformation from the metastable Al_mFe or $\alpha-AlFeSi$ phase to the Al_3Fe equilibrium phase and induced a significant change in solute levels in the solid solution. Homogenization at 550°C significantly reduced the solid solution levels due to the

elimination of the supersaturation originating from the cast ingot and produced the lowest flow stress under all of the deformation conditions studied. An increase in the homogenization temperature from 550 to 630°C increased the flow stress by 10 to 23% and 15 to 45% for the Al-0.3Fe-0.1Si and Al-0.3Fe-0.25Si alloys, respectively, over the range of deformation conditions examined.

The hot deformation behavior of dilute Al-Fe-Si alloys containing different amounts of Fe (0.1 to 0.7 wt%) and Si (0.1 to 0.25 wt%) was studied by uniaxial compression tests conducted at various temperatures (350-550 °C) and strain rates (0.01-10 s⁻¹). The flow stress of the 1xxx alloys increased with increasing Fe and Si content. Increasing the Fe content from 0.1 to 0.7% raised the flow stress by 11-32% in Al-Fe-0.1Si alloys, whereas the flow stress increased 5-14% when the Si content increased from 0.1 to 0.25% in Al-0.1Fe-Si alloys. The experimental stress-strain data were employed to drive constitutive equations correlating flow stress, deformation temperature and strain rate considering the influence of the chemical composition. The microstructural analysis results revealed that dynamic recovery is the sole softening mechanism during hot deformation of dilute Al-Fe-Si alloys. Increasing the Fe and Si content retarded dynamic recovery and resulted in a decrease in the subgrain size and mean misorientation angle of the boundaries.

Furthermore, the hot deformation behavior of dilute Al-Fe-Si alloys containing various Mn (0.1 and 0.2 wt%) and Cu (0.05, 0.18 and 0.31 wt%) contents was also investigated. It was found that both manganese and copper in solid solution have a significant influence on the hot workability of dilute Al-Fe-Si alloys. On a wt% basis, Mn exhibits a stronger strengthening effect compared to Cu. The activation energies for deformation were calculated from experimental data for all the alloys investigated. With a

0.2 wt% Mn addition, the activation energy increased from 161 and 176 kJ/mol for low-Fe (0.1wt%) and high-Fe (0.5wt%) base alloys to 181 and 192 kJ/mol, respectively. The addition of Cu up to 0.31 wt% only slightly increased the activation energy of low-Fe base alloy from 161 to 166 kJ/mol. Solute diffusion acted as the deformation rate controlling mechanism in these dilute alloys. Mn containing alloys have higher flow stress and higher activation energy due to the considerably lower diffusion rate of Mn in aluminum compared to Cu containing alloys. An addition of Mn and Cu also retarded the dynamic recovery and resulted in a decrease in the subgrain size and mean misorientation angle of the grain boundaries.

In addition, based on hot compression tests, an artificial neural network model was developed to predict the high temperature flow behavior of Al-0.12Fe-0.1Si-Cu alloys as a function of chemical composition (with Cu contents of 0.002-0.31wt%) and process parameters. A three-layer feed-forward back-propagation artificial neural network with 20 neurons in a hidden layer was established in this study to predict the flow behavior of Al-0.12Fe-0.1Si alloy with various levels of Cu addition (0.002-0.31wt%) at different deformation conditions. The input parameters were Cu content, temperature, strain rate and strain, while the flow stress was the output. The performance of the proposed model was evaluated using various standard statistical parameters. An excellent agreement between experimental and predicted results was obtained. Sensitivity analysis indicated that the strain rate is the most important parameter, while the Cu content exhibited a modest but significant influence on the flow stress. The ANN model proposed in this study can accurately predict the hot deformation behavior of Al-0.12Fe-0.1Si alloys.

PATENTS AND PUBLICATIONS

US Patent:

1. M. Shakiba, N. Parson, X.-G.Chen, Homogenisation Practice to Provide Improved Extrudability for 1XXX Alloys, Submitted to US patent, 2014.

Journal articles:

1. M. Shakiba, N. Parson, X.-G. Chen, Effect of homogenization treatment and silicon content on the microstructure and hot workability of dilute Al-Fe-Si alloys, *Materials science and engineering A*, 619 (2014), pp. 180-189.

2. M. Shakiba, N. Parson, X.-G. Chen, Effect of iron and silicon content on the hot compressive deformation behavior of dilute Al-Fe-Si alloys, *Journal of Materials Engineering and Performance*, 2014, on-line published, DOI: 10.1007/s11665-014-1302-3.

3. M. Shakiba, N. Parson, X.-G. Chen, Effect of Mn and Cu additions on hot deformation behavior of dilute Al-Fe-Si alloys, under preparation, 2014.

4. M. Shakiba, N. Parson, X.-G. Chen, Modeling the influence of Cu content and deformation variables on the high temperature flow behavior of Al-Fe-Si alloys using an artificial neural network, ready to submit, 2014.

Scientific posters:

1. M. Shakiba, N. Parson and X.-G Chen, Effect of Mn and Cu additions on hot deformation behavior of dilute Al-Fe-Si alloys, the *Encyclopedia of Research on Aluminum in Quebec*, Les Presses de l'aluminum (PRAL), Sherbrooke, 2014.

2. M. Shakiba and X.-G Chen, Prediction of elevated temperature flow behaviour of 1xxx alloys with various iron and silicon levels, the *Encyclopedia of Research on Aluminum in Quebec*, Les Presses de l'aluminum (PRAL), Montreal, 2013.

3. M. Shakiba and X.-G Chen, Phase transformations of iron intermetallic compounds of Al-Fe-Si alloys, the *Encyclopedia of Research on Aluminum in Quebec*, Les Presses de l'aluminum (PRAL), Trois-Riviere, 2012.

ACKNOWLEDGEMENTS

The author would like to express his greatest appreciation to his director, **Prof. X.-Grant Chen** and co-director, **Prof. Nick Parson**, for their expertise guidance, encouragement, understanding and support through the duration of his PhD's study.

The author would also like to convey his gratitude to **Prof. Daniel Larouche** and **Prof. Dilip Kumar Sarkar** as the jury members for their inspirational advices.

The author wishes to acknowledge financial support from the **Natural Sciences and Engineering Research Council of Canada (NSERC)** and from **Rio Tinto Alcan** through the NSERC Industrial Research Chair in Metallurgy of Aluminum Transformation at the University of Québec at Chicoutimi.

The author is also grateful to the directors of graduate studies, **Prof. Mohand Ourouche**, for his valuable comments during his seminar evaluation. Also, the author wishes to thank Ms. **C. Dumas** and **H. Duchesne**, for her help with administrative tasks.

The author would like to extend his thanks to **Prof. Zhan Zhang** and **Prof. Agnes Marie Samuel** for their precious comments and guides during seminars I and II.

Grateful acknowledgment is also sent to **Mr. M. Bouchard** and **Ms. E. Brideau** at CURAL Laboratory for their technical support.

Finally, the author would like to convey his deepest gratitude to his beloved parents, sisters and his wife, **Azadeh**, for their immense supports and love without which this work would not have been possible.

TABLE OF CONTENTS

RÉSUMÉ	i
ABSTRACT	v
PATENTS AND PUBLICATIONS	viii
ACKNOWLEDGEMENTS	ix
TABLE OF CONTENTS	xi
LIST OF TABLES	xvi
LIST OF FIGURES	xvii
 CHAPTER 1	
INTRODUCTION	1
1.1 Background and problem definition.....	2
1.2 Objectives	6
References	7
 CHAPTER 2	
LITERATURE REVIEW	10
2.1 Hot working.....	11
2.1.1 Work Hardening	12
2.1.2 Solid solution hardening	12
2.1.3 Precipitation hardening	14
2.1.4 Softening Mechanisms.....	14

2.1.4.1 Dynamic Recovery	14
2.1.4.2 Dynamic Recrystallization	17
2.1.5 Dynamic recovery flow curves	21
2.1.6 Dynamic recrystallization flow curves	22
2.2 AA1xxx series aluminum alloys	23
2.2.1 Microstructure of AA1xxx series aluminum alloys.....	23
2.2.1.1 Binary Al-Fe phases	24
2.2.1.2 Ternary Al-Fe-Si phases	26
2.2.1.3 Transformation of metastable phases.....	28
2.2.2 Hot deformation behavior of AA1xxx aluminum alloys	30
2.2.2.1 Substructure evolution during hot deformation	33
2.2.2.2 Effect of homogenization.....	34
2.2.2.4 Effect of Mn	36
2.2.2.4 Effect of Cu	37
2.3 Modeling the high temperature flow behavior of metals and alloys	38
2.3.1 Phenomenological constitutive equations.....	39
2.3.2 Artificial neural network (ANN)	40
References	44
CHAPTER 3	
EFFECT OF HOMOGENIZATION TREATMENT AND SILICON CONTENT ON THE MICROSTRUCTURE AND HOT WORKABILITY OF DILUTE AL-FE-SI ALLOYS	
51	
Abstract.....	52

3.1 Introduction	53
3.2 Experimental Procedure	55
3.3 Results and Discussion	58
3.3.1 As-cast and homogenized microstructures	58
3.3.2. Evolution of iron-rich intermetallic phases during homogenization	59
3.3.2.1. Solid-state transformation from Al_mFe to Al_3Fe	63
3.3.2.2. Solid-state transformation from $\alpha-AlFeSi$ to Al_3Fe	65
3.3.3. Solid solution levels.....	66
3.3.4. Flow stress behavior during hot deformation	69
3.3.5. Discussion.....	72
3.3.5.1. Effect of constituent particles.....	73
3.3.5.2 Impact of solute elements.....	74
3.3.5.3 Industrial aspect	76
3.4 Conclusions	78
References	79
 CHAPTER 4	
EFFECT OF IRON AND SILICON CONTENT ON THE HOT COMPRESSIVE DEFORMATION BEHAVIOR OF DILUTE AL-FE-SI ALLOYS.....	
Abstract.....	83
4.1 Introduction	84
4.2 Experimental.....	86
4.3 Result and discussion	88
4.3.1 Flow stress behavior	88

4.3.2 Constitutive analysis	93
4.3.3 Effect of chemical composition	98
4.3.4 Microstructural evolution during hot deformation	102
4.4. Conclusions	111
References	113
CHAPTER 5	
HOT DEFORMATION BEHAVIOR AND RATE CONTROLLING MECHANISM IN DILUTE AL-FE-SI ALLOYS WITH MINOR ADDITIONS OF MN AND CU.....116	
Abstract.....	117
5.1 Introduction	118
5.2 Experimental procedure.....	120
5.3 Results and discussion.....	122
5.3.1 Flow stress behavior	122
5.3.2 Constitutive analyses	128
5.3.3 Microstructural evolution during hot deformation	133
5.3.4 Discussion.....	138
5.4 Conclusions	144
References	144
CHAPTER 6	
MODELING THE EFFECTS OF CU CONTENT AND DEFORMATION VARIABLES ON THE HIGH-TEMPERATURE FLOW BEHAVIOR OF AL-FE-SI ALLOYS USING AN ARTIFICIAL NEURAL NETWORK.....148	
Abstract.....	149

6.1 Introduction	150
6.2 Experimental procedures	152
6.3 Results and discussion	153
6.3.1 Effect of Cu content on flow stress behavior.....	153
6.3.2 Development of artificial neural network model.....	157
6.3.2.1 Effect of Cu addition.....	160
6.3.2.2 Effect of temperature.....	161
6.3.2.3 Effect of strain rate.....	161
6.3.2.4 Assessment of the proposed model	163
6.3.2.5 Sensitivity analysis.....	166
6.4 Conclusions	167
Appendix 6.A: Example illustrating Garson’s algorithm.....	168
References	170
CHAPTER 7	
CONCLUSIONS & RECOMMENDATIONS	173
7.1 Conclusions	174
7.2 Recommendations	179

LIST OF TABLES

Table 3.1	Chemical compositions of two Al-Fe-Si alloys studied (wt%)	56
Table 4.1	Chemical compositions of the experimental alloys (wt%)	87
Table 4.2	Values of material constants and activation energies of all experimental alloys	98
Table 4.3	Coefficients of the polynomial fit of α , Q, n and lnA for the Al-Fe-0.1Si alloy	100
Table 4.4	Coefficients of the polynomial fit of α , Q, n and lnA for the Al-Fe-0.25Si alloy	100
Table 4.5	Evolution of the mean misorientation angle and the subgrain size under various deformation conditions in the Al-0.1Fe-0.1Si alloy	106
Table 5.1	Chemical compositions of experimental alloys (wt%)	122
Table 5.2	Values of material constants and activation energies of all the experimental alloys at strain 0.8	132
Table 5.3	Subgrain size and mean misorientation angle of deformed samples at T = 500°C and $\dot{\epsilon} = 0.01 \text{ s}^{-1}$ to strain of 0.8	138
Table 5.4	Atomic radius and shear modulus of alloying elements of aluminum [12]	140
Table 6.1	Chemical compositions of alloys (wt%)	153
Table 6.2	The values of R, AARE and RMSE for the proposed ANN model	165

LIST OF FIGURES

Fig. 2.1	Various stages in the recovery of plastically deformed material [2].....	16
Fig. 2.2	Microstructure in ND-RD plane of Al-0.1%Mg deformed in plane strain compression at $T = 350^{\circ}\text{C}$, $\dot{\epsilon} = 0.25 \text{ s}^{-1}$ and $\epsilon = 1$. (a) EBSD map showing LAGBs (white) and serrated HAGBs (black), (b) SEM channelling contrast image showing the subgrain structure [2]	17
Fig. 2.3	Mechanism of DRX by progressive lattice rotation in Al-Mg alloys; (a) HAGB serrations form, (b) Grain boundary sliding occurs on horizontal boundaries, but slip occurs on bulged sections, leading to local lattice rotations associated with the bulges, (c) [2].....	20
Fig. 2.4	When the grains are extremely thinned, they pinch off or perforate where opposite serration come into contact [3]	20
Fig. 2.5	Typical DRV stress-strain curves [22]	21
Fig. 2.6	Typical DRX stress-strain curves [2]	22
Fig. 2.7	Al rich corner of the equilibrium Al-Fe binary phase diagram [27]	24
Fig. 2.8	(a) Al_3Fe at grain boundaries in cast ingot under TEM and (b) typical [110] diffraction pattern of a faulted Al_3Fe crystal [27]	25
Fig. 2.9	Fe intermetallic phases morphology (deep-etching) under SEM (a) Curved plates like Al_6Fe phase and (b) fine feathery like Al_mFe phase [39]	26
Fig. 2.10	Liquidus projection in the Al corner of the ternary Al-Fe-Si phase diagram [27]	27

Fig. 2.11	Compositions of the common binary and ternary compounds found in Al-Fe-Si alloys [41]	28
Fig.2.12	Variation of normalized X-Ray intensity of Al_mFe , Al_6Fe and Al_3Fe with homogenization temperature in (a) Al-0.8Fe and (b) Al-0.6Fe alloys [42] ..	30
Fig. 2.13	TEM micrographs of subgrains structures in Al-0.65Fe alloy deformed at (a) $300^\circ C / 0.1 s^{-1}$ and (b) $500^\circ C / 0.1 s^{-1}$ [3].....	34
Fig.2.14	Schematic structure of an artificial neutral network [85].....	42
Fig.2.15	Shape of sigmoid function [85]	43
Fig. 3.1	As-cast microstructures: (a) low Si alloy (Al-0.3Fe-0.1Si) and (b) high Si alloy (Al-0.3Fe-0.25Si)	59
Fig. 3.2	Microstructures after homogenization at $630^\circ C$ for 12 h: (a) low Si alloy (Al-0.3Fe-0.1Si) and (b) high Si alloy (Al-0.3Fe-0.25Si)	59
Fig. 3.3	Backscattered electron images and corresponding EBSD solutions for different type of Fe-rich particles: (a) Al_mFe (as-cast Al-0.3Fe-0.1Si), (b) Al_6Fe (as-cast Al-0.3Fe-0.1Si), (c) Al_3Fe (Al-0.3Fe-0.25Si homogenized at $630^\circ C$ for 12 h) and (d) $\alpha-AlFeSi$ (as-cast Al-0.3Fe-0.25Si)	62
Fig. 3.4	Evolution of the phase volume fractions of Fe-rich intermetallics for the as-cast and homogenized conditions: (a) low Si alloy and (b) high Si alloy	63
Fig. 3.5	Transformation from Al_mFe to Al_3Fe in the low Si alloy: (a) As-cast, (b) $550^\circ C$ for 2 h, (c) $550^\circ C$ for 2 h at high magnification and (d) $550^\circ C$ for 6 h ..	64
Fig. 3.6	Transformation from $\alpha-AlFeSi$ to Al_3Fe in the high Si alloy: (a) As-cast, (b) and (c) $630^\circ C$ for 2 h and (d) $630^\circ C$ for 12 h	66
Fig. 3.7	Effect of homogenization practice on the electrical conductivity: (a) low Si alloy and (b) high Si alloy	68

Fig. 3.8	True stress-true strain curves for different initial states of the low Si alloy under different deformation conditions: (a) $\dot{\epsilon}=0.01 \text{ s}^{-1}$, $T=400 \text{ }^{\circ}\text{C}$, (b) $\dot{\epsilon}=0.01 \text{ s}^{-1}$, $T=500 \text{ }^{\circ}\text{C}$ (c) $\dot{\epsilon}=1 \text{ s}^{-1}$, $T=400 \text{ }^{\circ}\text{C}$ and (d) $\dot{\epsilon}=1 \text{ s}^{-1}$, $T=500 \text{ }^{\circ}\text{C}$ 70
Fig. 3.9	True stress-true strain curves for different initial states of the high Si alloy under different deformation conditions: (a) $\dot{\epsilon}=0.01 \text{ s}^{-1}$, $T=400 \text{ }^{\circ}\text{C}$, (b) $\dot{\epsilon}=0.01 \text{ s}^{-1}$, $T=500 \text{ }^{\circ}\text{C}$ (c) $\dot{\epsilon}=1 \text{ s}^{-1}$, $T=400 \text{ }^{\circ}\text{C}$ and (d) $\dot{\epsilon}=1 \text{ s}^{-1}$, $T=500 \text{ }^{\circ}\text{C}$ 71
Fig. 3.10	Effect of homogenization treatment on the flow stress (a) $\dot{\epsilon}: 1 \text{ s}^{-1}$, $T: 400^{\circ}\text{C}$ and (b) $\dot{\epsilon}: 1 \text{ s}^{-1}$, $T: 500^{\circ}\text{C}$ at a strain of 0.8..... 72
Fig. 3.11	Phase diagram of the binary Al-Fe system showing the solid solubility of iron in aluminum as a function of temperature [27]..... 75
Fig.4.1	True stress-true strain curves of Al-0.1Fe-0.1Si alloy at various strain rates (a) $\dot{\epsilon} = 0.01 \text{ s}^{-1}$, (b) $\dot{\epsilon} = 0.1 \text{ s}^{-1}$, (c) $\dot{\epsilon} = 1 \text{ s}^{-1}$ and (d) $\dot{\epsilon} = 10 \text{ s}^{-1}$ 90
Fig.4.2	True stress-true strain curves of Al-0.5Fe-0.1Si alloy at various strain rates (a) $\dot{\epsilon} = 0.01 \text{ s}^{-1}$, (b) $\dot{\epsilon} = 0.1 \text{ s}^{-1}$, (c) $\dot{\epsilon} = 1 \text{ s}^{-1}$ and (d) $\dot{\epsilon} = 10 \text{ s}^{-1}$ 91
Fig.4.3	Effect of iron on flow stress at strain of 0.8, (a) Al-Fe-0.1Si $\dot{\epsilon} = 0.01 \text{ s}^{-1}$, (b) Al-Fe-0.1Si $\dot{\epsilon} = 10 \text{ s}^{-1}$, (c) Al-Fe-0.25Si $\dot{\epsilon} = 0.01 \text{ s}^{-1}$ and (d) Al-Fe-0.25Si $\dot{\epsilon} = 10 \text{ s}^{-1}$ 92
Fig.4.4	Effect of silicon on flow stress at strain of 0.8, (a) Al-0.1Fe-Si $\dot{\epsilon} = 0.01 \text{ s}^{-1}$, (b) Al-0.1Fe-Si $\dot{\epsilon} = 10 \text{ s}^{-1}$, (c) Al-0.5Fe-Si $\dot{\epsilon} = 0.01 \text{ s}^{-1}$ and (d) Al-0.5Fe-Si $\dot{\epsilon} = 10 \text{ s}^{-1}$ 93
Fig.4.5	Plots of (a) $\ln\dot{\epsilon} - \sigma$ and (b) $\ln\dot{\epsilon} - \ln\sigma$ for Al-0.1Fe-0.1Si alloy..... 95
Fig.4.6	Plots of (a) $\ln\dot{\epsilon}$ vs. $\ln[\sinh(\alpha\sigma)]$ and (b) $\ln[\sinh(\alpha\sigma)]$ vs. $(1000/T)$ for Al-0.1Fe-0.1Si alloy 97
Fig.4.7	Plot of $\ln Z$ vs. $\ln[\sinh(\alpha\sigma)]$ for Al-0.1Fe-0.1Si alloy 97

Fig.4.8	Relationship between (a) α (b) Q , (c) n and (d) $\ln A$ and Fe level by polynomial fit for both Al-Fe-0.1Si or Al-Fe-0.25Si alloys	99
Fig.4.9	Correlation between the experimental and predicted flow stress of 1xxx alloys	102
Fig. 4.10	As-homogenized microstructures of (a) Al-0.1Fe-0.1Si and (b) Al-0.5Fe-0.1Si	103
Fig.4.11	Orientation imaging maps of Al-0.1Fe-0.1Si alloy under various deformation conditions: (a) 10 s^{-1} , $400 \text{ }^\circ\text{C}$, (b) 0.01 s^{-1} , $400 \text{ }^\circ\text{C}$ and (c) 0.01 s^{-1} , $500 \text{ }^\circ\text{C}$. White lines $1\text{-}5^\circ$, blue lines $5\text{-}15^\circ$ and black lines $> 15^\circ$	105
Fig.4.12	Orientation imaging maps of (a) Al-0.3Fe-0.1Si (b) Al-0.5Fe-0.1Si, (c) Al-0.1Fe-0.25Si and (d) Al-0.5Fe-0.25Si alloy deformed at $500 \text{ }^\circ\text{C}$ and 0.01 s^{-1}	108
Fig.4.13	Effect of Fe and Si contents on (a) Mean misorientation angle, (b) subgrain size of 1xxx alloys deformed at $500 \text{ }^\circ\text{C}$ and 0.01 s^{-1}	108
Fig. 4.14	Relationship between (a) the reciprocal subgrain diameter (d^{-1}) and logarithm of the Zener-Hollomon parameter (Z), (b) the steady-state flow stress (σ) and reciprocal subgrain diameter (d^{-1})	109
Fig.5.1	Typical true stress-true strain curves of: (a) Al-0.1Fe-0.1Si, (b) Al-0.5Fe-0.1Si, (c) Al-0.1Fe-0.1Si-0.1Mn, and (d) Al-0.5Fe-0.1Si-0.1Mn, (e) Al-0.1Fe-0.1Si-0.2Mn and (f) Al-0.5Fe-0.1Si-0.2Mn alloys	125
Fig.5.2	Typical true stress-true strain curves of: (a) Al-0.1Fe-0.1Si, (b) Al-0.1Fe-0.1Si-0.05Cu, (c) Al-0.1Fe-0.1Si-0.18Cu and (d) Al-0.1Fe-0.1Si-0.31Cu alloys.....	126
Fig.5.3	Effect of Mn and Cu on the flow stress at a strain of 0.8: (a) Al-0.1Fe-0.1Si-Mn, $\dot{\epsilon} = 0.01 \text{ s}^{-1}$, (b) Al-0.1Fe-0.1Si-Mn, $\dot{\epsilon} = 10 \text{ s}^{-1}$, (c) Al-0.5Fe-0.1Si-Mn, $\dot{\epsilon} = 0.01 \text{ s}^{-1}$, (d) Al-0.5Fe-0.1Si-Mn, $\dot{\epsilon} = 10 \text{ s}^{-1}$, (e) Al-0.1Fe-0.1Si-Cu, $\dot{\epsilon} = 0.01 \text{ s}^{-1}$ and (f) Al-0.1Fe-0.1Si-Cu, $\dot{\epsilon} = 10 \text{ s}^{-1}$	127

Fig.5.4	Effect of Mn and Cu contents on the flow stress at a strain of 0.8, temperature of 400 °C, and two extremes of strain rate: (a) $\dot{\epsilon} = 0.01 \text{ s}^{-1}$ and (b) $\dot{\epsilon} = 10 \text{ s}^{-1}$	128
Fig.5.5	Plots of (a) $\ln \dot{\epsilon} - \sigma$ and (b) $\ln \dot{\epsilon} - \ln \sigma$	130
Fig.5.6	Plots of (a) $\ln \dot{\epsilon}$ vs. $\ln[\sinh(\alpha\sigma)]$ and (b) $\ln[\sinh(\alpha\sigma)]$ vs. $(1000/T)$	130
Fig.5.7	Plot of $\ln Z$ vs. $\ln[\sinh(\alpha\sigma)]$	131
Fig.5.8	Activation energy of dilute Al-Fe-Si alloys as a function of alloying addition.....	132
Fig.5.9	TEM microimages of the deformed samples at T= 400 °C and $\dot{\epsilon} = 1 \text{ s}^{-1}$ (a) Al-0.1Fe-0.1Si-0.2Mn (b) Al-0.5Fe-0.1Si-0.2Mn.....	135
Fig.5.10	Orientation imaging maps of (a) Al-0.1Fe-0.1Si, (b) Al-0.1Fe-0.1Si-0.31Cu, (c) Al-0.1Fe-0.1Si-0.2Mn, (d) Al-0.5Fe-0.1Si and (e) Al-0.5Fe-0.1Si-0.2Mn samples deformed at 500°C and $\dot{\epsilon} = 0.01 \text{ s}^{-1}$. White lines 1-5°, blue lines 5-15° and black lines > 15°	137
Fig.5.11	The diffusion rate of various solutes in aluminum as a function of reciprocal temperature [31]	141
Fig. 6.1	Typical true stress-true strain curves of: (a) Base alloy, (b) 0.05% Cu, (c) 0.18% Cu and (d) 0.31% Cu	155
Fig. 6.2	Effect of Cu content on flow stress of Al-0.12Fe-0.1Si alloy at strain of 0.4; (a) $\dot{\epsilon} = 0.01 \text{ s}^{-1}$, (b) $\dot{\epsilon} = 0.1 \text{ s}^{-1}$, (c) $\dot{\epsilon} = 1 \text{ s}^{-1}$ and (d) $\dot{\epsilon} = 10 \text{ s}^{-1}$	156
Fig. 6.3	The architecture of the ANN model	157
Fig. 6.4	Performance of the network with different levels of hidden neurons	159
Fig. 6.5	Effect of Cu content on the flow stress at a strain of 0.4 (a) for 400 °C/10 s^{-1} and 450 °C/1 s^{-1} and (b) for 500 °C/0.1 s^{-1} and 550 °C/0.01 s^{-1}	160
Fig. 6.6	Effect of deformation temperature on the flow stress of experimental alloys at a strain of 0.4; (a) base alloy and (b) 0.31% Cu.....	162

Fig. 6.7	Effect of deformation strain rate on the flow stress of experimental alloys at a strain of 0.4; (a) base alloy and (b) 0.31% Cu1.....	162
Fig. 6.8	Comparison between predicted ANN model and measured flow stress curves of (a) base alloy at $\dot{\epsilon}= 0.01 \text{ s}^{-1}$, (b) 0.05% Cu alloy at $\dot{\epsilon}= 0.1 \text{ s}^{-1}$, (c) 0.18% Cu alloy at $\dot{\epsilon}= 1 \text{ s}^{-1}$, and (d) 0.31% Cu alloy at $\dot{\epsilon}= 10 \text{ s}^{-1}$	165
Fig. 6.9	Relative importance of individual input parameters	166
Fig.6.A.1	The structure of a 4-2-1 artificial neural network.....	168

CHAPTER 1

INTRODUCTION

CHAPTER 1

INTRODUCTION

1.1 Background and problem definition

Wrought 1xxx series aluminum alloys are used in a wide range of applications and product forms where excellent formability, corrosion resistance and electrical and thermal conductivity are desirable such as foil and strip for packaging and heat-exchanger tubing, cable sheathing and fin stock [1, 2]. In general, these products are hot deformed by extrusion or rolling from direct chill (DC) cast billets or ingots. To reduce production cost, high processing rates, which are controlled primarily by the flow stress, are desirable. The hot working characteristics of the cast billet or ingot have a significant influence on the hot forming process, which in turn are determined by the billet or ingot's microstructure and hot deformation regimes [3, 4].

Commercially, DC cast billets or ingots are typically homogenized prior to extrusion or rolling to improve hot workability and mechanical properties [5, 6]. In many cases, the hot workability can be optimized by proper selection of the homogenization method applied to the cast materials [7]. However, there is very limited information in the literature on the effectiveness of the homogenization treatment in 1xxx alloy production.

Commercial 1xxx aluminum alloys exhibit higher strength and work hardening than high purity aluminum. The main alloying additions, or controlled impurities, in these alloys are Fe and Si. Typically, the levels of iron and silicon in a specific alloy are controlled to give the required performance such as strength, formability or corrosion resistance. This can result in many commercial variants existing within a given AA specification. Many believe that the metallurgical performance of 1xxx alloys is determined by the solid solution levels of Fe and Si and the second phase particles type, morphology and distribution [5]. Zhao et al. [8] reported that Fe and Si play a major role in the strength and work hardening of commercial 1xxx alloys and that the contribution from the other impurities is negligible. McQueen et al. [9-11] concluded that dynamic recrystallization (DRX) could not occur in commercially pure aluminum (1xxx alloys) and that dynamic recovery (DRV) was the sole restoration mechanism during hot deformation. Although a few researchers [9, 11, 12] have studied the hot deformation behavior of commercially pure aluminum, no systematic investigation of the influence of different Fe and Si contents on the hot deformation behavior of dilute Al-Fe-Si alloys is available in the literature.

An alternate approach to gain strength in a specific alloy is to add other alloying elements such as manganese and copper for solution strengthening. Mn is normally added to aluminum in order to control dynamic softening processes. Generally, Mn in the presence of other elements of low solubility such as iron and silicon, forms coarse constituent particles and fine dispersoids that serve as obstacles against grain boundary migration and dislocation movement [13, 14]. But Mn also has a significant influence on the strength of aluminum alloys when presents in solid solution [13]. Copper as alloying

element is often added to improve the aluminum strength [1, 15]. However, additions of Cu more than 1.1% result in formation of coarse intermetallics during casting which can establish initiation site for corrosion. Considering the role of the large copper containing intermetallics in corrosion, the most recent work shows rather an improved corrosion resistance, when the copper remains in solid solution [16].

A number of studies have been performed on the solid solution strengthening of materials [5, 13, 17, 18]. Solute addition results in retardation of dislocation movement, enhancing the rate of dislocation multiplication and restriction of dynamic softening processes [5, 19]. The size and shear modulus differences between solute atoms and solvent matrix both have significant impact on the strengthening effect of solute elements [17, 20, 21]. Normally, the size effect is strong, which produces an attractive force between the solute atoms and the dislocation cores [21]. The shear modulus difference becomes significant when the solvent and solute atoms show similar sizes [21]. Spittel et al. [20] showed that 1% Mg with higher atomic radius difference, increases the flow stress of aluminum more significantly than 1% Cu with a smaller atomic radius difference. Ryen et al. [13] revealed that both Mg and Mn in solid solution give a nearly linear concentration dependence of strength for commercially pure aluminum alloys. Although, due to the clustering effect between Mn and trace elements in solid solution, Mn gave a considerably higher hardening effect per atom compare to Mg. Sherby et al. [22] studied the effect of trace amounts of iron addition on the creep behavior of the pure aluminum and found that the creep rate is controlled by the rate of solute atom diffusion in the subgrain boundary

region. However, a systematic investigation on the effect of different Mn and Cu contents on the hot deformation behavior of 1xxx aluminum alloys cannot be found in the literature.

In the first two parts of present study, systematic research work was carried out to clarify the effects of homogenization treatment as well as Fe and Si content on the hot deformation behavior of dilute Al-Fe-Si alloys. Then, the impact of Mn and Cu elements on the hot workability of these alloys was investigated with the long term view of optimizing 1xxx alloy design for strength and hot processability.

Finally, the capability of the artificial neural network (ANN) approach to predict the high temperature flow behavior of Al-0.12Fe-0.1Si-Cu alloys was examined as a function of chemical composition and process parameters. The flow behavior of materials is very important for the design of hot-forming processes due to its substantial impact on the required deformation load as well as the kinetics of metallurgical transformations. Traditionally, the trial and error method has been employed to optimize the thermomechanical processes. To overcome the huge number of tests required to achieve a reliable conclusion in the trial and error practice, ANN provides an efficient modeling approach that permits a significant reduction in the production cost. Recently the ANN has been successfully applied to model the high temperature flow behavior of stainless steels [23], aluminum alloys [24, 25], magnesium alloys [26], titanium alloys [27, 28] and Al-base metal matrix composites [29]. To date, no ANN model has been found to include the effect of both chemical composition and deformation variables simultaneously in aluminum alloys. In the present study, an ANN model has been proposed to predict the flow behavior of the Al-0.12Fe-0.1Si alloy with various levels of Cu addition (0.002-0.31wt.%) at

different deformation conditions. Sensitivity analysis was carried out in order to quantify the relative importance of the Cu content and individual deformation variables on the high temperature flow stress.

1.2 Objectives

This research project is divided in four parts. The objectives of each part are detailed as follows:

1) Effect of homogenization treatment;

- a) Investigating the effect of the homogenization parameters on the intermetallic phase transformation and solid solution levels of Al-Fe-Si alloys.
- b) Improving the hot workability of 1xxx alloys through adjusting the optimum homogenization conditions.

2) Influence of iron and silicon contents;

- a) Systematically studying the effect of iron and silicon contents and deformation variables on the hot workability of dilute Al-Fe-Si alloys.
- b) Developing proper constitutive equations to correlate flow stress, deformation temperature and strain rate considering the influence of the chemical composition.
- c) Investigating the effects of the deformation conditions and the chemical composition on the microstructural evolution during hot deformation of dilute Al-Fe-Si alloys.

3) Effect of minor additions of Mn and Cu;

- a) Assessing the impact of Mn and Cu minor additions on the flow stress and activation energy of 1xxx alloys.
- b) Studying the effect of Mn and Cu additions on the substructures of dilute Al-Fe-Si alloys.
- c) Investigating the strengthening mechanism of Mn and Cu minor additions in 1xxx alloys.

4) Modelling the effect of thermomechanical parameters and chemical composition on the hot deformation behavior of Al-0.1Fe-0.1Si-Cu alloys using ANN

- a) Evaluating the capability of the ANN approach to predict the high-temperature flow behavior of Al-0.1Fe-0.1Si-Cu alloys as a function of chemical composition and process parameters.
- b) Quantifying the relative importance of Cu addition and individual deformation variables on the flow stress of Al-0.1Fe-0.1Si-Cu alloys.

References

- [1] J.R. Davis, Aluminum and aluminum alloys. Materials Park, OH, ASM International, 1993 pp. 59-87.
- [2] J.G. Kaufman, Introduction to aluminum alloys and tempers. Materials Park, OH, ASM International, 2000, pp. 87-118.
- [3] J. Zhang, B. Chen, Z. Baoxiang, Effect of initial microstructure on the hot compression deformation behavior of a 2219 aluminum alloy, Mater. Des., 2012, 34, pp.15-21.

- [4] H. Li, Z. Li, M. Song, X. Liang, F. Guo, Hot deformation behavior and microstructural evolution of Ag-containing 2519 aluminum alloy, *Mater. Des.*, 2010, 31, pp.2171-6.
- [5] H.J. McQueen, S. Spigarelli, M.E. Kassner, E. Evangelista, Hot deformation and processing of aluminum alloys. Florida, CRC Press, 2011.
- [6] Y.V.R.K. Prasad, K.P. Rao, Effect of homogenization on the hot deformation behavior of cast AZ31 magnesium alloy, *Mater. Des.*, 2009, 30, pp.3723-30.
- [7] Y. Totik, M. Gavkali, The effect of homogenization treatment on the hot workability between the surface and the center of AA 2014 ingots, *Mater. Charact.*, 2002, 49, pp.261-8.
- [8] Q. Zhao, M. Slagvold, B. Holmedal, Comparison of the influence of Si and Fe in 99.999% purity aluminum and in commercial-purity aluminum, *Scripta Mater.*, 2012, 67, pp.217-20.
- [9] H.J. McQueen, E. Evangelista, N. Jin, M.E. Kassner, Energy dissipation efficiency in aluminum dependent on monotonic flow curves and dynamic recovery, *Metall. Mater. Trans. A*, 1995, 26, pp.1757-66.
- [10] H.J. McQueen, W. Blum, Dynamic recovery: sufficient mechanism in the hot deformation of Al, *Mater. Sci. Eng. A*, 2000, 290, pp.95-107.
- [11] H. McQueen, J. Hockett, Microstructures of aluminum compressed at various rates and temperatures, *Metall. Trans.*, 1970, 1, pp.2997-3004.
- [12] H.R. Rezaei Ashtiani, M.H. Parsa, H. Bisadi, Constitutive equations for elevated temperature flow behavior of commercial purity aluminum, *Mater. Sci. Eng. A*, 2012, 545, pp.61-7.
- [13] Ø. Ryen, B. Holmedal, O. Nijs, E. Nes, E. Sjölander, H.-E. Ekström, Strengthening mechanisms in solid solution aluminum alloys, *MMTA*, 2006, 37, pp.1999-2006.
- [14] T. Furu, R. Rysund, E. Nes, Substructure evolution during different hot deformation processes of commercial non-heat treatable aluminium alloys, *Mater. Sci. Eng. A*, 1996, 214, pp.122-32.
- [15] M.M.R. Jaradeh, T. Carlberg, Solidification Studies of 3003 Aluminium Alloys with Cu and Zr Additions, *J. Mater. Sci. Technol.*, 2011, 27, pp.615-27.
- [16] R. Benedictus, S.D. Meijers, A.J.W. And, J.H.W.D. Wit, Influence of alloying additions on corrosion behavior of aluminum brazing sheet, In: T. Sato, editor. 6th International Conference on Aluminum Alloys, ICAA-6. Japan, The Japan Institute of Light Metals; 1998, pp. 1577-82.
- [17] P. Haasen, Physical metallurgy. In: R.W. Chan, Haasen P, editors., 4th ed., Elsevier ltd., 1996, pp. 2009-68.
- [18] R.L. Fleischer, W.R. Hibbard, The relation between the structure and mechanical properties of metals, London: H.M. Stationery Off., 1963, pp. 262-94.

- [19] C.O. Schmidt, Modelling the solute strengthening-deformation strengthening interaction, *Inter. J. Eng. Sci.*, 1984, 22, pp.1055-63.
- [20] M. Spittel, T. Spittel. Flow stress of light metal alloys. In: Warlimont H, editor. Part 2: Non-ferrous Alloys - Light Metals: Springer Berlin Heidelberg, 2011, pp. 19-53.
- [21] B. Verlinden, J. Driver, I. Samajdar, R.D. Doherty, Thermo-Mechanical processing of metallic materials. Oxford, UK, Elsevier, 2007.
- [22] O.D. Sherby, A. Goldberg, O.A. Ruano, Solute-diffusion-controlled dislocation creep in pure aluminium containing 0.026 at.% Fe, *Philos. Mag.*, 2004, 84, pp.2417-34.
- [23] S. Mandal, P.V. Sivaprasad, S. Venugopal, K.P.N. Murthy, Artificial neural network modeling to evaluate and predict the deformation behavior of stainless steel type AISI 304L during hot torsion, *Appl. Soft Comput.*, 2009, 9, pp.237-44.
- [24] N. Haghdadi, A. Zarei-Hanzaki, A.R. Khalesian, H.R. Abedi, Artificial neural network modeling to predict the hot deformation behavior of an A356 aluminum alloy, *Mater. Des.*, 2013, 49, pp.386-91.
- [25] S. Toros, F. Ozturk, Flow curve prediction of Al-Mg alloys under warm forming conditions at various strain rates by ANN, *Appl. Soft Comput.*, 2011, 11, pp.1891-8.
- [26] Y.J. Qin, Q.L. Pan, Y.B. He, W.B. Li, X.Y. Liu, X. Fan, Artificial neural network modeling to evaluate and predict the deformation behavior of zk60 magnesium alloy during hot compression, *Mater. Manuf. Process.*, 2010, 25, pp.539-45.
- [27] Y. Sun, W. Zeng, X. Ma, B. Xu, X. Liang, J. Zhang, A hybrid approach for processing parameters optimization of Ti-22Al-25Nb alloy during hot deformation using artificial neural network and genetic algorithm, *Intermetallics*, 2011, 19, pp.1014-9.
- [28] Y. Sun, W.D. Zeng, Y.Q. Zhao, Y.L. Qi, X. Ma, Y.F. Han, Development of constitutive relationship model of Ti600 alloy using artificial neural network, *Comput. Mater. Sci.*, 2010, 48, pp.686-91.
- [29] I.S. Jalham, Modeling capability of the artificial neural network (ANN) to predict the effect of the hot deformation parameters on the strength of Al-base metal matrix composites, *Compos. Sci. Technol.*, 2003, 63, pp.63-7.

CHAPTER 2

LITERATURE REVIEW

CHAPTER 2

LITERATURE REVIEW

2.1 Hot working

Hot working usually refers to the processes where metals are plastically deformed at an elevated temperature $T_M > 0.5$ (T_M melting point) and high strain rate ($\dot{\epsilon}$) (0.01 -100 S^{-1}) [1]. Hot working processes are of great industrial interest because most metals show low flow stress and high ductility at high temperatures. Today more than 80% of all metals products are manufactured by the various hot working processes such as rolling and extrusion. Generally, the plastic deformation is the result of dislocation glide, which leads to considerable strain hardening. In hot working, the strain hardening is simultaneously alleviated by dynamic softening processes. The typical dynamic softening processes are dynamic recovery in high stacking-fault energy (SFE) materials and dynamic recrystallization in low SFE materials [2]. General understanding of the strain hardening and various restoration mechanisms in hot working is useful to maximize productivity and minimize product defects. Furthermore, constitutive equations relating σ to ϵ , $\dot{\epsilon}$ and T could be used to describe flow behavior of a metallic system [3, 4].

2.1.1 Work Hardening

Work hardening is one of the most important characteristic properties of metallic alloys. The maximum amount of uniform plastic deformation that a metal can undergo is defined as the work hardening coefficient [5]. Therefore, metals with a higher work hardening coefficient can undergo more complex-forming operations without failure. Plastic deformation of crystalline materials occurs by the movement of dislocations along crystal planes due to the applied stress. Work hardening or strain hardening is a result of the fact that the stress needed for dislocation movement usually rises during plastic deformation as the dislocation motion becomes increasingly impeded by microstructural obstacles. Solute atoms, other dislocations, second phase particles and grain boundaries are the most common obstacles to dislocation movement [2, 5, 6].

Generally, dislocations contribute most to the variation in obstacle density. The dislocation density gradually rises as deformation proceeds because some fraction of the mobile dislocations that produce the strain do not exit through the surface, are not absorbed in grain boundaries, and do not annihilate each other, but are stored in the crystals. Therefore, the stress required for plastic flow increases due to the multiplication of the dislocations and the dislocations interactions [7].

2.1.2 Solid solution hardening

Solute atoms have a significant influence on the work hardening behavior of most metals and alloys. A high solute content can decrease the stacking-fault energy, resulting in more difficulty in cross slip. However this solute effect on stacking-fault energy can be

neglected in dilute alloys. The dislocation-solute interactions have a significant effect on work hardening. In solid solution, the interaction between solute elements and the dislocation significantly reduces their mobility thereby increasing the stress required for plastic flow. The size and shear modulus differences between solute atoms and the solvent matrix both have significant impact on the interaction energy [8]. Normally, the size effect is the strongest and produces an attractive force between the dislocation core and the solute atoms as a result of the elastic distortion of the core which can accommodate solute atoms of sizes different from those of the solvent matrix. The shear modulus difference becomes significant when the solvent and solute atoms show similar size. In this case, the difference of the shear modulus of the matrix with solute concentration leads to additional interaction energy as a result of the dependence of flow stress on the shear modulus. During plastic deformation, the solute atoms tend to confine the dislocations to slip planes, decrease their capacity to recover dynamically by local climb and cross-slip, hinder the formation of 'clean' cell structures and thereby increase the dislocation density for a given amount of deformation [5].

Two different mechanisms have been proposed to explain dislocation-solute interactions: 1) solute atoms, which drag/lock the dislocations and 2) stationary solute atoms acting on moving dislocations as friction. If the solutes can diffuse to the suitable positions near dislocations (at relatively high temperature), the locking mechanism is preferred, while in low temperature regions, solutes are more stationary and act like obstacles on moving dislocations [9].

2.1.3 Precipitation hardening

Alloying elements in the form of second phase particles usually harden the material by creating an additional barrier to dislocation motion. The second phase particles will lie across the passage of dislocation movement and force the dislocations to expend additional energy either by cutting the particle or by looping around them [5]. The former case happens when precipitates are coherent with the matrix while the later occurs when precipitate particles are incoherent with the matrix lattice planes. In this case, the dislocations have to bypass the obstacles (precipitates) by bowing around them or by cross slip and climb to an alternative slip system. Hence, the presence of precipitates increases the dislocation density due to the accumulation of geometrically necessary dislocations around these particles [2].

2.1.4 Softening Mechanisms

Increase in dislocation density within grains of any hot deformed metal is continually counteracted by softening processes. The softening processes are generally divided into dynamic recovery (DRV) and dynamic recrystallization (DRX) [2, 5, 10].

2.1.4.1 Dynamic Recovery

Dynamic recovery consists of all the processes that lead to annihilation of dislocations and rearrangement of the remaining dislocations into low angle grain boundaries and cell/subgrain structures. In metals of high stacking fault energy, such as aluminum and its alloys, dislocation climb and cross slip happen readily to provide a significant amount of

recovery. Therefore, in these materials dynamic recovery tends to be the main softening mechanism which occurs during elevated temperature deformation [2, 10, 11].

Dynamic recovery is a thermally activated process which results in dislocation movement and rearrangement. Both the strain rate and deformation temperature have a significant influence on the dynamic recovery rate which in turn determines the steady state flow stress. The dynamic recovery rate increases with increasing temperature and decreasing strain rate [2, 3, 11]. Figure 2.1 schematically illustrates a series of microstructural evolutions occur during dynamic recovery [2].

In the early stages of the hot deformation process, due to a high rate of work hardening, dislocation density and flow stress increase rapidly. An increase in dislocation density raises the driving force for dynamic recovery which leads to the annihilation of some dislocations and the rearrangement of others to form low angle boundaries and a subgrain structure. Beyond a certain strain, the rate of work hardening and recovery become equal which results in a steady state flow stress.

Figure 2.2 illustrates a typical microstructure of a hot deformed aluminum alloy as it undergoes dynamic recovery. The grain boundaries migrate locally in response to the boundary tensions of the substructure and to local dislocation density variations, and become serrated with a wavelength which is closely related to the subgrain size [2, 5].

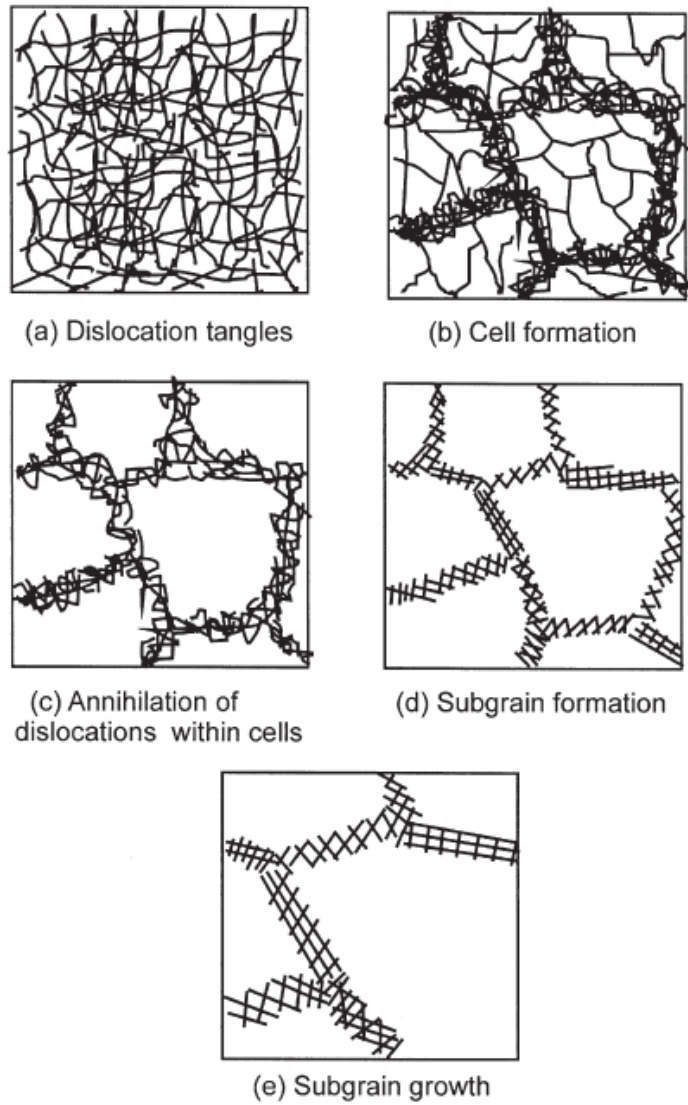


Fig. 2.1. Various stages in the recovery of plastically deformed material [2].

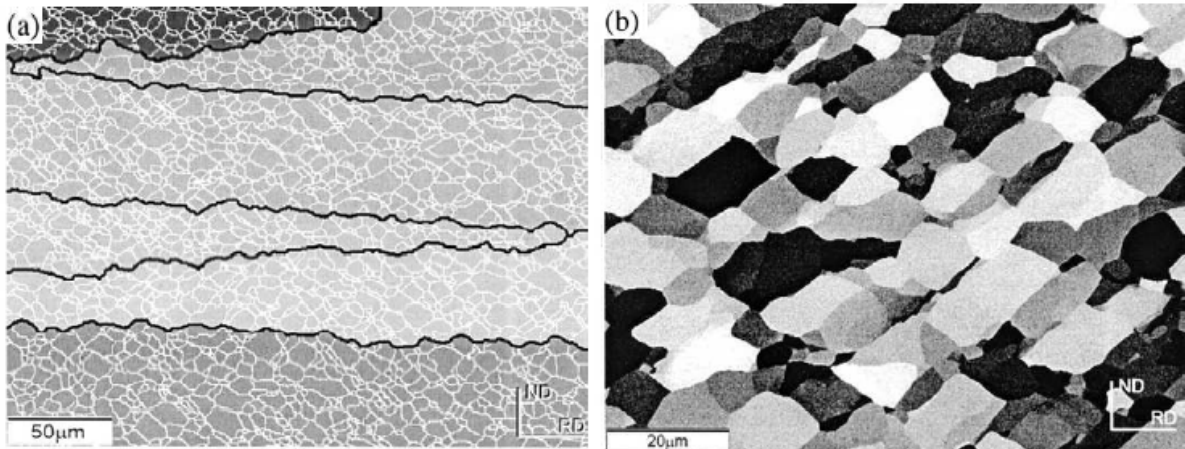


Fig. 2.2. Microstructure in ND-RD plane of Al-0.1%Mg deformed in plane strain compression at $T = 350^{\circ}\text{C}$, $\dot{\epsilon} = 0.25 \text{ s}^{-1}$ and $\epsilon = 1$. (a) EBSD map showing LAGBs (white) and serrated HAGBs (black), (b) SEM channelling contrast image showing the subgrain structure [2].

2.1.4.2 Dynamic Recrystallization

In the hot deformation of metals and alloys with low or medium stacking fault energy such as copper, nickel and austenitic iron, dynamic recovery proceeds slowly and dislocation density rises drastically. At some point this high dislocation density can provide enough driving force, allowing the initiation of recrystallization during hot deformation which is known as dynamic recrystallization (DRX). DRX is barely observed in metals and alloys with high stacking fault energy such as aluminum and its alloys due to the high rate of dynamic recovery that inhibits the accumulation of sufficient dislocations to sustain dynamic recrystallization [10, 11]. However, there are some reports of dynamic

recrystallization in aluminum of very high purity and aluminum alloys containing large particles such as Al-5Mg-0.8Mn [10, 12].

Two types of dynamic recrystallization have been reported thus far: discontinuous dynamic recrystallization (DDRX) and continuous dynamic recrystallization (CDRX) [2, 10, 13]. Classical DDRX, which has clear nucleation and growth stages, can take place in high purity aluminum [14, 15]. The nucleation of DRX is a critical factor in determining both the size and orientation of final grains. The preferred sites for nucleation are defects, such as grain boundaries as well as dislocations and deformation bands that are formed during deformation. The nucleation must reach a critical size before it grows and must be bounded by high angle boundaries since growth is achieved by grain boundary migration [10]. Furthermore, there is some evidence for particle stimulated dynamic recrystallization in aluminum alloys containing large particles [12, 16, 17]. During the hot deformation of an alloy containing large particles ($> 1\mu\text{m}$), the dislocations drastically accumulate in the vicinity of the large particles. The higher density of dislocations around the particles can lead to the nucleation of a new subgrain with high angle boundaries in the surrounding area of these particles. The newly formed subgrains will then grow and consume the surrounding subgrains. This is known as a particle stimulated nucleation (PSN) [10].

Recent studies show that in certain conditions a microstructure of high angle grain boundaries could gradually develop during elevated temperature deformation in ways other than DDRX which generally classified as a continuous dynamic recrystallization (CDRX). Dynamic recrystallization by progressive lattice rotation and geometry dynamic

recrystallization (GDRX) are the most commonly reported processes that can be considered as CDRX [2].

There is significant evidence that in some materials new grains with high angle boundaries may be developed during hot deformation by the progressive rotation of subgrains adjacent to the original grain boundaries. This phenomenon is mostly observed in aluminum alloys in which dislocation motion is hindered by solute drag such as Al-Mg alloys [18, 19]. The mechanism of the rotation recrystallization involves an interaction between grain boundary deformation and the grain boundary serrations as shown in Figure 2.3[2]. High angle grain boundaries (HAGB) develop serrations due to interaction with the deformation substructure (Figure 2.3(a)). Grain boundary sliding can then only take place on parts of the boundary, e.g. A, while other parts, e.g. B, have to accommodate the strain by plastic deformation (Figure 2.3 (b)), leading to shear and local lattice rotation as shown in figure 2.3 (c) [2].

Geometric dynamic recrystallization occurs on materials which are subjected to a large reduction in cross section. At low plastic strains the original grains boundaries become serrated and subgrain boundaries form. When the strains increase the serrated high angle boundaries become progressively perpendicular to the force direction and grains become elongated. Eventually, grain boundary serrations on opposite sides of the grains begin to touch and annihilate each other, leading the grains to ‘pinch off’, as shown in Figure 2.4 [2, 3, 20]. There are some reports of the occurrence of GDRX in aluminum alloys such as Al-5Mg-0.6Mn and Al-3Mg-0.2Fe [20, 21].

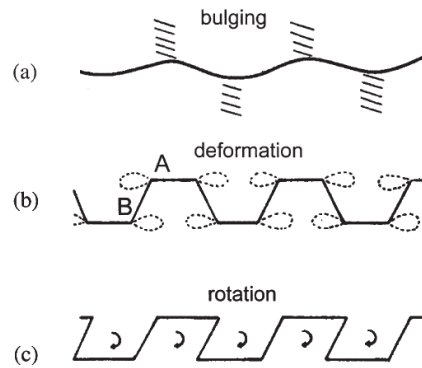


Fig. 2.3. Mechanism of DRX by progressive lattice rotation in Al-Mg alloys. (a) HAGB serrations form, (b) Grain boundary sliding occurs on horizontal boundaries, but slip occurs on bulged sections, leading to local lattice rotations associated with the bulges, (c) [2].

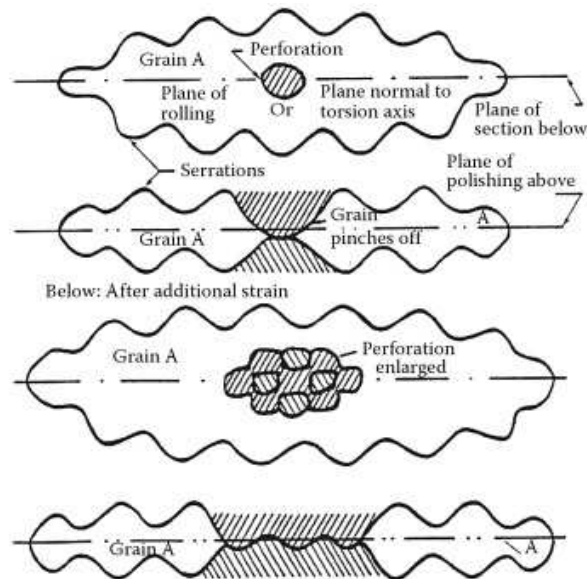


Fig. 2.4. When the grains are extremely thinned, they pinch off or perforate where opposite serration come into contact [3].

2.1.5 Dynamic recovery flow curves

In hot working tests at a constant temperature and strain rate, the stress-strain curve of a material undergoing dynamic recovery is typically characterized by a rise to a plateau followed by a constant or steady state flow stress as shown in Figure 2.5. The steady state flow stress gives evidence of constant dislocation density as a result of a balance between the rate of dislocation generation and annihilation [2, 3, 22, 23]. The generation rate is determined by the strain rate while the annihilation rate is a function of the dislocation density (and therefore the strain) and the ease of operation of recovery mechanisms is temperature-related [24]. Increasing DRV results in a decrease on flow stress and an increase in ductility [11].

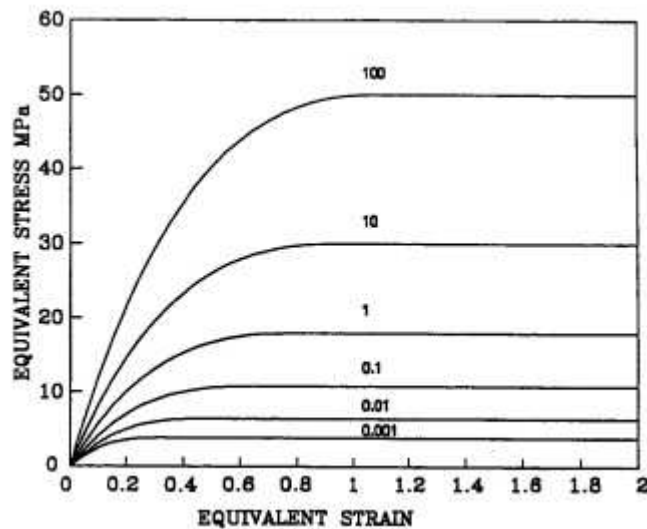


Fig. 2.5. Typical DRV stress-strain curves [22].

2.1.6 Dynamic recrystallization flow curves

The stress-strain curves for materials which undergo DRX normally show broad peaks followed by the steady state conditions as shown in Figure 2.6 [2, 3, 10]. In these materials strain hardening and DRV are the only mechanisms operating until near the peak stress, when the nucleation of DRX results in a rapid decrease in strain hardening to zero at the peak strain, and a further decrease in the flow stress as the recrystallized grains form with lower dislocation density and less strength [23]. At a low strain rate and high temperature, multiple peaks could appear at low strains [2].

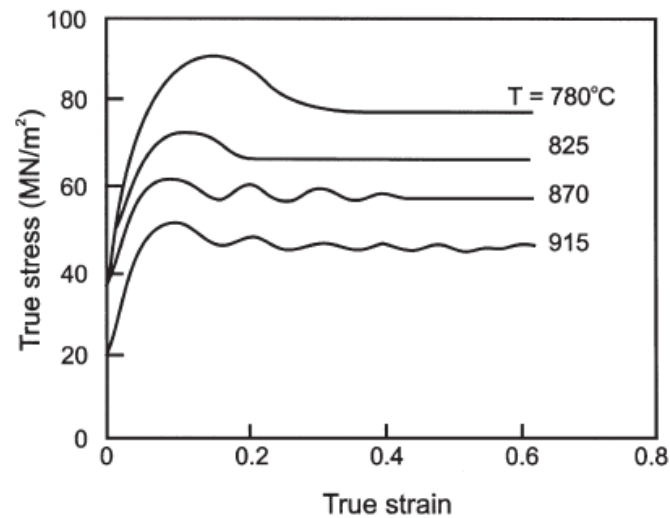


Fig. 2.6. Typical DRX stress-strain curves [2].

2.2 AA1xxx series aluminum alloys

The 1xxx series aluminum alloys are considered as the commercial purity aluminum, ranging from the baseline 1100 (99.00% min. Al) to the relatively purer 1050/1350 (99.50% min. Al) and 1175 (99.75 % min. Al). The wrought 1xxx series aluminum alloys are strain hardenable and offer excellent formability, corrosion resistance, and thermal and electrical conductivity. Typical applications include foil and strip for packaging, heat exchanger tubing and finstock, coaxial cable sheathing, chemical equipment, tank car or truck bodies and electrical conductors [25, 26].

2.2.1 Microstructure of AA1xxx series aluminum alloys

The 1xxx series alloys contain at least 99.0% aluminum with iron and silicon as the main alloying elements or impurities [27]. Since maximum solid solubility of Fe in aluminum is very low (~ 0.05 wt% at 650 °C), most of the iron combines with both aluminum and silicon to form secondary intermetallic phases [28, 29]. Comparing Si with Fe, Si has a higher solid solubility in aluminum which can reach 1.6 wt.% at 577 °C, so low levels of Si (0.1-0.2%) can easily dissolve in the Al matrix and iron aluminides. The Fe content, cooling rate and other impurities contents affect the type of constitutive particles, which form during solidification and casting. The type, size and distribution of the iron rich intermetallic phases have a significant influence on the properties of the alloy such as strength, ductility, hot workability, corrosion resistance and creep resistance. Furthermore, the solid solution level has a great impact on electrical conductivity and softening characteristics [27, 30, 31].

2.2.1.1 Binary Al-Fe phases

Figure 2.7 exhibits the Al rich corner of the equilibrium Al-Fe binary phase diagram. As seen, during the equilibrium solidification of Al-Fe alloys the θ - Al_3Fe intermetallic, which is also denoted as $\text{Al}_{13}\text{Fe}_4$, is formed by the eutectic reaction at 665°C and 1.8 wt% Fe [32]. Al_3Fe has a C-centered monoclinic crystal structure [33]. Al_3Fe normally forms relatively large angular precipitates in as-cast microstructures (Fig.2.8), which improve hardness but reduce formability and fatigue resistance [27]. The lattice parameters are: $a=1.5489\text{nm}$, $b=0.808\text{nm}$, $c=1.2476\text{nm}$ and $\beta=107^\circ43'$ [34].

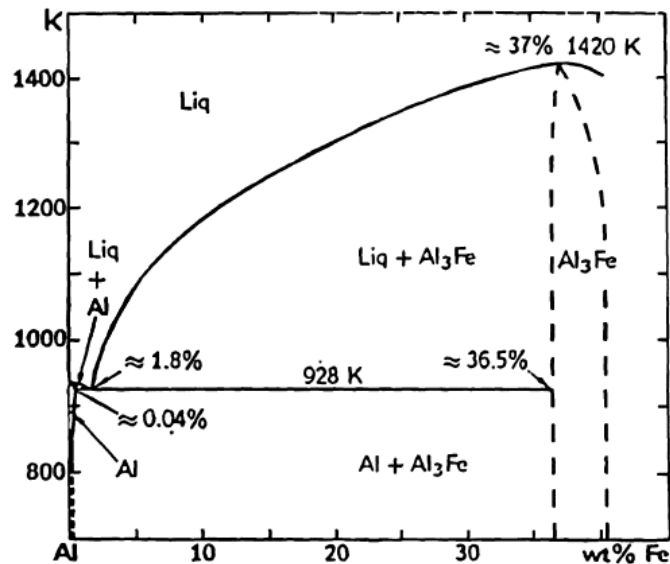


Fig 2.7. Al rich corner of the equilibrium Al-Fe binary phase diagram [27].

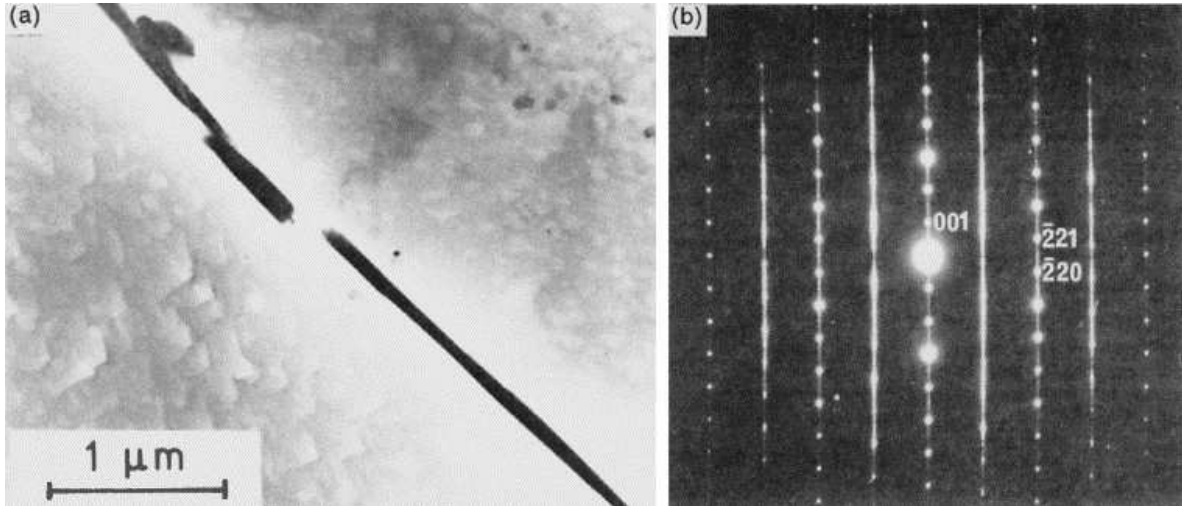


Fig. 2.8. (a) Al_3Fe at grain boundaries in cast ingot under TEM and (b) typical $[110]$ diffraction pattern of a faulted Al_3Fe crystal [27].

Reaching an equilibrium condition is almost impossible in real industrial production, so in the non-equilibrium condition a range of thermodynamically metastable phases such as Al_6Fe , Al_mFe , Al_xFe can be formed [27, 35-37].

Al_6Fe is often found in the relatively rapidly solidified regions of Al-Fe alloys and it has a flake-like morphology with several short wings. Chen's investigation also revealed that in three-dimensions, Al_6Fe has a curved plate-like morphology with a number of rod-like branches [38]. Figure 2.9 (a) exhibits a typical morphology of this phase on a deep-etched sample. Al_6Fe has a C-centered orthorhombic crystal structure [29]. The lattice parameters are: $a=0.6492\text{nm}$, $b=0.7437\text{nm}$ and $c=0.8788\text{nm}$ [34]. The formation of Al_6Fe is impeded in Al-Fe-Si alloys. In contrast, it is more stable in Mn containing Al alloys [27].

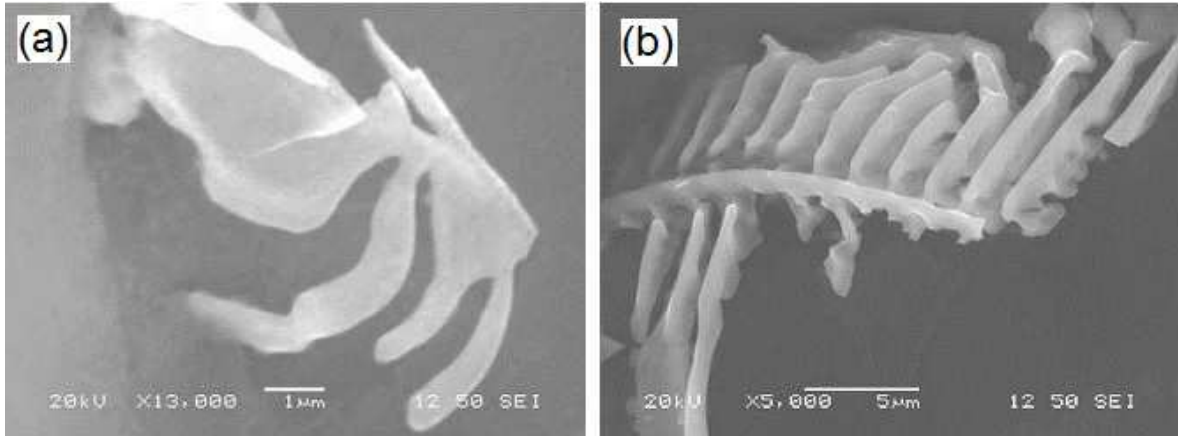


Fig. 2.9. Fe intermetallic phases morphology (deep-etching) under SEM (a) Curved plates like Al_6Fe phase and (b) fine feathery like Al_mFe phase [39].

Metastable Al_mFe phase forms at regions with higher cooling rates than those at which Al_6Fe and Al_3Fe form. The Al_mFe exists over a range of compositions, with the value of m quoted from 4 to 4.4. It has a body-centered tetragonal crystal structure with mostly dendrite-like morphology [27, 29]. 3-D observation has also shown that it has a feathery-like morphology with many fibers growing in various directions (Fig 2.9 (b)) [38]. The lattice parameters of this phase are: $a=0.884\text{nm}$ and $b=c=3.16\text{nm}$ [34].

2.2.1.2 Ternary Al-Fe-Si phases

Figure 2.10 illustrates the liquidus projection in the Al corner of the Al-Fe-Si ternary phase diagram [27]. Two ternary phases, α - $\text{Al}_8\text{Fe}_2\text{Si}$ and β - Al_5FeSi , can be formed during the equilibrium solidification of dilute Al-Fe-Si alloys. As seen each phase can exist over a range of compositions. In the low Si content Al alloys, the β phase cannot form under DC-casting conditions, therefore only ternary phase α along with binary phases such as Al_3Fe ,

Al_6Fe and Al_mFe form in these alloys. Figure 2.11 shows the composition ranges of the common iron rich intermetallics found in Al-Fe-Si alloys.

The α -phase can adopt different crystal structures. In the equilibrium condition the α -phase has a hexagonal crystal structure[40] however additions of V, Cr, Mn, Cu, Mo and W promote a body-centred cubic structure for the α -AlFeSi phase. The promotion and stabilization of the cubic α phase by trace elements common in commercial purity alloys leads to the cubic form being the one which is commonly found in commercial alloys[27]. The α -phase illustrates a dendritic morphology which is generally described as Chinese script under optical microscope imaging. For the hexagonal structure the unit cell parameters are $a = 1.24 \text{ nm}$, $c = 2.623 \text{ nm}$ [34].

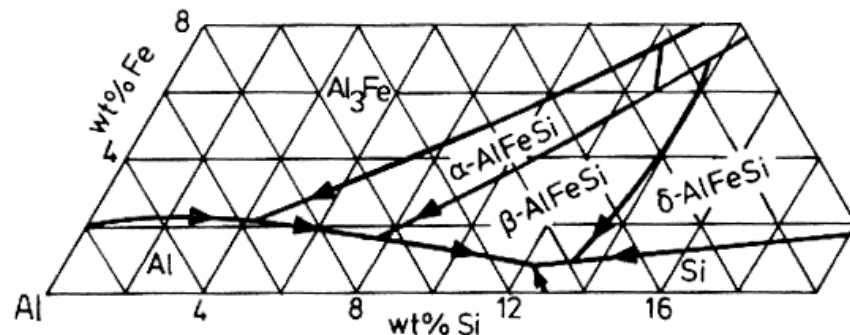


Fig. 2.10. Liquidus projection in the Al corner of the ternary Al-Fe-Si phase diagram [27].

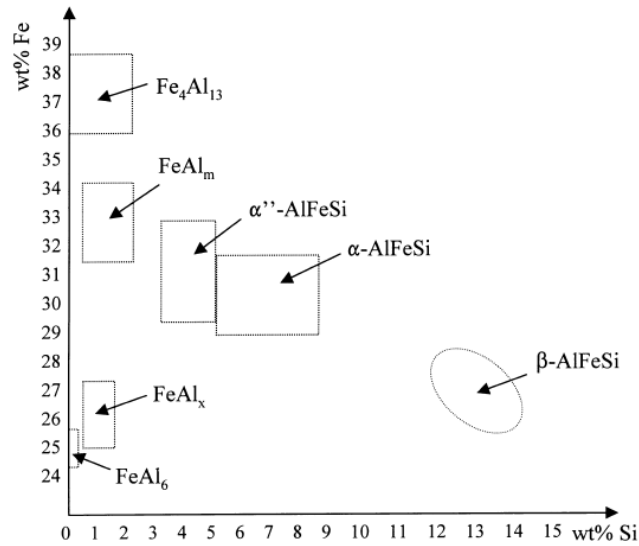


Fig. 2.11. Compositions of the common binary and ternary compounds found in Al-Fe-Si alloys [41].

2.2.1.3 Transformation of metastable phases

All commercially pure aluminum grades contain very small amounts of insoluble elements that segregate to cell or grain boundaries in cast materials. In the as-cast microstructure different iron intermetallic such as Al_mFe , Al_6Fe , Al_3Fe , $\text{Al}_8\text{Fe}_2\text{Si}$ (denoted as α -phase) and body-centered cubic structure for the α -phase known as α_c can be observed [27, 35-37].

Many authors, such as Kosuge [42], Griger et al. [43], Lendvai et al. [44, 45] and Murgas et al. [46], have reported transformations of metastable phases during homogenization of Al-Fe and Al-Fe-Si alloys in the temperature range of 350-650° C. They have observed that all the metastable phases, Al_mFe , Al_6Fe and also α -AlFeSi transform to

equilibrium Al_3Fe phase after homogenization at a sufficiently high temperature for an appropriate time. Kosuge et al. [42] studied the effect of homogenization in the range of 300-640°C on the microstructure of Al-Fe alloys (Al-0.6Fe and Al-0.8Fe-0.1Mg) and found that with increasing homogenization temperature the proportion of Al_mFe and Al_6Fe after one hour began to reduce from 500°C, and had totally converted to Al_3Fe by 640°C. Figure 2.12 illustrates the effect of homogenization temperature on the normalized intensities of X-ray peaks from Al_mFe , Al_6Fe and Al_3Fe . Kosuge and co-workers observed that the Al_mFe and Al_6Fe particles dissolved into the aluminum matrix while Al_3Fe nucleated and grew remotely from the dissolving particles. From this microstructural observation he proposed that transformation proceed via diffusion of Fe from the dissolving metastable phases to the precipitating Al_3Fe . Kosuge also studied the effect of Si on the transformations of metastable Al-Fe phases and found that the transformation of both Al_mFe and Al_6Fe phases took place more rapidly in the alloys containing silicon [42]. The mechanism of transformation of $\alpha\text{-AlFeSi}$ to Al_3Fe seems to be similar to that for the transformation of Al_mFe and Al_6Fe . Grieger et al. [43] reported that during transformation the Chinese script $\alpha\text{-AlFeSi}$ phases first coarsened and then dissolved, while Al_3Fe precipitated from the solid solution as acicular precipitates.

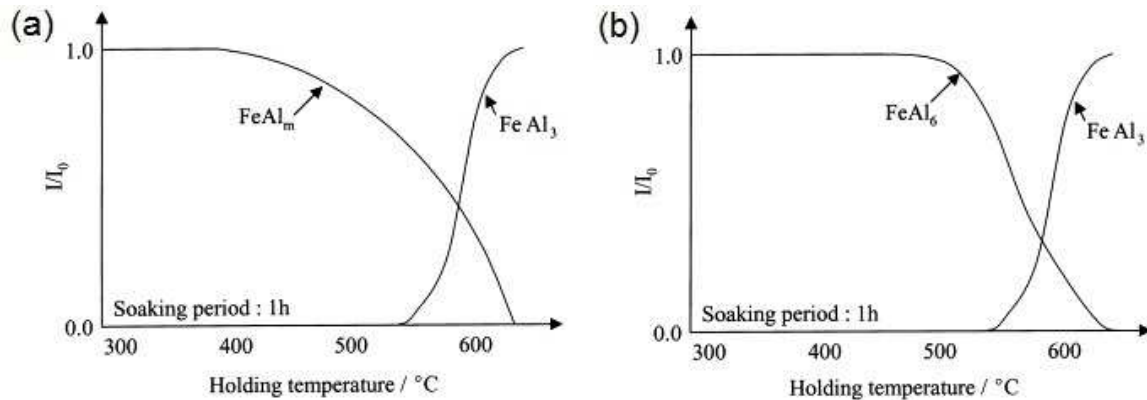


Fig.2.12. Variation of normalized X-Ray intensity of Al_mFe , Al_6Fe and Al_3Fe with homogenization temperature in (a) Al-0.8Fe and (b) Al-0.6Fe alloys [42].

2.2.2 Hot deformation behavior of AA1xxx aluminum alloys

Hot deformation processes are of great industrial importance since most metals show low flow stress and high ductility at high temperatures ($\geq 0.5 T_M$). In addition to changing the shape, hot working plays a significant role in improving the structure for further forming operations and for service [3, 5]. Therefore, it should be carried out as economically and effectively as possible. The ease of working, called the workability, is measured in terms of the power consumed and the rate and size of the possible reductions [3]. In order to have the best combination of processability and physical and mechanical properties, it is important to understand the hot workability and microstructural evolution of 1xxx aluminum alloys during hot deformation.

Dynamic recovery is the main softening mechanism during hot deformation of aluminum and its alloys, which exhibit high stacking fault energy (SFE). In these alloys,

the strain hardening is alleviated by the climb and glide of dislocations to mutually annihilate or rearrange into simple low energy arrays [2]. Previous studies have shown that chemical composition, initial microstructure and thermomechanical parameters have significant effect on the softening behavior and microstructural evolution of aluminum alloys. J.C. Blade [47] investigated the effect of additions of Fe and Si to super-purity aluminum and the variations of the Fe and Si contents of commercial purity aluminum on the recrystallization behaviors of these alloys after 50% hot rolling and a 30sec delay before quenching. He found that in commercially pure aluminum the extent of recrystallization was reduced by increasing the total iron and silicon content and, for most conditions, by increasing the Fe/Si ratio. Although both Fe and Si showed a retarding influence on recrystallization, the effect of Fe was more significant. Vandermeer's [48] investigation on the static recrystallization behavior of commercial purity aluminum- alloy AA1050 showed that Al_3Fe precipitate particles have a profound effect on the recrystallization kinetics of this alloy. Indeed, large non-deformable Al_3Fe particles were the preferred sites where the new recrystallized grains appeared upon annealing. Unlike static recrystallization, iron intermetallic particles such as Al_3Fe (as nucleation sites) cannot promote dynamic recrystallization in hot deformed aluminum alloys and, in commercial purity aluminum, DRV is the only operative dynamic restoration mechanism [3, 11]. Yamagata [15] compared the restorative process of high purity aluminum (99.999%Al) to that of 99.99% aluminum and found that dynamic recrystallization only occurred in the high purity aluminum while 99.99% aluminum experienced dynamic recovery. McQueen et al. [11, 22, 49] also showed that dynamic recrystallization could not occur in commercially pure

aluminum (1xxx alloys) and that dynamic recovery was the sole restoration mechanism during hot deformation.

The most basic parameter for characterizing the plastic deformation properties of alloys is the flow stress [50]. McQueen et al.'s [11] investigation showed that the hot deformation of commercial aluminum and its alloys in the range from 10^{-2} to 10^2 s⁻¹ above 350 °C leads to a steady state flow stress at constant strain rate and temperature. The steady state regime gives evidence of a constant dislocation density as a consequence of a balance of the work hardening and the dynamic softening. Previous studies also showed that the flow stress during hot deformation of commercially pure aluminum alloys decreases with increasing deformation temperature and decreasing strain rate [11, 22, 51].

Commercial 1xxx aluminum alloys exhibit higher strength and work hardening than high purity aluminum. Zhao et al. [52] reported that Fe and Si play a major role in the strength and work hardening of commercial 1xxx alloys and that the contribution from the other impurities is negligible. The flow stress of commercial purity aluminum is related to the strain rate and temperature by the hyperbolic sine equation. The activation energy for hot working varies with the composition, the microstructure as well as the deformation parameters and has been reported from 152 to 175 kJ/mol for commercial purity aluminum, rising with alloy content [3, 4, 22, 23, 49, 53]. The activation energy for pure Al is about 140-156 kJ/mol [3, 4, 22, 23].

2.2.2.1 Substructure evolution during hot deformation

Substructure development in materials with high stacking fault energy such as aluminum takes place as dislocations become entangled during strain hardening and then form a three dimensional subgrain structure, characterized by low or medium misorientation angles and relatively low interior dislocation densities [7, 54]. The equilibrium subgrain size increases with increasing deformation temperature and decreasing strain rate and is largely independent of strain [55, 56]. During large strains, the subgrains do not elongate with the grains as the cell walls continually decompose and reform in a process named repolygonization, maintaining characteristic wall spacing and dislocation arrays [3, 57, 58]. When the temperature and strain rate, as the controlling parameters, are changed a new equilibrium structure will develop which is independent of the previous one. The stable subgrain size d_s changes with the deformation conditions according to the following relationship [3, 49, 59-62]:

$$d_s^{-1} = a + b \log Z \quad (2.1)$$

where a and b are constants, and Z is the Zener-Holloman parameter ($Z = \dot{\epsilon} \exp(\frac{Q}{RT})$).

Figure 2.13 shows the effect of the Z parameter on the subgrain structure in the Al-0.65%Fe alloy. The micrographs show fine elongated subgrains at $300^\circ \text{C} / 0.1 \text{ S}^{-1}$ and well recovered subgrains at $500^\circ \text{C} / 0.1 \text{ S}^{-1}$.

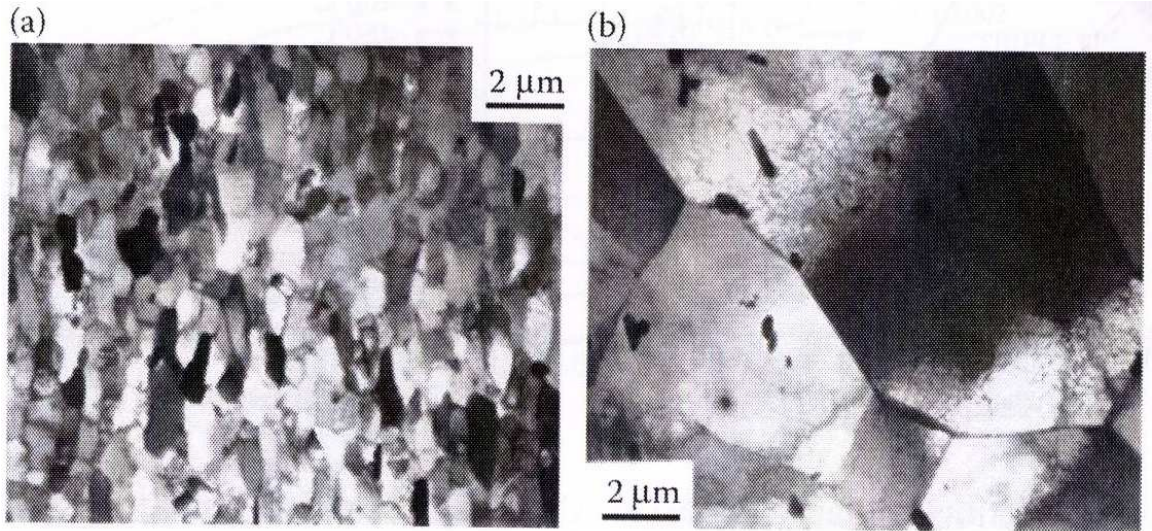


Fig. 2.13. TEM micrographs of subgrains structures in Al-0.65Fe alloy deformed at (a) $300^{\circ}\text{C}/0.1\text{ s}^{-1}$ and (b) $500^{\circ}\text{C}/0.1\text{ s}^{-1}$ [3].

2.2.2.2 *Effect of homogenization*

Homogenization before hot working has significant influence on the workability and the degree of microstructural evolution which occurs during hot deformation. The main purpose of homogenization is to shrink and spheroidize the constituent particles, remove nonequilibrium eutectics and particles, and eliminate coring by diffusion to achieve a material as uniform as possible. Reduction in the size of particles $>1\ \mu\text{m}$ can remove sites for recrystallization nucleation and the re-precipitation of a higher density of fine particles can restrain it further; on the other hand, the coalescence of small particles reduce their ability to hinder restoration [3].

Homogenization normally is able to improve ductility and reduce hot strength by up to 20% [3, 27, 63]. Prasad et al. [64] reported that a suitable homogenization treatment, which dissolved the intermetallic particles present at the grain boundaries, improves hot workability of as-cast AZ31 Mg-alloy by reducing the intercrystalline cracking and flow instability regimes. Totik et al. [63] showed that homogenization at 510 °C significantly improved the hot workability of AA 2014 alloy and resulted in the uniform workability of the tested ingots. Zhang et al. [65] studied the influence of the initial microstructure on the hot workability of a AA2219 aluminum alloy and found that the aged (535 °C for 10h following by natural aging in open air) microstructure produced the lowest hot deformation resistance and the solutionized (460 °C 10h) microstructure showed the highest deformation resistance under the same deformation conditions.

The effects of homogenization on hot workability of 1xxx series aluminum alloys are complex but in general, the particles formed during casting are re-dissolved during homogenization, while new particles precipitate from the supersaturated solid solution (more details can be found in section 2.2.1.3). The type, size, density and distribution of intermetallics as well as the solid solution level of alloying elements or impurities in 1xxx series aluminum alloys can be affected by the homogenization temperature and soaking time. Finding the proper homogenization treatment for certain chemical composition is, therefore, of great interest.

2.2.2.4 Effect of Mn

Small additions of transition elements such as manganese are often made to wrought aluminum alloys for the purpose of controlling dynamic softening processes. In hot deformation of aluminum alloys, the softening processes such as DRV, DRX and grain growth can be affected by the presence of transition elements in either solid solution or as precipitates.

Generally, Mn in the presence of other elements of low solubility such as iron and silicon forms coarse constituent particles and fine dispersoids that serve as obstacles against grain boundary migration and dislocation movement [54, 66]. In Al-Fe-Mn alloys the precipitation of $Al_6(Mn,Fe)$ particles are favorable while $\alpha-Al(Mn,Fe)Si$ particles are formed in alloys containing Si [67]. Mn also has a significant influence on the strength of aluminum alloys when presents in solid solution [66].

Zhang et al. [68] reported that the alloy Al-0.9Mn, compared to pure aluminum, was significantly stronger in hot working over the temperature range of 200-500°C due to the presence of fine and uniformly distributed Mn containing dispersoid. These fine particles with a sufficient density stabilized the substructure and resulted in higher strength and activation energy. Furu et al. [54] showed that an addition of 1%Mn produced a solute drag effect during hot deformation of aluminum and resulted in a smaller subgrain size and lower misorientation angle. Recent investigations suggested that the solute hardening effect of Fe and Mn in aluminum are absolutely significant and are among the strongest [69]. Ryen et al. [66] reported that Mn in solid solution had a significant effect on the strength

and work hardening rate of both commercial and high purity aluminum alloys. The solute hardening rate was about 50% stronger in the commercially pure aluminum alloys compared to the high purity alloys. This strong strengthening effect was considered to be attributed to the clustering effect between Mn and trace elements in solid solution [66].

2.2.2.4 Effect of Cu

Copper is often added to improve aluminum's mechanical properties. Addition of copper increases the strength, hardness, fatigue and creep resistance of aluminum alloys [25, 70]. Mechanical improvement resulting from copper addition strongly depends on copper content and the form in which it is present (in solid solution or as precipitates). Aluminum alloys containing a high amount of copper (≥ 2 wt.%) form an important group of alloys which respond to solution treatment and subsequent aging with an increase in strength and hardness by formation of Al_2Cu called θ as precipitate. When the amount of copper is low (< 1 wt.%) because it has relatively high solubility in aluminum 5.7% at 550°C [8, 66] copper can be present in solid solution. Cu in solid solution can increase strength by interacting with dislocations through atmospheres which either pin static dislocations or at high temperature are dragged by gliding dislocations [1, 9]. Considering the role of copper in corrosion resistance, the most recent work shows a rather favorable influence while the copper remains in solid solution [71].

Unfortunately, no systematic investigation has been performed to study the effect of the minor addition of Cu on the hot deformation behavior and microstructural evolution of 1xxx series aluminum alloys.

2.3 Modeling the high temperature flow behavior of metals and alloys

The flow behavior of crystalline materials during hot deformation is complex. The work hardening and dynamic softening mechanisms are both strongly affected by a number of factors, such as chemical composition, forming temperature, strain rate and strain [4, 22]. Therefore, prediction of the hot deformation behavior of metals and alloys under various thermomechanical conditions is of great technical interest. Constitutive models are normally used to describe high-temperature flow behavior. These models are mainly divided into three categories: 1) analytical [72-74], 2) phenomenological [75-77] and 3) artificial neural network (ANN) [78-81].

Analytical constitutive models are based on the physical aspects of the material's behavior and require comprehensive understanding of the underlying mechanisms that control the material's deformation. In addition, there are many independent parameters in the analytical constitutive equations that have to be determined through materials testing. Phenomenological constitutive models are the classical approach for modeling the forming processes of materials at high strain rates and temperatures. These models describe the flow behavior based on the empirical observations using some mathematical functions to consider the influence of the deformation variables on the flow stress of metals and alloys [82].

The application of an ANN in a hot working area is relatively new. It is, however, becoming popular due to its great ability to simulate complex and nonlinear problems, which are difficult to simulate by using existing mathematical approaches. The most

important advantage of ANNs is that they do not require postulation of a mathematical model at the outset or the identification of its parameters. ANNs learn from examples and recognize patterns in a series of input and output data without the need for any prior assumptions about their nature and interrelations [83, 84]. Recently ANNs have been successfully applied to model the high-temperature flow behavior of stainless steels [79, 83-85], aluminum alloys [78, 80, 86], magnesium alloys [87], zirconium alloys [88], titanium alloys [89, 90] and Al-base metal matrix composites [91].

2.3.1 Phenomenological constitutive equations

Phenomenological constitutive equations are widely used to model the hot deformation behavior of metals and alloys. At an elevated temperature, the strain rate ($\dot{\epsilon}$) is related to the temperature and the flow stress by the Arrhenius type equation [4, 82, 92-95]:

$$\dot{\epsilon} = Af(\sigma)\exp\left(-\frac{Q}{RT}\right) \quad (2.2)$$

where $\dot{\epsilon}$ is the strain rate (s^{-1}), A is a constant, Q is the activation energy for hot deformation ($KJ\ mol^{-1}$), R is the universal gas constant ($8.314\ J\ mol^{-1}\ K^{-1}$), T is the absolute temperature (K) and $f(\sigma)$ is the stress function which can be expressed as [23, 96-101]:

$$f(\sigma) = \begin{cases} \sigma^{n_1} & \alpha\sigma < 0.8 \\ \exp(\beta\sigma) & \alpha\sigma > 1.2 \\ [\sinh(\alpha\sigma)]^n & \text{for all } \sigma \end{cases} \quad (2.3)$$

where σ is the flow stress (MPa), n_1 , β and n are material constant and $\alpha = \beta/n_1$ [98-100] is a stress multiplier. Substituting the suitable function of $f(\sigma)$ into Eq. (1) leads to the power law, exponential and hyperbolic sine law equations, respectively:

$$\dot{\epsilon} = A_1 \sigma^{n_1} \exp\left(-\frac{Q}{RT}\right) \quad (2.4)$$

$$\dot{\epsilon} = A_2 \exp(\beta\sigma) \exp\left(-\frac{Q}{RT}\right) \quad (2.5)$$

$$\dot{\epsilon} = A[\sinh(\alpha\sigma)]^n \exp\left(-\frac{Q}{RT}\right) \quad (2.6)$$

where A_1 and A_2 are the material constants. Generally, the power law equation breaks down at high stress values, and the exponential equation breaks down at low stress values. However, the hyperbolic-sine law is suitable for constitutive analysis over a wide range of temperatures and strain rates [4, 92-95].

Furthermore, the effect of the temperature and the strain rate on the hot-deformation behavior could be represented by the Zener-Holloman parameter (Z) in an exponential equation [3, 51, 53, 75, 95, 102]:

$$Z = \dot{\epsilon} \exp\left(\frac{Q}{RT}\right) \quad (2.7)$$

2.3.2 Artificial neural network (ANN)

The artificial neural network model has been developed in an attempt to emulate the organizational skills and process abilities of the mammalian brain. An ANN consists of processing units (artificial neurons) grouped into layers and related to each other by parallel

connections. The strength of these interconnections is regulated by the weight related to them. In every network, the first and last layers are input and output layers while all the layers in between are termed as the hidden layers. The number of layers, number of neurons in each layer and the nature of transfer functions are the most important parameters that should be carefully considered during development of each ANN. The number of neurons in the input and output layers shows the number of variables employed in the prediction and the number of variables to be predicted, respectively. To establish the relationships between the inputs and outputs, neurons in the hidden layers must perform the intermediate computations. The number of hidden layers and the number of neurons in each layer are not predetermined and have to be defined by the desired accuracy in the neural network predictions. However, though there is no theoretical limit on the number of hidden layers there is, generally, just one or two. A maximum of three hidden layers are enough to solve problems of any complexity [85]. Figure 2.14 illustrates a typical multilayer feed-forward ANN with a single hidden layer.

In the feed forward neural network, every neuron of a certain layer is connected to all the neurons of the layer next to it. Each of the neurons receives inputs and generates a single output. The inputs can be raw data or the output of other neurons and have an associated weight indicating the strength of the connections between correspondent neurons. The output can also be the final output or it can be used by the next neurons.

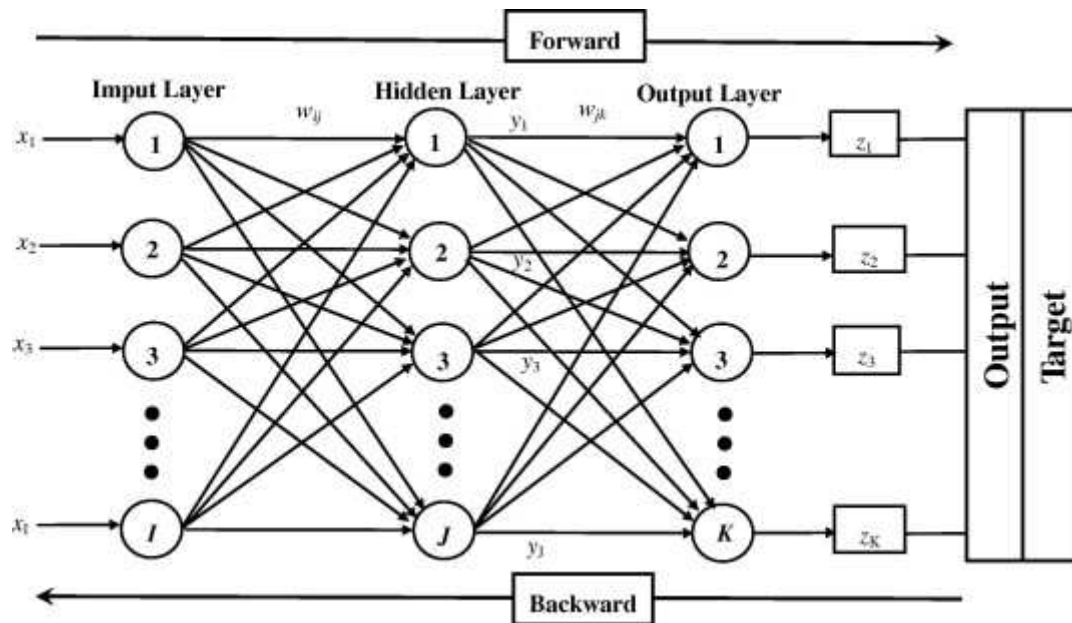


Fig.2.14. Schematic structure of an artificial neural network [85].

The transformation function defines the relationships between the inputs and the final output of the neurons. Various transformation functions can be used as the neurons activation function. However, as mentioned above, the careful selection of this function can have a significant impact on the accuracy of the network. The differentiable sigmoid function, given by equation 2.8, is the most popular transfer function used in back propagation networks, as shown in Fig.2.15 [103].

$$F(x) = \frac{1}{1 + \exp(-x)} \quad (2.8)$$

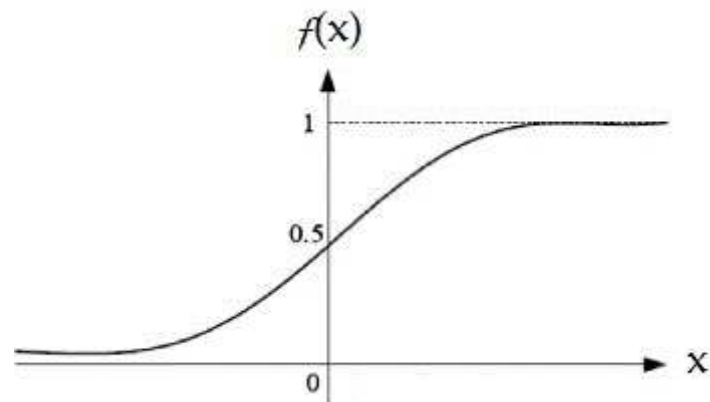


Fig.2.15. Shape of sigmoid function [85].

Once the network is designed, training of the network needs to be done using an appropriate algorithm such as back propagation, quasi-Newton, Levenberg-Marquardt algorithms and so on [103]. Network training is a process by which the connection weight and bias on an ANN are adapted through a repetitive process of computation and comparison. The most important objective is to minimize the difference between the predicted and the desired output by adjusting the weights and biases on all the inputs. The learning process is usually attained on a set of data known as "training data". Training data is a set of known inputs and outputs that illustrate the correct solution to the problem. Several iterations of the complete training data are required to produce a consistent set of weights and biases [103]. A back propagation algorithm is the most popular learning algorithm which is used in many various engineering applications.

Since most of the training algorithms are sensitive to the scale of data in order to ensure the learning efficiency of the algorithm and to prevent a specific factor from

dominating learning for the model, both input and output data are generally normalized within the range of 0-1. The following equation is widely utilized for unification [78, 80].

$$X' = 0.1 + 0.8 \times \left(\frac{X - X_{\min}}{X_{\max} - X_{\min}} \right) \quad (2.9)$$

where X is the original data, X_{\min} and X_{\max} are the minimum and maximum value of X , and X' is the unified data corresponding to X . Finally, once the ANN is trained, statistical performance measures can be used to evaluate the performance of the proposed network.

References

- [1] H.J. McQueen, Metal forming: Industrial, mechanical computational and microstructural, J. Mater. Process. Technol., 1993, 37, pp.3-36.
- [2] F.J. Humphreys, M. Hatherly, Recrystallization and related annealing phenomena, Second ed. Oxford, Elsevier Ltd., 2004.
- [3] H.J. McQueen, S. Spigarelli, M.E. Kassner, E. Evagelista, Hot deformation and processing of aluminum alloys. Florida, CRC Press, 2011.
- [4] H.J. McQueen, N.D. Ryan, Constitutive analysis in hot working, Mater. Sci. Eng. A, 2002, 322, pp.43-63.
- [5] B. Verlinden, J. Driver, I. Samajdar, R.D. Doherty, Thermo-mechanical processing of metallic materials. Oxford, UK, Elsevier, 2007.
- [6] J.E. Hatch, Aluminum: properties and physical metallurgy. Metals Park, OH, ASM, 1984.
- [7] O. D. Sherby, R. H. Klundt, A.K. Miller, Flow Stress, subgrain size, and subgrain stability at elevated temperature, Metall. Trans. A, 1977, 8, pp.843-50.
- [8] M. Spittel, T. Spittel. Flow stress of light metal alloys. In: Warlimont H, editor. Part 2: Non-ferrous Alloys - Light Metals: Springer Berlin Heidelberg; 2011, pp. 19-53.
- [9] P. Haasen. Physical metallurgy. In: R.W. Chan, Haasen P, editors., 4th ed., Elsevier ltd.; 1996, pp. 2009-68.
- [10] R.D. Doherty, D.A. Hughes, F.J. Humphreys, J.J. Jonas, D.J. Jensen, M.E. Kassner, et al., Current issues in recrystallization: a review, Mater. Sci. Eng. A, 1997, 238, pp.219-74.

- [11] H.J. McQueen, W. Blum, Dynamic recovery: sufficient mechanism in the hot deformation of Al, *Mater. Sci. Eng. A*, 2000, 290, pp.95-107.
- [12] H.J. McQueen, E. Evangelista, J. Bowles, G. Crawford, Hot deformation and dynamic recrystallization of Al-5Mg-0.8Mn alloy, *Metal Sci.*, 1984, 18, pp.395-402.
- [13] S. Gourdet, F. Montheillet, An experimental study of the recrystallization mechanism during hot deformation of aluminium, *Mater. Sci. Eng. A*, 2000, 283, pp.274-88.
- [14] D. Ponge, M. Bredehöft, G. Gottstein, Dynamic recrystallization in high purity aluminum, *Scripta Mater.*, 1997, 37, pp.1769-75.
- [15] H. Yamagata, Dynamic recrystallization and dynamic recovery in pure aluminum at 583K, *Acta Metall. Mater.*, 1995, 43, pp.723-9.
- [16] F.R. Castro-Fernandez, C.M. Sellars, Static recrystallisation and recrystallisation during hot deformation of Al-1Mg-1Mn alloy, *Mater. Sci. Technol.*, 1988, 4, pp.621-7.
- [17] T. Sheppard, M.G. Titcher, Development of duplex deformation substructure during extrusion of a commercial Al-5Mg-0.8Mn alloy, *Met. Sci.*, 1980, 14, pp.579-89.
- [18] K.J. Gardner, R. Grimes, Recrystallization during hot deformation of aluminum alloys, *Met. Sci.*, 1979, 13, pp.216-22.
- [19] M.R. Drury, F.J. Humphreys, The development of microstructure in Al-5%Mg during high temperature deformation, *Acta Metall.*, 1986, 34, pp.2259-71.
- [20] W. Blum, Q. Zhu, R. Merkel, H.J. McQueen, Geometric dynamic recrystallization in hot torsion of Al-5Mg-0.6Mn (AA5083), *Mater. Sci. Eng. A*, 1996, 205, pp.23-30.
- [21] A. Gholinia, F.J. Humphreys, P.B. Prangnell, Production of ultra-fine grain microstructures in Al-Mg alloys by conventional rolling, *Acta Mater.*, 2002, 50, pp.4461-76.
- [22] H.J. McQueen, E. Evangelista, N. Jin, M.E. Kassner, Energy dissipation efficiency in aluminum dependent on monotonic flow curves and dynamic recovery, *Metall. Mater. Trans. A*, 1995, 26, pp.1757-66.
- [23] C.M. Sellar, W.J.M. Tegart, Hot workability, *Int. Met. Rev.*, 1972, 17, pp.1-24.
- [24] J.J. Jonas, C.M. Sellars, W.J.M. Tegart, Strength and structure under hot working conditions, *Metall. Rev.*, 1969, 14, pp.1-24.
- [25] J.R. Davis, Aluminum and aluminum alloys. Materials Park, OH, ASM International, 1993.
- [26] J.G. Kaufman, Introduction to aluminum alloys and tempers. Materials Park, OH, ASM International, 2000.
- [27] C.M. Allen, K.a.Q. O'reilly, B. Cantor, P.V. Evans, Intermetallic phase selection in 1XXX Al alloys, *Prog. Mater. Sci.*, 1998, 43, pp.89-170.
- [28] P. Liu, T. Thorvaldsson, G.L. Dunlop, Formation of intermetallic compounds during solidification of dilute Al-fe-Si alloys, *Mater. Sci. Technol.*, 1986, 2, pp.1009-18.

- [29] P. Skjerpe, Intermetallic phases formed during DC-casting of an Al-0.25 Wt Pct Fe-0.13 Wt Pct Si alloy, *Metall. Trans. A*, 1987, 18, pp.189-200.
- [30] P.E. Fortin, Factors influencing electrical conductivity and strength of aluminum and its alloys, *Can. Metall. Quart.*, 1972, 11, pp.309-15.
- [31] J.G. Morris, Dynamic strain aging in aluminum alloys, *Mater. Sci. Eng.*, 1974, 13, pp.101-8.
- [32] D. Liang, H. Jones, Effect of growth velocity on growth temperature of the Al-Al₃Fe and Al-Al₆Fe eutectics, *Z Metallkd*, 1992, 83, pp.224-6.
- [33] P.J. Black, The structure of FeAl₃. I, *Acta Cryst.*, 1955, 8, pp.43-8.
- [34] P. Villars, D.L. Calvert, Pearson's handbook of crystallographic data for intermetallic phases. Materials Park, OH, ASM International, 1991.
- [35] D.V. Malakhov, D. Panahi, M. Gallerneault, On the formation of intermetallics in rapidly solidifying Al-Fe-Si alloys, *CALPHAD*, 2010, 34, pp.159-66.
- [36] C.A. Aliravci, M.O. Pegguleryuz, Calculation of phase diagrams and verification of the eutectic temperature for the solidification of metastable Al-Fe phases in DC-cast aluminium alloys, *CALPHAD*, 1998, 22, pp.147-55.
- [37] H. Wenstengen, Formation of intermetallic compounds during DC casting of a commercial Al-Fe-Si alloy, *Z Metallkd*, 1982, 73, pp.360-8.
- [38] X.-G. Chen, Growth mechanisms of intermetallic phases in DC cast AA1xxx alloys, *Light Met.*, 1998, 3, pp.1071-6.
- [39] Z. Zhang, G. Li, X.G. Chen, Identification and distribution of Fe intermetallic phases in AA5657 DC cast ingots, In: Weiland H, Rollett AD, Cassada WA, editors., 13th international conference on aluminum alloys, Pittsburgh, PA, USA, 2012. pp. 1857-63.
- [40] D. Munson, A clarification of the phases occurring in aluminum-rich Aluminum-Iron-Silicon alloys with particular reference to the ternary phase α -AlFeSi, *J. Inst. Met.*, 1967, 95, pp.217-9.
- [41] Y. Langsrud, Silicon in commercial aluminium alloys - what becomes of it during dc-casting?, *Key Eng. Mat.*, 1991, 44-45, pp.95-116.
- [42] H. Kosuge, H. Takada, Phase change of the metastable phases in Al-Fe alloys at elevated temperatures, *J. Jpn. Inst. light Met*, 1979, 29, pp.64-9.
- [43] A. Griger, V. Stefániay, A. Lendvai, T. Turmezey, Possible modification of cast structure by continuous casting technology in AlFeSi alloys Part III: Intermetallic phases, *Alum*, 1989, 10, pp.1049-56.
- [44] J. Lendvai, Zs Rajkovits, T. Ungar, I. Kovacs, Formation and reversion of precipitates in a DC cast Al-0.5%Fe alloy, *Alum*, 1986, 62, pp.443-5.
- [45] J. Lendvai, G. Honyek, Zs Rajkovits, T. Ungar, I. Kovacs, T. Turmezey, The properties of Al-Fe ingots cast at different cooling rates, *Alum*, 1986, 62, pp.363-366.

- [46] L. Murgas, Z. Homonnay, S. Nagy, A. Vértes, Investigation of phase transformation in an Al-0.58 wt% Fe alloy by Mössbauer spectroscopy, *Hyperfine Interact.*, 1988, 41, pp.595-8.
- [47] J.C. Blade, Recrystallization in hot rolling of dilute aluminium alloys, *Metal Sci.*, 1979, 13, pp.206-10.
- [48] R.A. Vandermeer, D. Juul Jensen, Recrystallization in hot vs cold deformed commercial aluminum: a microstructure path comparison, *Acta Mater.*, 2003, 51, pp.3005-18.
- [49] H. McQueen, J. Hockett, Microstructures of aluminum compressed at various rates and temperatures, *Metall. Trans.*, 1970, 1, pp.2997-3004.
- [50] H.Z. Li, H.J. Wang, X.P. Liang, H.T. Liu, Y. Liu, X.M. Zhang, Hot deformation and processing map of 2519A aluminum alloy, *Mater. Sci. Eng. A*, 2011, 528, pp.1548-52.
- [51] H.R. Rezaei Ashtiani, M.H. Parsa, H. Bisadi, Constitutive equations for elevated temperature flow behavior of commercial purity aluminum, *Mater. Sci. Eng. A*, 2012, 545, pp.61-7.
- [52] Q. Zhao, M. Slagvold, B. Holmedal, Comparison of the influence of Si and Fe in 99.999% purity aluminum and in commercial-purity aluminum, *Scripta Mater.*, 2012, 67, pp.217-20.
- [53] H.J. McQueen, P. Sakaris, Influence of stress multiplier in SINH equation on constitutive constants for Al alloys with Mg and dispersoids In: L. Arnberg, E. Nes, O. Lohne, N. Ryum, editors., *Aluminum alloys: Their Physical and Mechanical Properties - Proceedings ICAA3. Trondheim, Norway* pp. 179-84.
- [54] T. Furu, R. Røed, E. Nes, Substructure evolution during different hot deformation processes of commercial non-heat treatable aluminium alloys, *Mater. Sci. Eng. A*, 1996, 214, pp.122-32.
- [55] A. Thompson, Substructure strengthening mechanisms, *Metall. Mat. Trans. A*, 1977, 8, pp.833-42.
- [56] J.C. Glez, J.H. Driver, Substructure development in hot plane strain compressed Al-1%Mn crystals, *Acta Mater.*, 2003, 51, pp.2989-3003.
- [57] H.J. McQueen, The production and utility of recovered dislocation substructures, *Metall. Mat. Trans. A*, 1977, 8, pp.807-24.
- [58] H.J. McQueen, J.J. Jonas, Role of the dynamic and static softening mechanisms in multistage hot working, *J. Appl. Metalworking*, 1985, 3, pp.410-20.
- [59] H.J. McQueen, W.A. Wong, J.J. Jonas, Deformation of aluminium at high temperatures and strain rates, *Can. J. Phys.*, 1967, 45, pp.1225-34.
- [60] J.J. Jonas, D.R. Axelrad, J.L. Uvira, On substructure strengthening and the high temperature deformation of cubic metals, *Trans. Japan. Inst. Met.*, 1968, 9, pp.257-67.

- [61] G. Avramovic-Cingara, D.D. Perovic, H.J. Mcqueen, Hot deformation mechanisms of a solution-treated Al-Li-Cu-Mg-Zr alloy, *Metall. Mat. Trans. A*, 1996, 27, pp.3478-90.
- [62] N.D. Ryan, H.J. Mcqueen, Flow stress, dynamic restoration, strain hardening and ductility in hot working of 316 steel, *J. Mat. Process. Tech.*, 1990, 21, pp.177-99.
- [63] Y. Totik, M. Gavali, The effect of homogenization treatment on the hot workability between the surface and the center of AA 2014 ingots, *Mater. Charact.*, 2002, 49, pp.261-8.
- [64] Y.V.R.K. Prasad, K.P. Rao, Effect of homogenization on the hot deformation behavior of cast AZ31 magnesium alloy, *Mater. Des.*, 2009, 30, pp.3723-30.
- [65] J. Zhang, B. Chen, Z. Baoxiang, Effect of initial microstructure on the hot compression deformation behavior of a 2219 aluminum alloy, *Mater. Des.*, 2012, 34, pp.15-21.
- [66] Ø. Ryen, B. Holmedal, O. Nijs, E. Nes, E. Sjölander, H.-E. Ekström, Strengthening mechanisms in solid solution aluminum alloys, *Metall. Mat. Trans. A*, 2006, 37, pp.1999-2006.
- [67] Q. Du, W.J. Poole, M.A. Wells, N.C. Parson, Microstructure evolution during homogenization of Al-Mn-Fe-Si alloys: Modeling and experimental results, *Acta Mater.*, 2013, 61, pp.4961-73.
- [68] H. Zhang, E.V. Konopleva, H.J. Mcqueen, Effects of Mn dispersoid on hot working of Al-1Mn, *Mater. Sci. Eng. A*, 2001, 319-321, pp.711-5.
- [69] O.D. Sherby, O.A. Ruano, Rate-controlling processes in creep of subgrain containing aluminum materials, *Mater. Sci. Eng. A*, 2005, 410-411, pp.8-11.
- [70] M.M.R. Jaradeh, T. Carlberg, Solidification Studies of 3003 Aluminium Alloys with Cu and Zr Additions, *J. Mater. Sci. Tech.*, 2011, 27, pp.615-27.
- [71] R. Benedictus, S.D. Meijers, A.J.W. And, J.H.W.D. Wit, Influence of alloying additions on corrosion behavior of aluminum brazing sheet, In: Sato T, editor., 6th International Conference on Aluminum Alloys, ICAA-6. Japan: The Japan Institute of Light Metals; 1998. pp. 1577-82.
- [72] J. Luo, M. Li, X. Li, Y. Shi, Constitutive model for high temperature deformation of titanium alloys using internal state variables, *Mech. Mater.*, 2010, 42, pp.157-65.
- [73] F.J. Zerilli, R.W. Armstrong, Dislocation-mechanics-based constitutive relations for material dynamics calculations, *J. Appl. Phys.*, 1987, 61, pp.1816-25.
- [74] G.Z. Voyiadjis, A.H. Almasri, A physically based constitutive model for fcc metals with applications to dynamic hardness, *Mech. Mater.*, 2008, 40, pp.549-63.
- [75] Y.C. Lin, Q.-F. Li, Y.-C. Xia, L.-T. Li, A phenomenological constitutive model for high temperature flow stress prediction of Al-Cu-Mg alloy, *Mater. Sci. Eng. A*, 2012, 534, pp.654-62.

- [76] S.B. Davenport, N.J. Silk, C.N. Sparks, C.M. Sellars, Development of constitutive equations for modelling of hot rolling, *Mater. Sci. Technol.*, 2000, 16, pp.539-46.
- [77] G.R. Johnson, W.H. Cook, A constitutive model and data for metals subjected to large strains, high strain rates and high temperatures, *Proceedings of the 7th International Symposium on Ballistics*. Netherlands: Hague; 1983. pp. 541-3.
- [78] N. Haghdadi, A. Zarei-Hanzaki, A.R. Khalesian, H.R. Abedi, Artificial neural network modeling to predict the hot deformation behavior of an A356 aluminum alloy, *Mater. Des.*, 2013, 49, pp.386-91.
- [79] L.X. Kong, P.D. Hodgson, D.C. Collinson, Modelling the effect of carbon content on hot strength of steels using a modified artificial neural network, *ISIJ International*, 1998, 38, pp.1121-9.
- [80] Z. Lu, Q. Pan, X. Liu, Y. Qin, Y. He, S. Cao, Artificial neural network prediction to the hot compressive deformation behavior of Al–Cu–Mg–Ag heat-resistant aluminum alloy, *Mech. Res. Commun.*, 2011, 38, pp.192-7.
- [81] N.S. Reddy, Y.H. Lee, C.H. Park, C.S. Lee, Prediction of flow stress in Ti–6Al–4V alloy with an equiaxed $\alpha + \beta$ microstructure by artificial neural networks, *Mater. Sci. Eng. A*, 2008, 492, pp.276-82.
- [82] Y.C. Lin, X.-M. Chen, A critical review of experimental results and constitutive descriptions for metals and alloys in hot working, *Mater. Des.*, 2011, 32, pp.1733-59.
- [83] M. Sumantra, P.V. Sivaprasad, S. Venugopal, K.P.N. Murthy, Constitutive flow behaviour of austenitic stainless steels under hot deformation: artificial neural network modelling to understand, evaluate and predict, *Model. Simul. Mater. Sci. Eng.*, 2006, 14, pp.1053-70.
- [84] S. Mandal, P.V. Sivaprasad, S. Venugopal, K.P.N. Murthy, Artificial neural network modeling to evaluate and predict the deformation behavior of stainless steel type AISI 304L during hot torsion, *Appl. Soft Comput.*, 2009, 9, pp.237-44.
- [85] Y.C. Lin, J. Zhang, J. Zhong, Application of neural networks to predict the elevated temperature flow behavior of a low alloy steel, *Comput. Mater. Sci.*, 2008, 43, pp.752-8.
- [86] S. Toros, F. Ozturk, Flow curve prediction of Al–Mg alloys under warm forming conditions at various strain rates by ANN, *Appl. Soft Comput.*, 2011, 11, pp.1891-8.
- [87] Y.J. Qin, Q.L. Pan, Y.B. He, W.B. Li, X.Y. Liu, X. Fan, Artificial Neural Network Modeling to Evaluate and Predict the Deformation Behavior of ZK60 Magnesium Alloy During Hot Compression, *Mater. Manuf. Process.*, 2010, 25, pp.539-45.
- [88] R. Kapoor, D. Pal, J.K. Chakravarty, Use of artificial neural networks to predict the deformation behavior of Zr–2.5Nb–0.5Cu, *J. Mater. Process. Tech.*, 2005, 169, pp.199-205.
- [89] Y. Sun, W. Zeng, X. Ma, B. Xu, X. Liang, J. Zhang, A hybrid approach for processing parameters optimization of Ti-22Al-25Nb alloy during hot deformation using artificial neural network and genetic algorithm, *Intermetallics*, 2011, 19, pp.1014-9.

- [90] Y. Sun, W.D. Zeng, Y.Q. Zhao, Y.L. Qi, X. Ma, Y.F. Han, Development of constitutive relationship model of Ti600 alloy using artificial neural network, *Comput. Mater. Sci.*, 2010, 48, pp.686-91.
- [91] I.S. Jalham, Modeling capability of the artificial neural network (ANN) to predict the effect of the hot deformation parameters on the strength of Al-base metal matrix composites, *Compos. Sci. Technol.*, 2003, 63, pp.63-7.
- [92] S. Banerjee, P.S. Robi, A. Srinivasan, L. Praveen Kumar, High temperature deformation behavior of Al–Cu–Mg alloys micro-alloyed with Sn, *Mater. Sci. Eng. A*, 2010, 527, pp.2498-503.
- [93] S.B. Brown, K.H. Kim, L. Anand, An internal variable constitutive model for hot working of metals, *Int. J. Plast.*, 1989, 5, pp.95-130.
- [94] F.A. Slooff, J. Zhou, J. Duszczyk, L. Katgerman, Constitutive analysis of wrought magnesium alloy Mg–Al₄–Zn₁, *Scripta Mater.*, 2007, 57, pp.759-62.
- [95] Y.C. Lin, Y.-C. Xia, X.-M. Chen, M.-S. Chen, Constitutive descriptions for hot compressed 2124-T851 aluminum alloy over a wide range of temperature and strain rate, *Comput. Mater. Sci.*, 2010, 50, pp.227-33.
- [96] H. Mirzadeh, A. Najafizadeh, M. Moazeny, Flow Curve Analysis of 17-4 PH Stainless Steel under Hot Compression Test, *Metall. Mater. Trans. A*, 2009, 40, pp.2950-8.
- [97] Y.-C. Lin, M.-S. Chen, J. Zhang, Modeling of flow stress of 42CrMo steel under hot compression, *Mater. Sci. Eng. A*, 2009, 499, pp.88-92.
- [98] S. Mandal, V. Rakesh, P.V. Sivaprasad, S. Venugopal, K.V. Kasiviswanathan, Constitutive equations to predict high temperature flow stress in a Ti-modified austenitic stainless steel, *Mater. Sci. Eng. A*, 2009, 500, pp.114-21.
- [99] Z.Y. Chen, S.Q. Xu, X.H. Dong, Deformation behavior of AA6063 aluminium alloy after removing friction effect under hot working conditions, *Acta Metall. Sin.*, 2008, 21, pp.451-8.
- [100] W. Li, H. Li, Z. Wang, Z. Zheng, Constitutive equations for high temperature flow stress prediction of Al–14Cu–7Ce alloy, *Mater. Sci. Eng. A*, 2011, 528, pp.4098-103.
- [101] C.M. Sellars, W.J. McTegart, La relation entre la résistance et la structure dans la déformation à chaud, *Mem. Sci. Rev. Met.*, 1966, 63, pp.731-46.
- [102] A. Marandi, A. Zarei-Hanzaki, N. Haghdadi, M. Eskandari, The prediction of hot deformation behavior in Fe–21Mn–2.5Si–1.5Al transformation-twinning induced plasticity steel, *Mater. Sci. Eng. A*, 2012, 554, pp.72-8.
- [103] A.R. Khataee, M.B. Kasiri, *Computer Science, Technology and Applications: Artificial Neural Network Modeling of Water and Wastewater Treatment Processes*. New York, Nova Science Publishers, Inc., 2011.

CHAPTER 3

EFFECT OF HOMOGENIZATION TREATMENT AND SILICON CONTENT ON THE MICROSTRUCTURE AND HOT WORKABILITY OF DILUTE AL-FE-SI ALLOYS

CHAPTER 3

**EFFECT OF HOMOGENIZATION TREATMENT AND SILICON
CONTENT ON THE MICROSTRUCTURE AND HOT WORKABILITY
OF DILUTE AL-FE-SI ALLOYS¹**

Abstract

The effect of the homogenization treatment on the microstructure and hot workability of two dilute Al-Fe-Si alloys was investigated using optical microscopy, SEM, EBSD, electrical conductivity measurements and hot compression testing. Homogenization promoted the phase transformation from the metastable Al_mFe or $\alpha-AlFeSi$ phase to the Al_3Fe equilibrium phase and induced a significant change in solute levels in the solid solution. The Al_mFe dissolved and transformed completely at 550°C in both alloys. The $\alpha-AlFeSi$ was transformed at 590°C in the low Si alloy (Al-0.3Fe-0.1Si), whereas it began to decompose and transform to Al_3Fe at 630°C in the high Si alloy (Al-0.3Fe-0.25Si). The flow stress behavior of dilute Al-Fe-Si alloys was primarily controlled by the amount of Fe and Si in the solid solution. Homogenization at 550°C significantly reduced the solid solution levels due to the elimination of the supersaturation originating from the cast ingot and produced the lowest flow stress under all of the deformation conditions studied. An

¹ Published at Mater. Sci. Eng. A, 2014, 619, pp. 180-189.

increase in the homogenization temperature from 550 to 630°C increased the flow stress by 10 to 23% and 15 to 45% for the low Si alloy and the high Si alloy, respectively, over the range of deformation conditions examined. An increase in the silicon level from 0.10 to 0.25% raised the overall flow stresses by 4-11% due to increased solute levels for given homogenization conditions.

3.1 Introduction

The 1xxx series of aluminum alloys are strain hardenable and offer excellent formability, corrosion resistance, and thermal and electrical conductivity. Typical applications include foil and strips for packaging, heat exchanger tubing and finstock, coaxial cable sheathing and electrical conductors [1, 2]. In general, these products are hot deformed by extrusion or rolling from direct chill (DC) cast billets or ingots. The demand for high productivity during processing leads to the requirement for an increase in hot workability to provide low flow stress with desirable final mechanical properties. Therefore, many variants of the 1xxx series alloys are in commercial use today, balancing mechanical and physical properties along with processability. One example is the use of 1xxx series alloys in the form of hot extruded tubing for heat transfer and sheathing applications. To reduce production costs, high extrusion speeds, which are primarily controlled by the flow stress during hot deformation, are desirable. The hot working characteristics of the cast billet or ingot have a significant influence on the hot forming process, which in turn are determined by its microstructure and hot deformation regimes [3, 4]. Commercially, DC cast billets or ingots are typically homogenized prior to extrusion or rolling to improve hot workability and mechanical properties [5, 6]. In many cases, the hot

workability can be optimized by proper selection of the homogenization method applied to the cast materials [7]. Prasad et al.[6] reported that a suitable homogenization treatment, which dissolved the intermetallic particles present at the grain boundaries, improves hot workability of as-cast AZ31 alloy by reducing the intercrystalline cracking and flow instability regimes. Totik et al.[7] showed that homogenization at 510 °C significantly improved the hot workability of AA 2014 alloy and resulted in the uniform workability of the tested ingots. Zhang et al.[3] studied the influence of the initial microstructure on the hot workability of a AA 2219 aluminum alloy and found that the as-aged microstructure produced the lowest hot deformation resistance and the as-solutionized microstructure showed the highest deformation resistance under the same deformation conditions. Liu et al.[8] investigated the effect of cooling rate after homogenization on the elevated temperature flow behavior of AA 7050 aluminum alloy and found that furnace-cooled alloy exhibited higher hot workability than water-quenched alloy. However, there is very limited information in the literature on the effectiveness of the homogenization treatment in 1xxx alloy production.

The 1xxx series alloys contain at least 99.0% aluminum with iron and silicon as the main alloying elements or impurities (all alloy compositions are given in wt% unless otherwise indicated). Because the solid solubility of iron in aluminum is very low (i.e., max. 0.05% at 650°C), most of the iron combines with both aluminum and silicon to form secondary intermetallic phases [9, 10]. The equilibrium intermetallic Al_3Fe phase can form at slow solidification rates. However, depending on the alloy composition, cooling rate and presence of trace elements, a wide range of intermediate intermetallic phases, such as

Al_mFe , Al_9Fe , Al_6Fe , Al_xFe and $\alpha\text{-AlFeSi}$ ($\text{Al}_8\text{Fe}_2\text{Si}$), can form and are considered metastable Fe-rich phases in the literature [9-11]. The metallurgical performance of 1xxx series alloys during hot deformation can be influenced by secondary intermetallic phases in terms of their type, size and distribution. Although there are abundant studies on the formation of iron-rich intermetallic phases during solidification of 1xxx series aluminum alloys [12], studies of their evolution during the homogenization treatment are limited. Kosuge et al. [13] and Griger et al. [14] reported a solid-state phase transformation from Al_mFe , Al_6Fe and $\alpha\text{-AlFeSi}$ to Al_3Fe in dilute Al-Fe-Si alloys. Li et al. [15] also observed the phase transformation from $\text{Al}_m(\text{FeMn})$ to $\text{Al}_3(\text{FeMn})$ in AA5182 after homogenization at 520°C.

In the current study, the microstructural evolution of two typical dilute Al-Fe-Si alloys during homogenization was investigated using optical and electron microscopy as well as electric conductivity measurements. The effect of the homogenization parameters on the intermetallic phase transformation and solid solution levels was studied. The hot deformation behavior under different homogenization conditions was evaluated using the uniaxial hot compression test at various deformation temperatures and strain rates.

3.2 Experimental Procedure

Two dilute Al-Fe-Si alloys with chemical compositions shown in Table 3.1 were selected for investigation. Both alloys were prepared from commercially pure aluminum (99.7%), Al-20%Fe and Al-50%Si master alloys. For each alloy, approximately 10 kg of material was melted in an electrical resistance furnace. The melting temperature was kept at

about 750 °C. The molten metals were grain-refined by addition of 0.015% Ti in the form of an Al-5Ti-1B master alloy. The melts then cast into a rectangular permanent steel mold measuring 30×40×80 mm³. The chemical compositions of each alloy were measured using optical emission spectroscopy (OES) technique.

Table 3.1. Chemical compositions of two Al-Fe-Si alloys studied (wt%)

Alloys	Fe	Si	Cu	Mn	Cr	Ni	Zn	Ti	B	Ga	V	Fe/Si
Low Si	0.31	0.11	0.002	0.002	0.001	0.002	0.002	0.024	0.0029	0.014	0.011	2.82
High Si	0.31	0.26	0.002	0.002	0.001	0.002	0.002	0.024	0.0029	0.014	0.011	1.19

Cast ingots were homogenized at 550, 590 and 630°C for various soaking times (2, 6 and 12 h) followed by water quenching. All homogenization treatments were conducted in an air circulating electrical furnace. As-cast and homogenized samples were taken from the same ingot position for metallographic examination to eliminate the influence of the cooling rate.

The microstructures of the as-cast and homogenized samples were examined using optical microscopy (OM) and scanning electron microscopy (SEM, JEOL-6480LV) equipped with an electron backscatter diffraction (EBSD) system. Because iron-rich intermetallic phases have different morphologies [16, 17] and the stoichiometry of iron-rich phases are not always fixed, the EBSD technique was employed to provide unambiguous characterization of the iron-rich phases. The crystallographic data for all of the binary Al-Fe and ternary Al-Fe-Si compounds listed in the Pearson's Handbook [18] were entered

into a customized Channel 5 software database for phase identification. A total of 12 fields with dimensions of 150 μm x 150 μm were observed in each sample. All of the Fe-rich intermetallic particles in each field were identified by the EBSD analysis and more than 100 particles in each sample were characterized. After identifying all of the intermetallic particles appearing in each field, the volume fraction of each phase was quantified using the CLEMEX image analyzing system.

The electrical conductivity was measured using an AC electrical conductivity instrument (SIGMASCOPE SMP 10) on the polished rectangular ingot blocks measuring 50x35x25 mm^3 . This machine measures the electrical conductivity using the eddy current method. All tests were conducted at frequency of 60 kHz. In order to consider the influence of temperature on the electrical conductivity of the samples the temperature of the specimens was directly measured by one sensor while other sensor measured the electrical conductivity. SIGMASCOPE SMP 10 gives electrical conductivity of different metals and alloys in comparison with international annealed copper standard (%IACS). IACS is 100% for annealed copper standard. For each condition, six electrical conductivity measurements were performed to provide an average value.

Cylindrical specimens of 10 mm diameter and 15 mm in height were machined for hot compression testing. The uniaxial hot compression tests were conducted using a Gleeble 3800 thermo-mechanical testing unit at strain rates of 0.01 and 1 s^{-1} and deformation temperatures of 400 and 500°C. During the tests on the Gleeble 3800 unit, specimens were heated at a rate of 2 °C/s and maintained for 120 s at the desired temperature to ensure a

homogeneous temperature distribution. The specimens were deformed to a total true strain of 0.8 and then immediately water-quenched to room temperature.

3.3 Results and Discussion

3.3.1 As-cast and homogenized microstructures

Figure 3.1 shows the optical microstructures of two Al-Fe-Si alloys in the as-cast condition, which consists of α -Al dendrites (matrix) and different Fe-rich intermetallic phases distributed along the aluminum dendrite boundaries. The mean aluminum grain sizes were 110 and 120 μm for the low Si alloy (Al-0.3Fe-0.1Si) and high Si alloy (Al-0.3Fe-0.25Si), respectively. In general, four different types of Fe-rich intermetallics including equilibrium Al_3Fe and metastable Al_mFe , α -AlFeSi and Al_6Fe phases were observed in the cast microstructure. In the low Si alloy, the dominant phases were the feather-like Al_mFe and acicular Al_3Fe (Fig. 3.1a), and in the high Si alloy, the major phases were Chinese script α -AlFeSi and acicular Al_3Fe (Fig. 3.1b).

During homogenization at the temperature range studied (550 to 630 $^\circ\text{C}$), the metastable Al_mFe and α -AlFeSi phases became unstable and transformed to the equilibrium Al_3Fe phase. Figure 3.2 shows an example of the microstructure after homogenization at 630 $^\circ\text{C}$ for 12 h for both alloys. The feather-like Al_mFe was completely changed to acicular and plate-like Al_3Fe in the low Si alloy (Fig. 3.2a), while most of the Chinese script α -AlFeSi was transformed to plate-like Al_3Fe and only a few spheroidized α -AlFeSi remained in the high Si alloy (Fig. 3.2b).

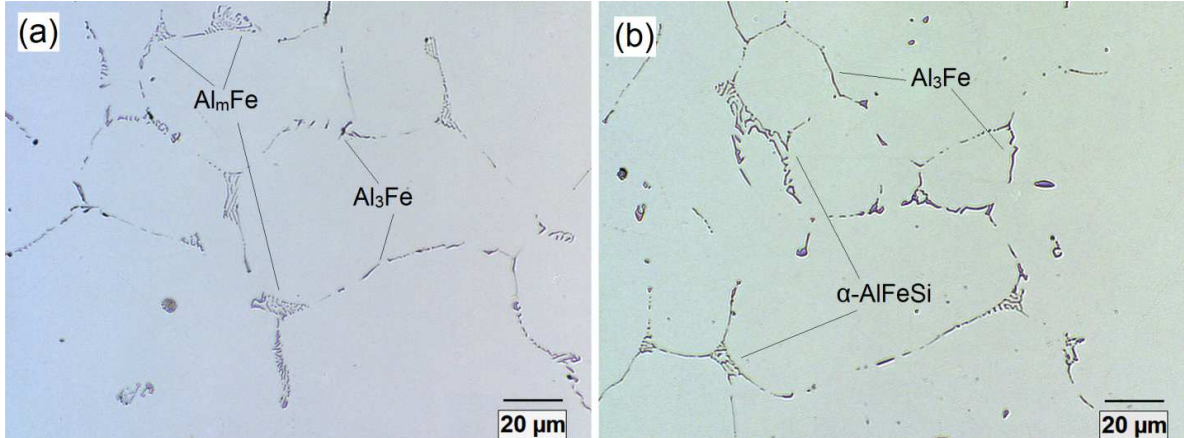


Fig. 3.1. As-cast microstructures: (a) low Si alloy (Al-0.3Fe-0.1Si) and (b) high Si alloy (Al-0.3Fe-0.25Si).

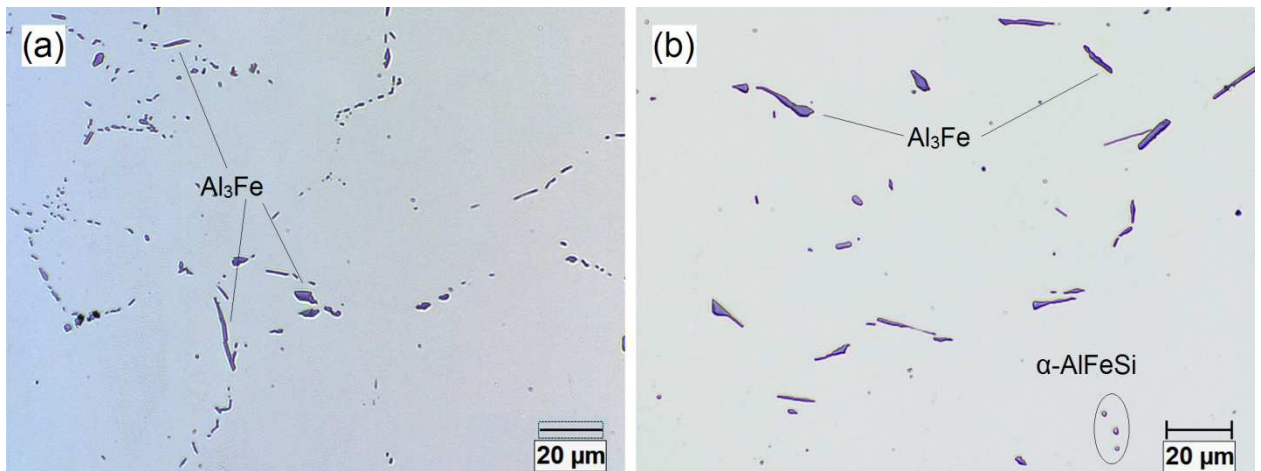


Fig. 3.2. Microstructures after homogenization at 630 °C for 12 h: (a) low Si alloy (Al-0.3Fe-0.1Si) and (b) high Si alloy (Al-0.3Fe-0.25Si).

3.3.2. Evolution of iron-rich intermetallic phases during homogenization

To better quantify their evolution during heat treatment, all of the Fe-rich intermetallic particles were first identified by EBSD and then the volume fraction of each phase was

quantified by image analysis [19, 20]. Figure 3.3 shows typical morphologies and their EBSD solutions for the four different intermetallics observed in the two alloys in the as-cast and homogenized conditions. In the EBSD analysis, the mean angular deviation (MAD) between the experimental and simulated patterns represents the accuracy of the solution. A smaller value indicates a closer match between the experimental and simulated results. Typically, a MAD value smaller than 0.7 is considered to be critical for an accurate solution [21]. The MAD values obtained for Al_mFe , Al_6Fe , Al_3Fe and $\alpha\text{-AlFeSi}$ phases presented in figure 3.3, were approximately 0.2, 0.14, 0.18 and 0.23, respectively, which are much lower than 0.7 and confirm the reliable and accurate identification of all four phases.

The quantitative results for phase evolution as a function of homogenization temperature are shown in Figure 4. In the low Si alloy (Fig. 3.4a), the as-cast microstructure was dominated by both Al_mFe and Al_3Fe with a minor amount of $\alpha\text{-AlFeSi}$. After homogenization at 550 °C for 6 h, Al_mFe decomposed and completely transformed to Al_3Fe while the $\alpha\text{-AlFeSi}$ remained unchanged. After increasing the temperature to 590 °C, $\alpha\text{-AlFeSi}$ dissolved and transformed to Al_3Fe . Therefore, at higher homogenization temperatures (590 to 630 °C), Al_3Fe is the only intermetallic phase in the microstructure.

For the high Si alloy (Fig. 3.4b), the as-cast microstructure consisted of a major phase of $\alpha\text{-AlFeSi}$ and two minor phases consisting of Al_3Fe and Al_mFe . During homogenization at 550 °C for 6 h, all of the Al_mFe was converted to Al_3Fe but the $\alpha\text{-AlFeSi}$ remained stable. The major $\alpha\text{-AlFeSi}$ phase only began to decompose at 630°C. After 6 h, most of the

α -AlFeSi particles transformed to Al_3Fe . Therefore, the major α -AlFeSi co-existed with Al_3Fe at 550 and 590 °C, and Al_3Fe become the predominant phase at 630 °C.

In both alloys, Al_6Fe was present as trace amounts of isolated particles (i.e., less than 3% of the constituent particles) in the as-cast microstructure. As reported by Griger et al. [14] and Tezuka et al. [22], the use of Al-Ti-B as a grain refiner can promote the formation of Al_mFe over Al_6Fe . During homogenization, the Al_6Fe phase was stable at 550 °C and disappeared after homogenization at 590 °C in both alloys.

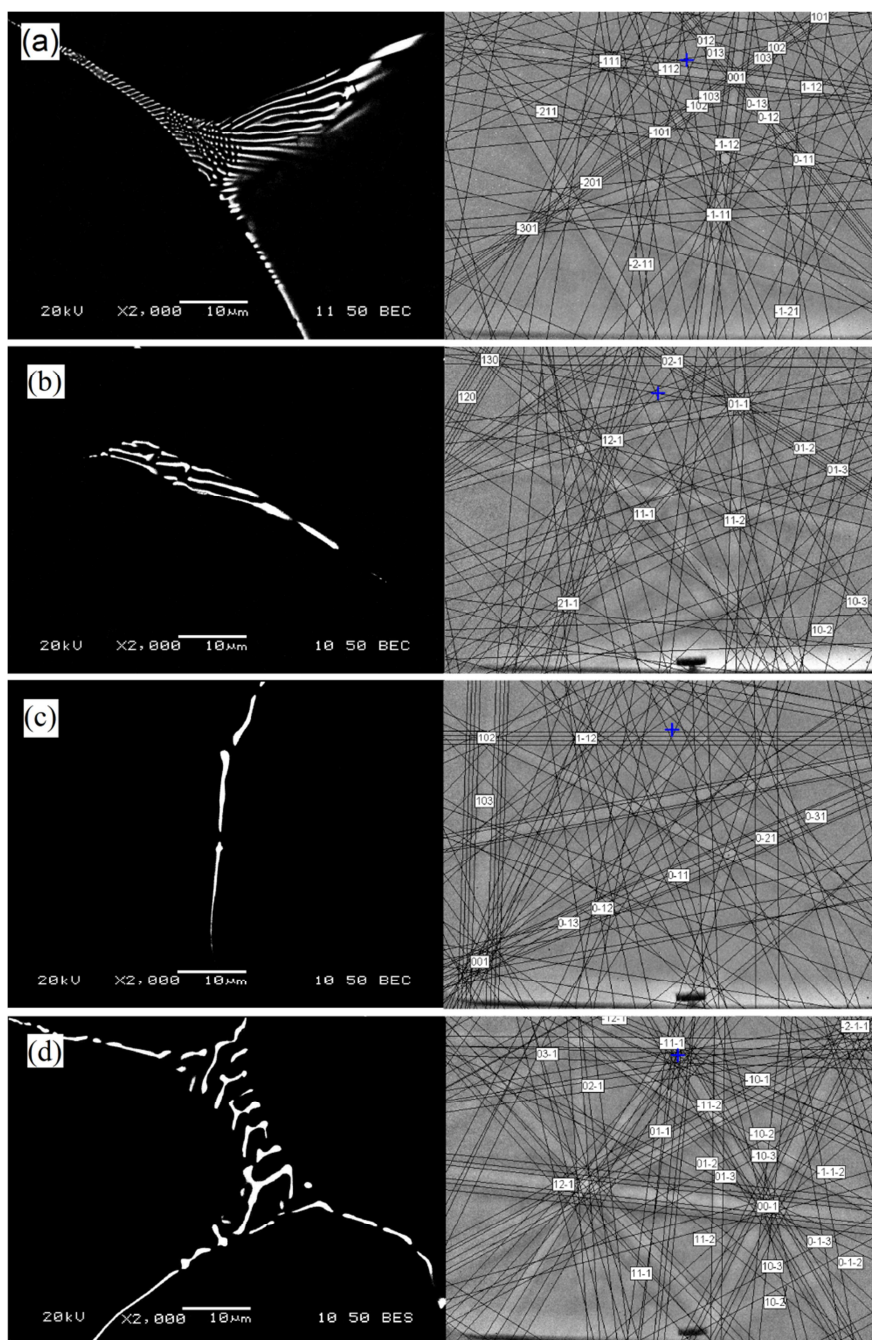


Fig. 3.3. Backscattered electron images and corresponding EBSD solutions for different type of Fe-rich particles: (a) Al_mFe (as-cast Al-0.3Fe-0.1Si), (b) Al_6Fe (as-cast Al-0.3Fe-0.1Si), (c) Al_3Fe (Al-0.3Fe-0.25Si homogenized at 630 °C for 12 h) and (d) $\alpha\text{-AlFeSi}$ (as-cast Al-0.3Fe-0.25Si).

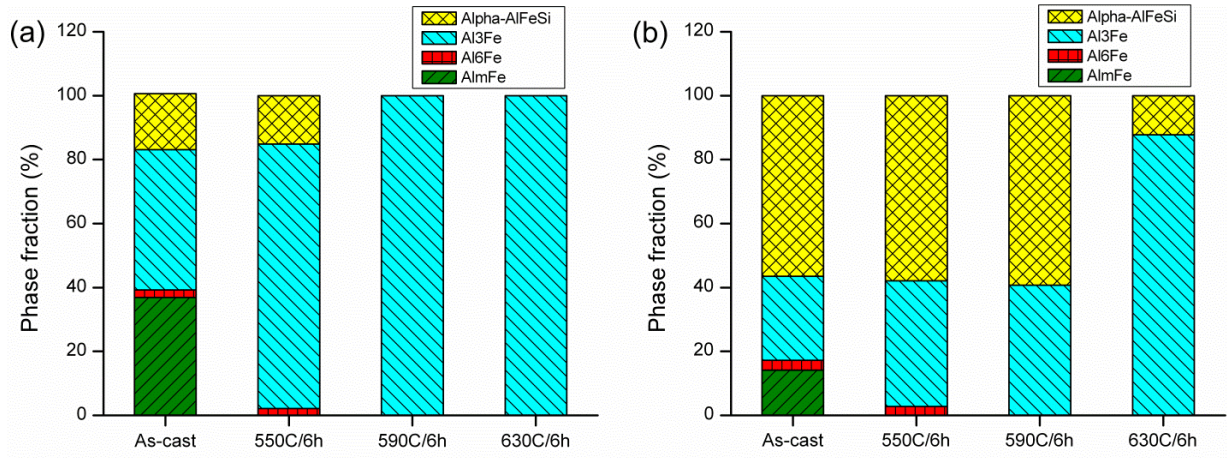


Fig. 3.4. Evolution of the phase volume fractions of Fe-rich intermetallics for the as-cast and homogenized conditions: (a) low Si alloy and (b) high Si alloy.

It should be mentioned that the total amount of intermetallic phases measured in the as-cast condition were approximately 1.3 and 1.5 vol.% for the low Si and high Si alloys, respectively. During homogenization, the total volume fraction of intermetallics may slightly change due to the phase transformation. However, these small changes tend to be within the accuracy range of the image analysis measurement.

3.3.2.1. Solid-state transformation from Al_mFe to Al_3Fe

Figure 3.5 shows the solid-state transformation from Al_mFe to Al_3Fe in detail at 550°C for the low Si alloy, starting with the cast microstructure in Fig. 3.5a where the Al_mFe phase formed during solidification. During homogenization at 550°C for 2 h (Fig. 3.5b and c), Al_mFe first spheroidized and then dissolved in the aluminum matrix. Simultaneously, plate-like Al_3Fe particles precipitated either in the aluminum matrix close to the original Al_mFe phase or on the pre-existing Al_3Fe phase formed during solidification. It is apparent

that the solid-state transformation from Al_mFe to Al_3Fe proceeds via a dissolution-reprecipitation mechanism where iron is required to diffuse from the dissolving Al_mFe to the precipitating Al_3Fe particles. Therefore, the controlling factor for the phase transformation is the diffusion of iron between the two species. By increasing the homogenization time to 6 h (Fig 3.5d), all of the Al_mFe transformed to Al_3Fe , which continued to coarsen into large plate-like particles. Homogenization at a higher temperature or for a longer time, as shown in Figure 3.2 (a), promoted the formation of coarse block-shaped or plate-like Al_3Fe , which most likely result from phase ripening and coalescence.

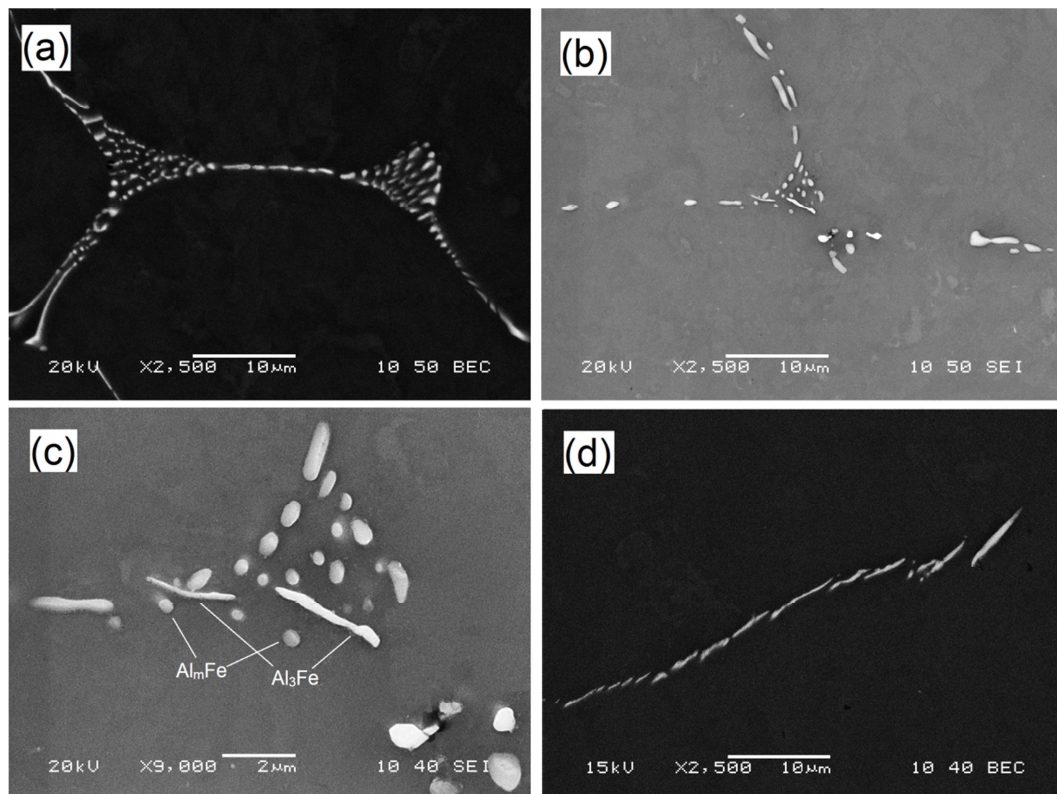


Fig. 3.5. Transformation from Al_mFe to Al_3Fe in the low Si alloy: (a) As-cast, (b) 550 °C for 2 h, (c) 550 °C for 2 h at high magnification and (d) 550 °C for 6 h.

3.3.2.2. Solid-state transformation from α -AlFeSi to Al_3Fe

Figure 3.6 illustrates the microstructural evolution during homogenization at 630°C and shows the solid-state transformation from α -AlFeSi to Al_3Fe in the high Si alloy. In the as-cast condition, the Chinese script α -AlFeSi particles were located along the aluminum dendrite boundaries (Fig. 3.6a). During homogenization at 630 °C for 2 h, α -AlFeSi first coarsened and spheroidized (Figs. 3.6b and c) and finally dissolved releasing Fe and Si atoms into the solid solution. Simultaneously, Al_3Fe precipitated either in the vicinity of the original α -AlFeSi (Fig. 3.6c) or on the pre-existing Al_3Fe particles. The α -AlFeSi to Al_3Fe transformation also proceeded via a dissolution-reprecipitation mechanism. The phase transformation rate is believed to be controlled by the growth rate of the Al_3Fe phase, which in turn is controlled by the diffusion of Fe in the aluminum matrix from the dissolving α -AlFeSi to the precipitating Al_3Fe .

After homogenization for 12 h, most of α -AlFeSi had completely transformed and Al_3Fe continued to coarsen into large plate-like particles. However, a small amount of spheroidal α -AlFeSi still remained in the microstructure (Fig. 3.6d). For the low Si alloy, all of the α -AlFeSi particles transformed to Al_3Fe at 590 °C, whereas in the high Si alloy, α -AlFeSi was stable at this temperature and only started to transform at 630°C. Due to the higher bulk silicon content, α -AlFeSi in the high Si alloy is more stable than that in the low Si alloy.

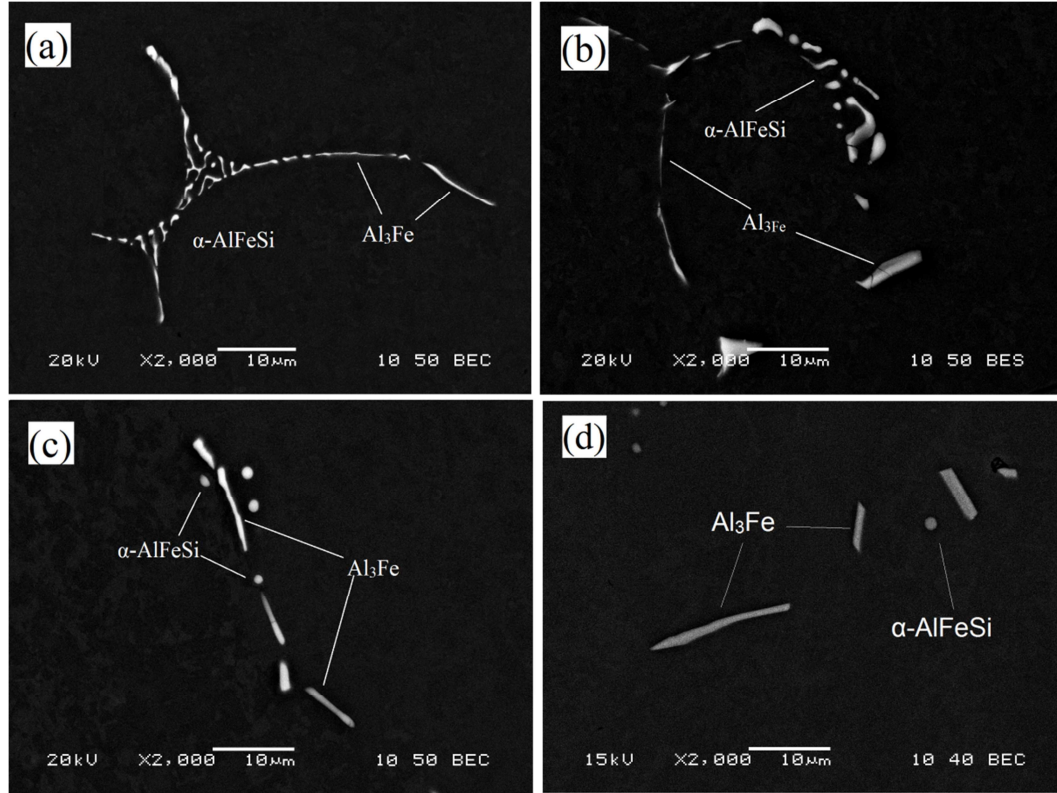


Fig. 3.6. Transformation from α -AlFeSi to Al_3Fe in the high Si alloy: (a) As-cast, (b) and (c) 630 °C for 2 h and (d) 630 °C for 12 h.

3.3.3. Solid solution levels

Solid solution levels can significantly contribute to the high temperature flow stress in dilute aluminum alloys [5, 23]. However, due to low solubility of iron in aluminum and also low amount of Si concentration in the investigated alloys it is very hard to directly measure the solute level of these elements in the aluminum matrix by EDX technique precisely. Furthermore, using XRD technique to measure the solute levels of iron and silicon based on the variation of lattice parameters is technically challenging, because it needs an advance XRD machine and also reliable standard. The increase or decrease in

electrical conductivity is widely used to follow the dissolution and precipitation of solutes in aluminum alloys [24, 25] and was used as an index of solid solution levels of Fe and Si in this study.

The impact of the homogenization treatment on the electrical conductivity of the two alloys is shown in Figure 3.7. In comparison to the low Si alloy, the high Si alloy generally exhibited lower conductivity for a given condition, indicating overall higher levels of solute in solution. During the rapid solidification in the permanent mold casting, which has a similar cooling rate range to DC cast ingots, some Fe and Si atoms are retained in the supersaturated solid solution. Homogenization at 550°C significantly increased the electrical conductivity of both alloys compared to the as-cast condition due to the elimination of supersaturation as excess Fe and Si were precipitated as intermetallics. As the homogenization temperature was increased to 630 °C, the conductivity decreased to levels similar to the as-cast condition, indicating the dissolution of Fe and Si containing constituent phases.

In the low Si alloy, the phase transformation of Al_mFe to Al_3Fe occurred at 550 °C and reached completion with increased homogenization time. However, the conductivity changed only slightly as the homogenization time increased at this temperature (Fig. 3.7a), which indicated that this type of phase transformation did not significantly affect the solid solution levels. However, by increasing the homogenization temperature from 550 to 590 °C, the transformation of $\alpha-AlFeSi$ to Al_3Fe was promoted resulting in a release of Si atoms into the solution. Therefore, the decrease in conductivity was more significant. An increase

in the temperature to 630 °C further decreased the conductivity, which corresponded to the re-dissolution of the constituent phases and further release of Fe and Si into the solution due to increased solid solubility at a higher temperature.

As shown in Fig. 3.7b, the high Si alloy only exhibited a slight decrease in electrical conductivity from 550 to 590 °C because no phase transformation occurred in this temperature range (Fig. 4b). However, a more significant drop in conductivity was observed when the temperature was increased from 590 to 630 °C because the transformation of α -AlFeSi to Al_3Fe released free Si atoms into the solution and the solid solubility increased with temperature. After soaking at 630 °C, the conductivity continued to decrease as the homogenization time increase, and after 12 h the conductivity of the high Si alloy was actually lower than that at the as-cast condition, which indicated that the solid solution levels progressively increased as the homogenization time increased.

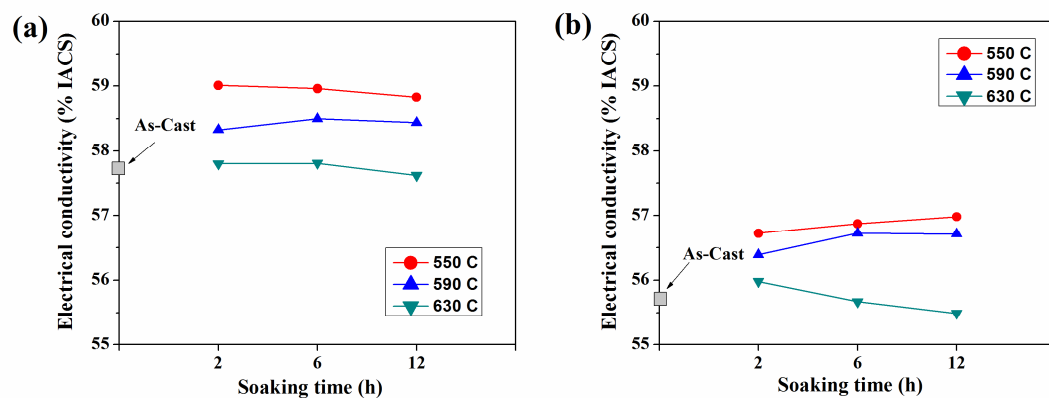


Fig. 3.7. Effect of homogenization practice on the electrical conductivity: (a) low Si alloy and (b) high Si alloy.

The results for both alloys in Fig. 3.7 indicate that the solid solution levels initially decreased during homogenization at 550 °C and then increased at higher homogenization temperatures. It is also evident that the Al_mFe to Al_3Fe phase transformation had little influence on the solid solution levels, and the phase transformation of $\alpha\text{-AlFeSi}$ to Al_3Fe significantly increased solute levels in the solution during homogenization.

3.3.4. Flow stress behavior during hot deformation

The hot workability of two dilute Al-Fe-Si alloys was assessed by a series of flow stress curves. Figures 3.8 and 3.9 show the true stress-true strain curves for both alloys as a function of homogenization temperature for a 6 h soak time compared to the as-cast starting material. For most of the test conditions, the peak flow stress was followed by a steady state region, as shown in Figures 3.8 and 3.9. However, at the highest Z condition ($\dot{\epsilon}=1 \text{ s}^{-1}$ and $T=400 \text{ °C}$), the flow stress continued to increase with increasing strain. The former case occurs when dynamic softening is in balance with work hardening while the latter phenomenon is indicative of work hardening being stronger than softening during deformation. In general, such flow stress behaviors are characteristic of hot working where dynamic recovery is the main softening mechanism [5]. For the low Si alloy (Fig. 3.8), the flow stress behavior was very similar for all four deformation conditions. The as-cast material always exhibited the highest flow stress values. Homogenization at 550 °C yielded the lowest flow stress values. The flow stress gradually increased when the homogenization temperature was increased to 590 and 630 °C. For the high Si alloy (Fig. 3.9), the highest overall value of flow stress was obtained after homogenization at 630°C followed by the

as-cast condition. The minimum values of flow stress were still obtained after homogenization at 550 °C.

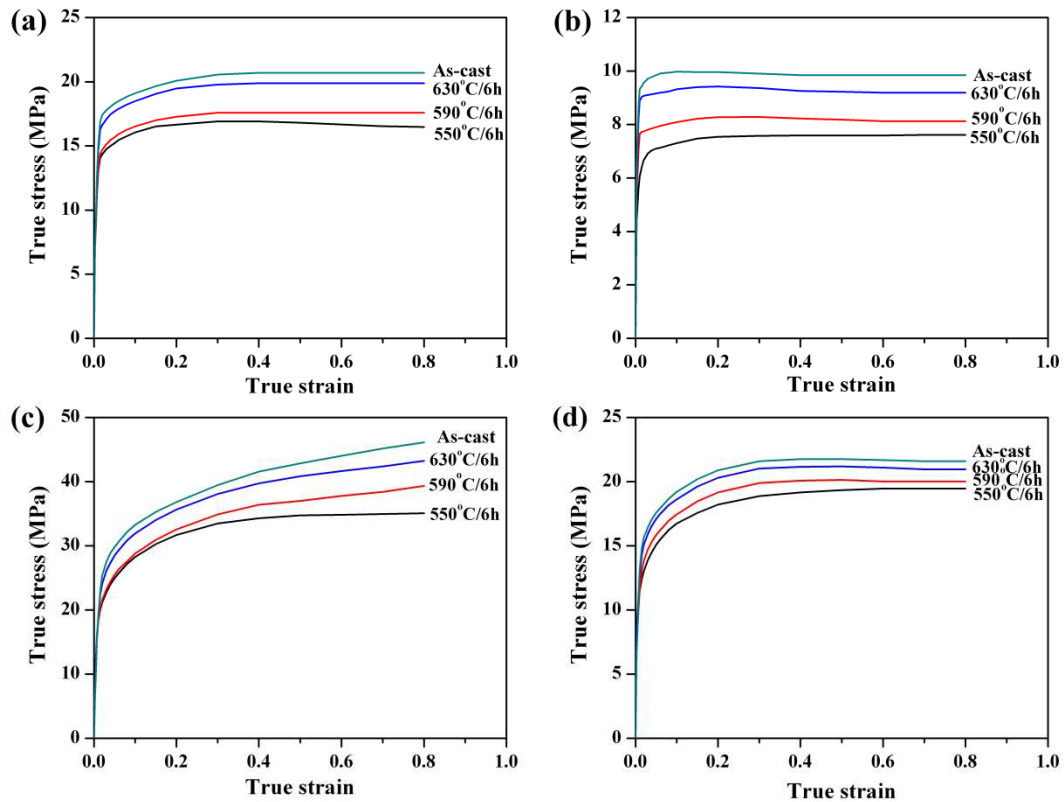


Fig. 3.8. True stress-true strain curves for different initial states of the low Si alloy under different deformation conditions: (a) $\dot{\epsilon}=0.01 \text{ s}^{-1}$, $T=400 \text{ }^{\circ}\text{C}$, (b) $\dot{\epsilon}=0.01 \text{ s}^{-1}$, $T=500 \text{ }^{\circ}\text{C}$ (c) $\dot{\epsilon}=1 \text{ s}^{-1}$, $T=400 \text{ }^{\circ}\text{C}$ and (d) $\dot{\epsilon}=1 \text{ s}^{-1}$, $T=500 \text{ }^{\circ}\text{C}$.

Typical flow stress values at a strain of 0.8 are shown in Figure 3.10 as a function of the homogenization temperature for deformation conditions where $\dot{\epsilon}=1 \text{ s}^{-1}$ and $T=400$ and 500°C . The two alloys exhibited a similar trend as a function of the homogenization temperature. Homogenization decreased the flow stress compared to the as-cast condition,

and treatment at 550°C yielded the minimum flow stress for both alloys. This result is consistent with the supersaturated state of the as-cast ingot and the maximum precipitation of the solute at 550°C. However, the flow stress increased again at higher homogenization temperatures as the solute levels increased. In general, the high Si alloy exhibited higher flow stress values (4-11%) under all deformation conditions due to the higher solute content.

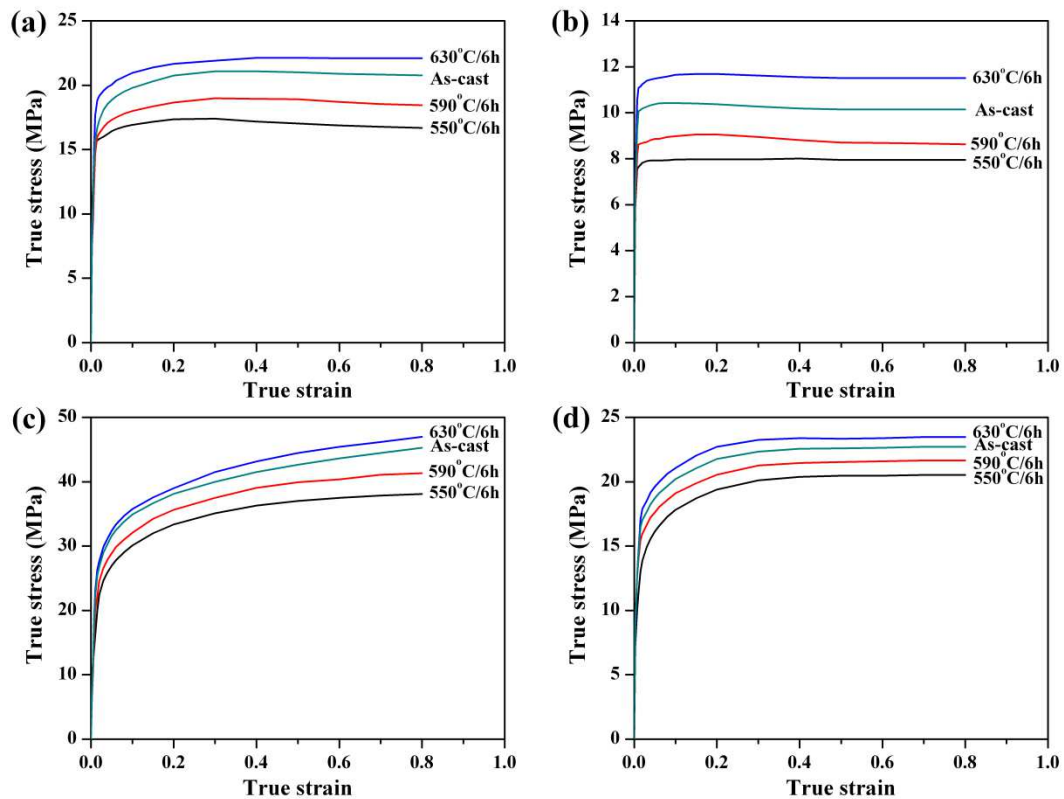


Fig. 3.9. True stress-true strain curves for different initial states of the high Si alloy under different deformation conditions: (a) $\dot{\epsilon}=0.01 \text{ s}^{-1}$, $T=400 \text{ }^{\circ}\text{C}$, (b) $\dot{\epsilon}=0.01 \text{ s}^{-1}$, $T=500 \text{ }^{\circ}\text{C}$ (c) $\dot{\epsilon}=1 \text{ s}^{-1}$, $T=400 \text{ }^{\circ}\text{C}$ and (d) $\dot{\epsilon}=1 \text{ s}^{-1}$, $T=500 \text{ }^{\circ}\text{C}$.

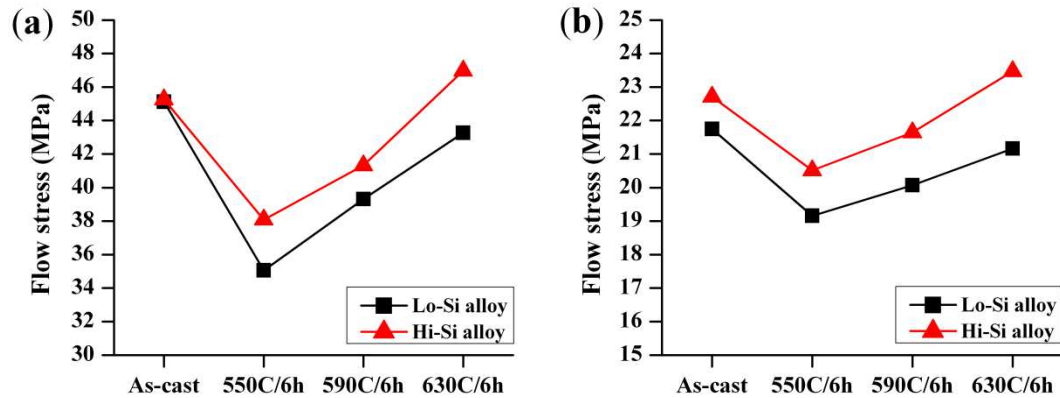


Fig. 3.10. Effect of homogenization treatment on the flow stress (a) $\dot{\epsilon}: 1 \text{ s}^{-1}$, $T: 400^\circ\text{C}$ and (b) $\dot{\epsilon}: 1 \text{ s}^{-1}$, $T: 500^\circ\text{C}$ at a strain of 0.8.

In the low Si alloy, an increase in the soak temperature from 550 to 630°C produced a 10 to 23% increase in the flow stress over the range of deformation conditions due to increased Fe and Si levels in the solid solution. For the same range of conditions, the flow stress of the high Si alloy increased by 15 to 45%. This larger increase in the flow stress was associated with the higher proportion of $\alpha\text{-AlFeSi}$, which promoted the release of more Si solute during the transformation to Al_3Fe .

3.3.5. Discussion

The Fe and Si present in the 1xxx DC cast ingots as deliberate alloy additions or impurities are generally present in two forms: (1) constituent particles that are Fe-rich intermetallics distributed along aluminum cell and grain boundaries and (2) solute elements that are in the aluminum solid solution. Both constituent particles and solute elements can have significant impacts on the hot workability of aluminum alloys [5]. Homogenization of

DC cast ingots prior to extrusion or rolling often results in significant changes in the type, size and distribution of constituent particles as well as the solute levels in the aluminum matrix, which in turn, can alter the hot workability of a given alloy.

3.3.5.1. Effect of constituent particles

Al-Fe and Al-Fe-Si intermetallic (constituent) particles in dilute Al-Fe-Si alloys were originally eutectic secondary phases that solidified around aluminum cells and grains. In general, when intermetallic particles are relatively fine ($<1 \mu\text{m}$) and uniformly distributed in the matrix, they can effectively pin dislocations, stabilize subgrains and retard dynamic recovery and recrystallization, leading to a large increase in the flow stress during the hot deformation process[5]. In the current study, the size of all of the intermetallic particles in the as-cast and homogenized conditions were quite large (i.e., from one to tens of μm , as shown in Figs. 3.1 and 3.2), and the total volume fractions of the intermetallic particles were also quite low (i.e., approximately 1.3 and 1.5 vol.% in the low Si and high Si alloys, respectively). Therefore, the low volume fraction, large size and large interparticle spacing of the intermetallic particles limit their overall pinning ability.

During homogenization at different temperatures, phase transformations (Al_mFe to Al_3Fe and $\alpha\text{-AlFeSi}$ to Al_3Fe) occurred, and the type and size of intermetallic particles were partially modified. However, the size of the particles after homogenization was still large (1-20 μm), and their location in the microstructure remained unchanged (Fig. 3.2). Therefore, it is reasonable to conclude that the contribution to high temperature flow stress

from the various intermetallic particles and their distributions produced by changes in the alloy composition and homogenization treatment is not significant.

3.3.5.2 Impact of solute elements

Solute elements can have a strong influence on the hot deformation behavior of aluminum alloys by interacting with mobile dislocations and retarding softening processes [5, 23, 26]. The solution strengthening effect of a solute is strongly dependent on the specific solvent/solute pair [27]. The rapid solidification of the permanent mold casting used in this study resulted in the retention of Fe and Si atoms in the supersaturated solid solution. Therefore, the as-cast samples typically exhibited the highest flow stress in both alloys. Homogenization at a lower temperature (550 °C) significantly reduced the flow stress compared to the as-cast condition due to the elimination of Fe and Si supersaturation. However, an increase in the homogenization temperature from 550 to 630 °C increased the flow stresses by 10-23% and 15-45% for the low and high Si alloys, respectively (Figs. 3.8 and 3.9). The increase in flow stress is believed to be closely related to the high solid solution levels of both Fe and Si produced at a higher homogenization temperature.

Figure 3.11 shows the Al-Fe phase diagram where the solubility of iron increases rapidly as the temperature increases [28]. The iron solid solubility limits for the Al-Fe binary system at 550, 590 and 630 °C are approximately 0.012, 0.024 and 0.04%, respectively (i.e., the iron solute content can be more than tripled over this temperature range). Although iron typically has low solid solubility in aluminum (i.e., several hundred ppm), it is a potent solute that has a significant influence on dislocation movement due to

its low diffusivity [29]. Marshall et al. [30] reported that very small concentrations of iron in a solid solution of high purity aluminum may suppress softening processes. Shelby et al. [29] also demonstrated that a small amount of iron in solution (i.e., at the level of several hundred ppm) could significantly improve the creep resistance of pure aluminum.

In addition to the effect of iron solid solubility, the phase transformation from α -AlFeSi to Al_3Fe at higher temperatures released Si atoms to the matrix and increased the overall solute level, which augmented the flow stress. For the high Si alloy, α -AlFeSi was the dominant intermetallic phase, and it occupied approximately 60% of the total intermetallic volume fraction prior to the transformation (Fig. 3.4b). The phase transformation of α -AlFeSi to Al_3Fe at 630 °C produced a significant increase in the silicon content in the solid solution (Fig. 3.7b), which resulted in a significant increase in the flow stress that exceeded the as-cast value.

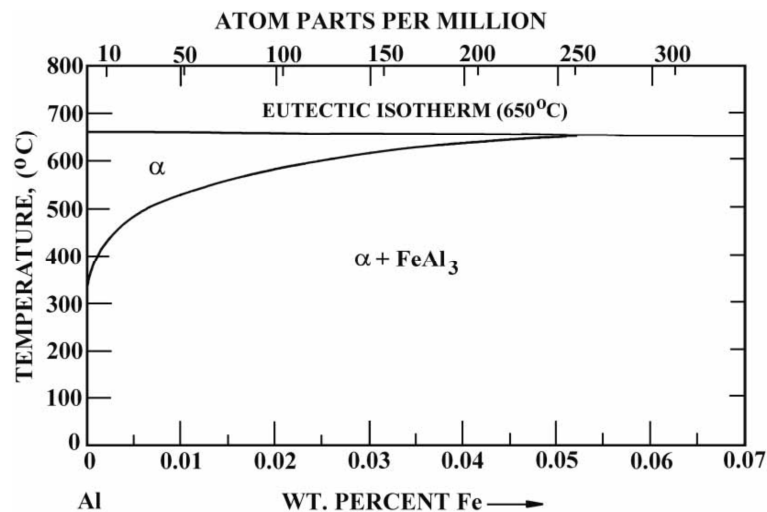


Fig. 3.11. Phase diagram of the binary Al–Fe system showing the solid solubility of iron in aluminum as a function of temperature [27].

In summary, for dilute Al-Fe-Si alloys, the effect of intermetallic particles on the flow stress is quite limited. The solute level of iron and silicon in the solid solution is believed to be the predominant factor controlling the flow stress and therefore the hot workability of the alloy.

3.3.5.3 *Industrial aspect*

Based on industrial experience, the as-cast microstructure is undesirable for hot deformation processes (e.g., high speed hot extrusion of thin wall tubing) due to the inherent high solid solution levels, which promote high flow stress, and the coarse intermetallic structures, which can cause hot ductility related surface defects, such as die lines or pick-up. The selection of homogenization parameters (i.e. temperature and time) should consider both aspects.

Homogenization of dilute Al-Fe-Si alloys induces a progressive transformation either from Al_mFe to Al_3Fe at lower temperatures or from $\alpha-AlFeSi$ to Al_3Fe at higher temperatures. In both cases, extended homogenization times can promote coarsening of Al_3Fe , which may be detrimental to the hot ductility and surface finish quality of extruded products.

The results of the current study indicate that the solute levels of Fe and Si are the key factors controlling the flow stress during hot deformation of dilute Al-Fe-Si alloys. Homogenization at a lower temperature (550 °C) eliminated the supersaturation of solute elements and therefore greatly reduced the flow stress. However, an increase in the homogenization temperature cannot further soften the materials, as traditionally believed.

On the contrary, an increase in the homogenization temperature significantly increased the flow stress up to 23 and 45% from 500 to 630 °C for the low and high Si alloys, respectively, due to the increase in the solid solution levels at higher temperatures. Increases of this magnitude in the flow stress are highly significant for the extrusion process where the productivity is typically limited by the press capacity. One of the key factors affecting extrusion productivity of dilute Al-Fe-Si alloys is the high temperature flow stress. In general, an extrusion press has a specific pressure available to push the billet through the die and this is a direct function of the flow stress. Aluminum alloys exhibit strain rate sensitivity, namely the higher the strain rate (the ram speed), the higher the flow stress is. Therefore, for a given press capacity and profile geometry, the flow stress of the material will dictate the maximum ram speed at which the press can operate. A higher flow stress also produces a larger temperature increase during extrusion, which increases the surface exit temperature for a given extrusion speed resulting in an earlier onset of surface defects.

If the minimum flow stress is the primary consideration, the use of a relatively low homogenization temperature, such as 550°C, offers significant potential benefits in terms of the extrusion speed and productivity for dilute Al-Fe-Si alloys. A reduction in the silicon level can also be beneficial. In comparison to the low Si alloy, the high Si alloy exhibited higher flow stresses (4 to 11%) for a given deformation condition. This further increase in flow stress is also significant in term of the processing speed. This effect was further compounded at high homogenization temperatures by the release of Si during the α -AlFeSi to Al₃Fe transformation, which resulted in a further increase in flow stress. Commercially,

an increase in Si in the alloy is often utilized to increase the room temperature strength. Therefore, there is a potential trade-off between these two aspects. If the final mechanical property requirement dictates the use of a high silicon alloy, the proper selection of homogenization temperature and time should be considered to avoid the phase transformation from α -AlFeSi to Al_3Fe .

3.4 Conclusions

- 1) The as-cast microstructures of two dilute Al-Fe-Si alloys (Al-0.3Fe-0.1Si and Al-0.3Fe-0.25Si) consisted of α -Al dendrites and metastable Al_mFe and α -AlFeSi, as well as equilibrium Al_3Fe intermetallic particles. The proportion of α -AlFeSi intermetallic increased with a higher silicon content.
- 2) Homogenization promoted the phase transformation from the metastable Al_mFe or α -AlFeSi phase to the equilibrium Al_3Fe phase via a dissolution-reprecipitation mechanism. The Al_mFe dissolved and transformed completely at 550°C in both alloys. The α -AlFeSi was transformed at 590°C in the low Si alloy (Al-0.3Fe-0.1Si), whereas it began to decompose and transform to Al_3Fe at 630°C in the high Si alloy (Al-0.3Fe-0.25Si).
- 3) Homogenization at 550°C significantly reduced the solid solution levels in both alloys due to the elimination of the supersaturation originating from the cast ingot. Above 550°C , the solid solution levels progressively increased.
- 4) The flow stress behavior of dilute Al-Fe-Si alloys was primarily controlled by the solute levels of Fe and Si. Homogenization at 550°C produced the lowest flow stress for all of the deformation conditions studied. An increase in the

homogenization temperature from 550 to 630°C increased the flow stress by 10 to 23% and 15 to 45% for the low Si and high Si alloys, respectively, which is commercially significant in terms of the productivity during hot forming processes.

- 5) An increase in the silicon content from 0.10 to 0.25% in dilute Al-0.3Fe-Si alloys increased the solid solution levels for all of the homogenized conditions studied, which resulted in an increase in the overall flow stress by 4 to 11%.

References

- [1] J.R. Davis, Aluminum and aluminum alloys. Materials Park, OH, ASM International, 1993, pp. 59-87.
- [2] J.G. Kaufman, Introduction to aluminum alloys and tempers. Materials Park, OH, ASM International, 2000, pp. 87-118.
- [3] J. Zhang, B. Chen, Z. Baoxiang, Effect of initial microstructure on the hot compression deformation behavior of a 2219 aluminum alloy, *Mater. Des.*, 2012, 34, pp.15-21.
- [4] H. Li, Z. Li, M. Song, X. Liang, F. Guo, Hot deformation behavior and microstructural evolution of Ag-containing 2519 aluminum alloy, *Mater. Des.*, 2010, 31, pp.2171-6.
- [5] H.J. McQueen, S. Spigarelli, M.E. Kassner, E. Evagelista, Hot deformation and processing of aluminum alloys. Florida, CRC Press, 2011, pp. 14–16 and 143–190.
- [6] Y.V.R.K. Prasad, K.P. Rao, Effect of homogenization on the hot deformation behavior of cast AZ31 magnesium alloy, *Mater. Des.*, 2009, 30, pp.3723-30.
- [7] Y. Totik, M. Gavgali, The effect of homogenization treatment on the hot workability between the surface and the center of AA 2014 ingots, *Mater. Charact.*, 2002, 49, pp.261-8.
- [8] S. Liu, J. You, X. Zhang, Y. Deng, Y. Yuan, Influence of cooling rate after homogenization on the flow behavior of aluminum alloy 7050 under hot compression, *Mater. Sci. Eng. A*, 2010, 527, pp.1200-5.
- [9] P. Liu, T. Thorvaldsson, G.L. Dunlop, Formation of intermetallic compounds during solidification of dilute Al-Fe-Si alloys, *Mater. Sci. Technol.*, 1986, 2, pp.1009-18.
- [10] P. Skjerpe, Intermetallic phases formed during DC-casting of an Al-0.25 Wt Pct Fe-0.13 Wt Pct Si alloy, *Metall. Trans. A*, 1987, 18, pp.189-200.
- [11] D.V. Malakhov, D. Panahi, M. Gallerneault, On the formation of intermetallics in rapidly solidifying Al-Fe-Si alloys, *CALPHAD*, 2010, 34, pp.159-66.

- [12] C.M. Allen, K.a.Q. O'reilly, B. Cantor, P.V. Evans, Intermetallic phase selection in 1XXX Al alloys, *Prog. Mater. Sci.*, 1998, 43, pp.89-170.
- [13] H. Kosuge, H. Takada, Phase change of the metastable phases in Al-Fe alloys at elevated temperatures, *J. Jpn. Inst. light Metal.*, 1979, 29, pp.64-9.
- [14] A. Griger, V. Stefániay, A. Lendavi, T. Turmezey, Possible modification of cast structure by continuous casting technology in AlFeSi alloys Part III: Intermetallic phases, *Alum*, 1989, 10, pp.1049-56.
- [15] Y.J. Li, L. Arnberg, A eutectoid phase transformation for the primary intermetallic particle from $Alm(Fe,Mn)$ to $Al_3(Fe,Mn)$ in AA5182 alloy, *Acta Mater.*, 2004, 52, pp.2945-52.
- [16] Y. Wang, H. Jones, P.V. Enans, The influence of third alloying elements on solidification microstructure of Al-3Fe alloys produced by Bridgman unidirectional growth, In: Beech J, Jones H, editors, 4th decennial international conference on solidification processing. Sheffield, UK, 1997. pp. 568-71.
- [17] X.G. Chen, Effect of grain refiners on intermetallic phases in AA1xxx simulated DC castings, In: Eckert CE, editor, 128th TMS Annual Meeting 'Light Metals'. San Diego, CA, USA, 1999. pp. 803-9.
- [18] P. Villars, D.L. Calvert, Pearson's handbook of crystallographic data for intermetallic phases. Materials Park, OH, ASM International, 1991.
- [19] Z. Zhang, G. Li, X.G. Chen, Identification and distribution of Fe intermetallic phases in AA5657 DC cast ingots, In: Weiland H, Rollett AD, Cassada WA, editors, 13th international conference on aluminum alloys. Pittsburgh, PA, USA, 2012. pp. 1857-63.
- [20] Z. Zhang, G. Li, X.G. Chen, Effect of nickel and vanadium on iron – bearing intermetallic phases in AA5657 simulated DC castings, *Mater. Sci. Technol.*, 2013, 30, pp.951-61.
- [21] M.V. Kral, H.R. McIntyre, M.J. Smillie, Identification of intermetallic phases in a eutectic Al–Si casting alloy using electron backscatter diffraction pattern analysis, *Scripta Mater.*, 2004, 51, pp.215-9.
- [22] H. Tezuka, A. Kamio, Influence of minor elements on the crystallization manner of intermetallic phases in unidirectionally solidified Al-Fe alloys, In: Arnberg L, editor, 3rd International conference, Aluminium alloys: their physical and mechanical properties. Trondheim, Norway, 1992. pp. 117-22.
- [23] J. Zhang, F. Pan, R. Zuo, C. Bai, The low temperature precipitation in commercial-purity aluminium sheets for foils, *J. Mater. Process. Technol.*, 2008, 206, pp.382-7.
- [24] J.E. Hatch, Aluminum: properties and physical metallurgy. Metals Park, OH, ASM, 1984, pp. 200-241.
- [25] H.W. Huang, B.L. Ou, C.T. Tsai, Effect of homogenization on recrystallization and precipitation behavior of 3003 aluminum alloy, *Mater. Trans.*, 2008, 49, pp.250-9.

[26] Q. Zhao, M. Slagvold, B. Holmedal, Comparison of the influence of Si and Fe in 99.999% purity aluminum and in commercial-purity aluminum, *Scripta Mater.*, 2012, 67, pp.217-20.

[27] F.J. Humphreys, M. Hatherly, *Recrystallization and related annealing phenomena*, Second ed. Oxford, Elsevier Ltd., 2004, p. 228.

[28] J.K. Edgar, Solubility of iron in solid aluminum, *Trans AIME*, 1949, 180, pp.225-9.

[29] O.D. Sherby, A. Goldberg, O.A. Ruano, Solute-diffusion-controlled dislocation creep in pure aluminium containing 0.026 at.% Fe, *Philos. Mag.*, 2004, 84, pp.2417-34.

[30] G.J. Marshall, R.A. Ricks, Role of Iron during Recovery and Recrystallization of Aluminium-Iron Alloys, In: Fuentes M, Sevillano JG, editors, *Recrystallization'92*. San Sebastian, Spain, 1992. pp. 245-50.

CHAPTER 4

EFFECT OF IRON AND SILICON CONTENT ON THE HOT COMPRESSIVE DEFORMATION BEHAVIOR OF DILUTE AL-FE-SI ALLOYS

CHAPTER 4

**EFFECT OF IRON AND SILICON CONTENT ON THE HOT
COMPRESSIVE DEFORMATION BEHAVIOR OF DILUTE AL-FE-SI
ALLOYS²**

Abstract

The hot deformation behavior of dilute Al-Fe-Si alloys (1xxx) containing various amounts of Fe (0.1 to 0.7 wt%) and Si (0.1 to 0.25 wt%) was studied by uniaxial compression tests conducted at various temperatures (350-550 °C) and strain rates (0.01-10 s⁻¹). The flow stress of the 1xxx alloys increased with increasing Fe and Si content. Increasing the Fe content from 0.1 to 0.7% raised the flow stress by 11-32% in Al-Fe-0.1Si alloys, whereas the flow stress increased 5-14% when the Si content increased from 0.1 to 0.25% in Al-0.1Fe-Si alloys. The influence of the temperature and the strain rate on the hot deformation behavior was analyzed using the Zener-Holloman parameter, and the effect of the chemical composition was considered in terms of the materials constants in the constitutive analysis. The proposed constitutive equations yielded an excellent prediction of the flow stress over wide ranges of temperature and strain rate with various Fe and Si contents. The microstructural analysis results revealed that the dynamic recovery is the sole softening mechanism of the 1xxx alloys during hot deformation. Increasing the Fe and Si

² Published at J. Mater. Eng. Perform., 24, 2015, 404-415.

content retarded the dynamic recovery and resulted in a decrease in the subgrain size and mean misorientation angle of the boundaries.

4.1 Introduction

The 1xxx series aluminum alloys are primarily used for applications in which superior formability and excellent thermal and electrical conductivity are required. Typical applications include foil and strips for packaging, heat-exchanger tubing and fin stock, coaxial cable sheathing and electrical conductors [1, 2]. These products are generally subjected to hot-forming processes such as extrusion and rolling. Therefore, the development of a method to analyze and predict their hot deformation behavior under various thermomechanical conditions is the primary goal.

The high-temperature flow behavior of various materials in hot-forming processes is very complex. The work hardening and dynamic softening are both significantly affected by many factors, such as the chemical composition, the forming temperature, the strain rate and the strain [3, 4]. The flow behavior of materials is very important for the design of hot-forming processes due to its substantial impact on the required deformation load as well as the kinetics of metallurgical transformations. Traditionally, the trial and error method has been employed to optimize the thermomechanical processes. To overcome the huge number of tests required to achieve a reliable conclusion in the trial and error practice, various modeling techniques have been developed that permit a significant reduction in the production cost.

The modeling of materials flow behavior is often conducted by proper constitutive equations, which correlates the dynamic material properties such as the flow stress to the process parameters such as the deformation temperature and strain rate [5-7]. Normally, uniaxial hot compression tests are employed to provide the necessary data to extract the constitutive equations. Several analytical [8], phenomenological [9], and empirical [10] models have been proposed to describe the high temperature flow behavior for a wide range of metals and alloys. Johnson and Cook [11] proposed a phenomenological model to develop a cumulative-damage fracture model. Sellars et al. [12] proposed a hyperbolic-sine constitutive law to describe the elevated temperature flow behavior of various materials. Sloof et al. [13] introduced a strain-dependent parameter into the hyperbolic sine constitutive equation to improve its accuracy. Lin et al. [14] proposed a revised hyperbolic sine constitutive equation to describe the flow behavior of 42CrMo steel by considering the compensation of the strain and strain rate. Ashtiani et al. [6] established strain-compensated constitutive equations to predict the flow behavior of commercially pure aluminum. Among various constitutive equations available, the hyperbolic sine constitutive equation, proposed by Sellars et al. [12], has proven to be applicable over a wide range of materials and alloys [5-7, 15, 16].

Commercial 1xxx aluminum alloys exhibit higher strength and work hardening than high purity aluminum. The main alloying additions, or controlled impurities, in these alloys are Fe and Si. Zhao et al. [17] reported that Fe and Si play a major role in the strength and work hardening of commercial 1xxx alloys and that the contribution from the other impurities is negligible. McQueen et al. [4, 18, 19] concluded that dynamic recrystallization

(DRX) could not occur in commercially pure aluminum (1xxx alloys) and that dynamic recovery (DRV) was the sole restoration mechanism during hot deformation. Although a few researchers [4, 6, 19] have studied the hot deformation behavior of commercially pure aluminum, no systematic investigation of the influence of different Fe and Si contents on the hot deformation behavior of dilute Al-Fe-Si alloys is available in the literature.

In the present study, the hot deformation behavior of dilute Al-Fe-Si alloys with a systematic variation of the Fe and Si contents was investigated by hot compression tests conducted at various deformation temperatures and strain rates. The experimental stress-strain data were employed to drive constitutive equations correlating flow stress, deformation temperature and strain rate considering the influence of the chemical composition. Moreover, the effects of the deformation conditions and the chemical composition on the microstructural evolution associated with the dynamic softening were investigated.

4.2 Experimental

To cover the range of Fe and Si of commercial interest in 1xxx alloys, seven dilute Al-Fe-Si alloys containing 0.1 to 0.7 % Fe and 0.1 to 0.25 % Si were investigated (all alloy compositions in this study are in wt% unless otherwise indicated). The chemical compositions of the experimental alloys are presented in Table 4.1. They were prepared from commercially pure aluminum (99.7%), Al-20%Fe and Al-50%Si master alloys. For each composition, approximately 5 kg of material was melted in an electrical resistance furnace and then cast into a rectangular, permanent steel mold measuring 30×40×80 mm³.

Prior to the cast, the melts were grain-refined by an addition of 0.015% Ti in the form of an Al-5Ti-1B master alloy. The cast ingots of these alloys were homogenized at 550 °C for 6 h, followed by water quenching at ambient temperature.

Cylindrical samples of 10 mm in diameter and 15 mm in height were machined from the homogenized ingots. The uniaxial hot-compression tests were conducted using a Gleeble 3800 thermomechanical testing unit at strain rates of 0.01, 0.1, 1 and 10 s⁻¹ and temperatures of 350, 400, 450, 500 and 550 °C. During the tests on the Gleeble 3800 unit, the specimens were heated at a rate of 2 °C/s and maintained for 120 s at the desired temperature to ensure a homogeneous temperature distribution. The specimens were deformed to a total true strain of 0.8 and then immediately water-quenched to retain the deformed microstructure.

Table 4.1. Chemical compositions of the experimental alloys (wt%).

Alloys	Si	Fe	Cu	Mn	Cr	Ni	Ti	Zr	V
Al-0.1Fe-0.1Si	0.10	0.12	0.002	0.001	0.001	0.007	0.016	0.0015	0.012
Al-0.3Fe-0.1Si	0.10	0.28	0.003	0.002	0.001	0.007	0.017	0.0015	0.012
Al-0.5Fe-0.1Si	0.10	0.49	0.004	0.002	0.001	0.007	0.017	0.0014	0.012
Al-0.7Fe-0.1Si	0.11	0.68	0.006	0.003	0.001	0.007	0.018	0.0013	0.012
Al-0.1Fe-0.25Si	0.24	0.13	0.002	0.001	0.001	0.007	0.018	0.0014	0.012
Al-0.3Fe-0.25Si	0.24	0.30	0.001	0.002	0.001	0.007	0.017	0.0014	0.012
Al-0.5Fe-0.25Si	0.26	0.52	0.002	0.002	0.001	0.008	0.017	0.0015	0.012

The deformed samples were sectioned parallel to the compression axis along the centerline direction. Because conventional mechanical polishing can cause surface plastic deformation on the relatively soft surfaces of commercially pure aluminum and introduces a large number of artifacts in the electron backscattered diffraction (EBSD) maps, an argon ion-beam cross-section polisher (JEOL SM-09010) was employed in this study. All samples were polished in an Ar⁺ ion beam at 5 kV with a current of 80 mA for 8 h. The microstructural evolution of the compressed samples was investigated using the EBSD technique under a scanning electron microscope (SEM, JEOL JSM-6480LV). In the EBSD analysis, the boundaries of grains and subgrains are defined as low-angle boundaries, medium-angle boundaries and high-angle boundaries with misorientation angles of 1-5°, 5-15° and greater than 15°, respectively [20]. The step size between the scanning points was set as 1.0 μm. The line intercept method was used to measure the subgrain size of the deformed samples. To ensure the statistical reliability, more than 100 subgrains were measured in each sample. For the quantitative measurement of the misorientation distribution of the boundaries, EBSD line scanning was performed with a step size of 0.2 μm.

4.3 Result and discussion

4.3.1 Flow stress behavior

A series of true stress-true strain curves were obtained for all seven alloys at various deformation temperatures (350 to 550 °C) and strain rates (0.01 to 10 s⁻¹). Figures 4.1 and 4.2 display typical true stress-true strain curves for the Al-0.1Fe-0.1Si and Al-0.5Fe-0.1Si

alloys as examples. At the beginning of deformation, the flow stress increased rapidly because of dislocation multiplication and the high rate of work hardening [21, 22]. Subsequently, the flow stress increased at a decreasing rate with an increase in the strain and then either remained fairly constant or, in certain cases with a high Zener-Holloman parameter (Z), continued to increase until the end of the deformation. The steady state regime (after the strain of ~ 0.1) gives evidence of a constant dislocation density as a result of a balance of the work hardening and the dynamic softening. In the cases of high Z , the strain hardening without saturation is indicative of the work hardening being stronger than the dynamic softening during the deformation. In general, both flow behaviors are characteristic of high temperature deformation in which dynamic recovery (DRV) is the dominant softening mechanism [18, 21, 23]. The effects of the deformation temperature and strain rate on the flow stress behavior of these alloys were significant. The flow stress increased with decreasing deformation temperature and increasing strain rate, which is in good agreement with previously reported results [4, 6, 24]. The highest value of the flow stress was obtained at a strain rate of 10 s^{-1} and a temperature of $350 \text{ }^\circ\text{C}$ for all of the alloys investigated, whereas by decreasing the strain rate to 0.01 s^{-1} and increasing the temperature to $550 \text{ }^\circ\text{C}$, the flow stress reached its minimum value.

Figures 4.3 and 4.4 demonstrate the influence of the Fe and Si levels on the flow stress at a strain of 0.8 for all of the alloys at two extremes of strain rates (0.01 and 10 s^{-1}), respectively. Increasing the Fe content increases the flow stress at all deformation conditions (Fig. 4.3). However, its effect was more significant when the Si level remained low (0.1 %). For example, in the low Si series alloys (Al-Fe-0.1Si), at a given deformation

condition ($350\text{ }^{\circ}\text{C}$ and 0.1 s^{-1}), increasing the iron content from 0.1 to 0.3 and 0.5 % increased the flow stress from 34.9 to 38.3 and 40.2 MPa, respectively. In the high Si series alloys (Al-Fe-0.25Si), by raising the Fe content from 0.1 to 0.3 and 0.5, the flow stress increased from 39.5 to 42.1 and 42.8 MPa, respectively. Generally, in the case of the low Si alloys, raising the iron content from 0.1 to 0.5 % increased the flow stress by 7 to 26% over the range of deformation conditions studied. However, by raising the iron content from 0.1 to 0.5 % in the high Si series alloys, the flow stress increased only 4 to 16%.

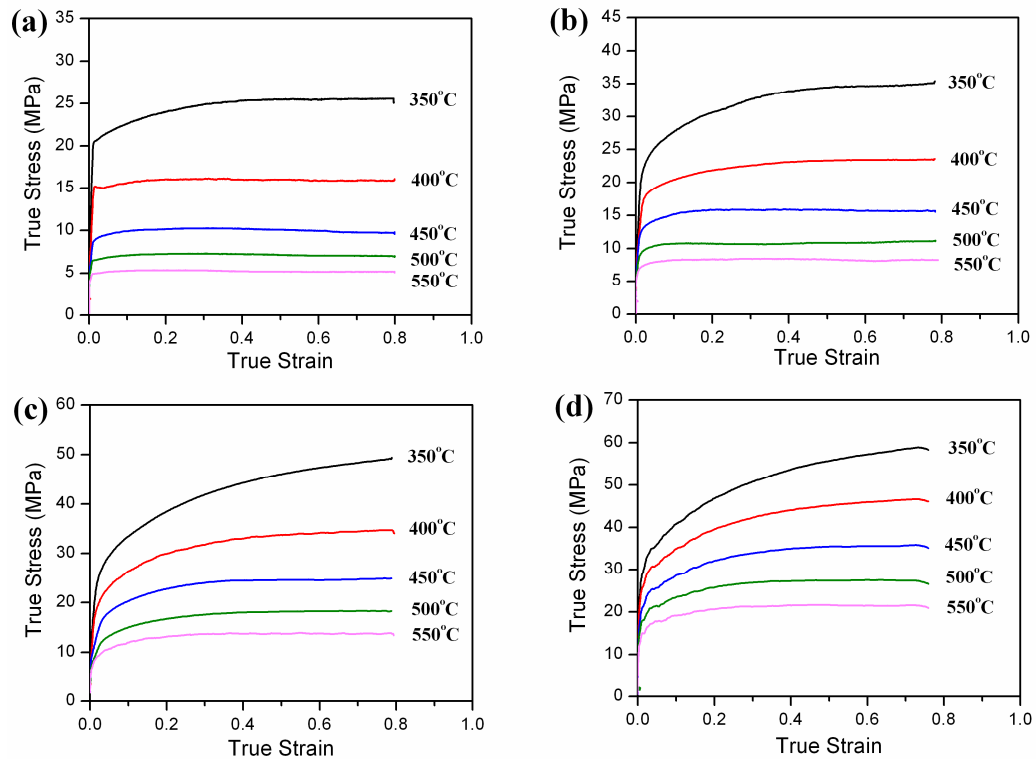


Fig.4.1. True stress-true strain curves of Al-0.1Fe-0.1Si alloy at various strain rates (a) $\dot{\epsilon} = 0.01\text{ s}^{-1}$, (b) $\dot{\epsilon} = 0.1\text{ s}^{-1}$, (c) $\dot{\epsilon} = 1\text{ s}^{-1}$ and (d) $\dot{\epsilon} = 10\text{ s}^{-1}$.

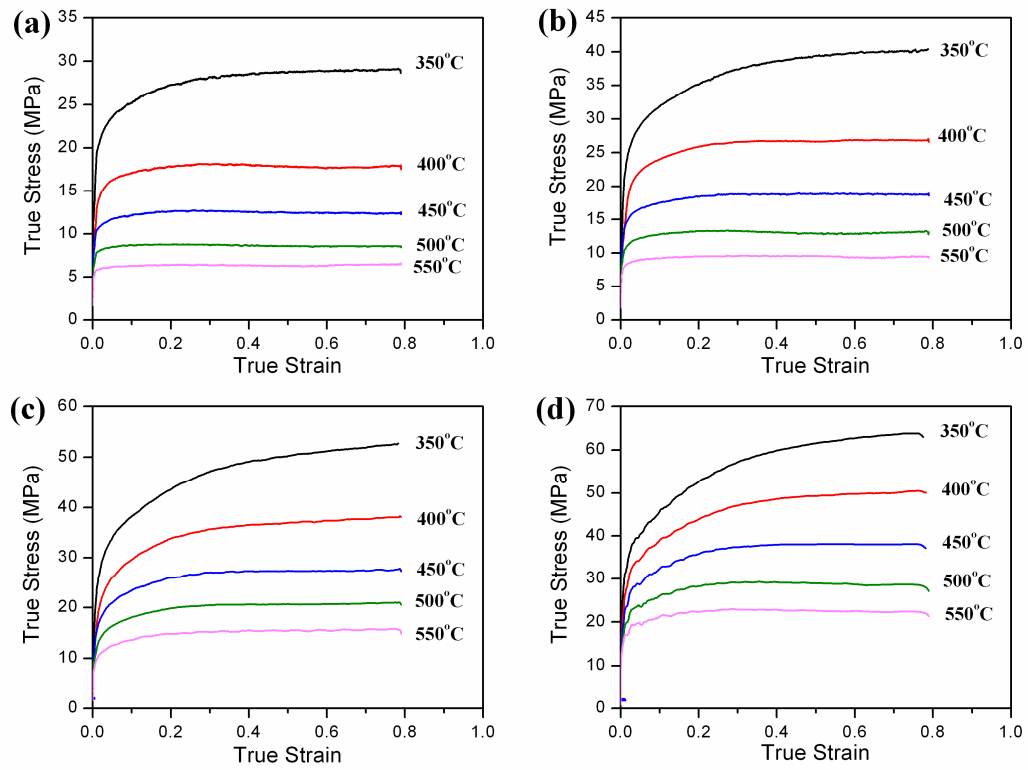


Fig.4.2. True stress-true strain curves of Al-0.5Fe-0.1Si alloy at various strain rates (a) $\dot{\epsilon} = 0.01 \text{ s}^{-1}$, (b) $\dot{\epsilon} = 0.1 \text{ s}^{-1}$, (c) $\dot{\epsilon} = 1 \text{ s}^{-1}$ and (d) $\dot{\epsilon} = 10 \text{ s}^{-1}$.

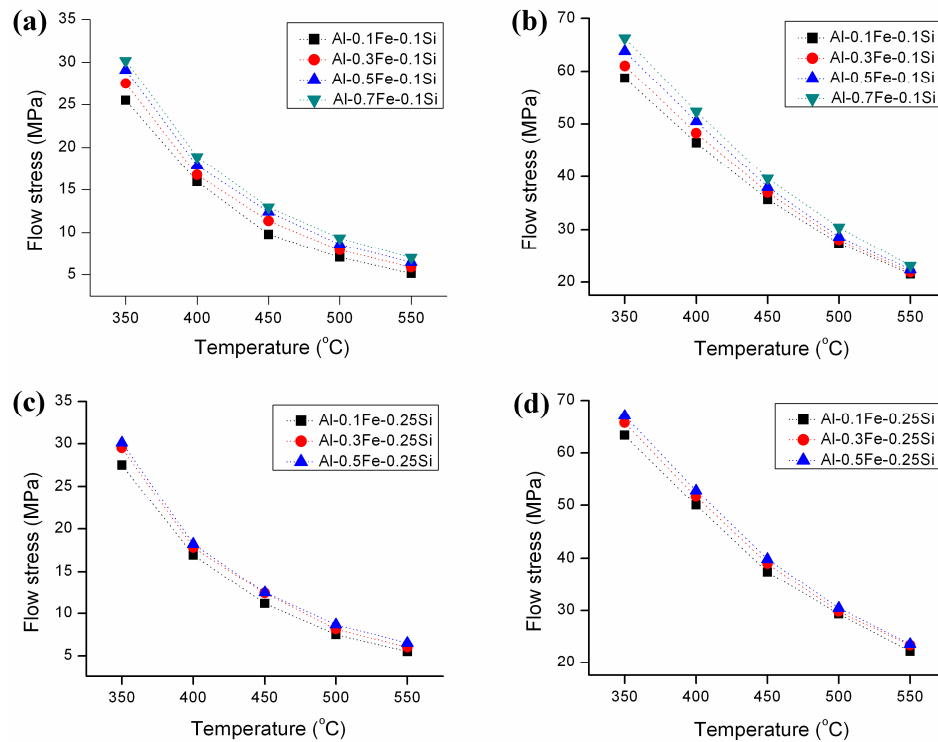


Fig.4.3. Effect of iron on flow stress at strain of 0.8, (a) Al-Fe-0.1Si $\dot{\epsilon} = 0.01 \text{ s}^{-1}$, (b) Al-Fe-0.1Si $\dot{\epsilon} = 10 \text{ s}^{-1}$, (c) Al-Fe-0.25Si $\dot{\epsilon} = 0.01 \text{ s}^{-1}$ and (d) Al-Fe-0.25Si $\dot{\epsilon} = 10 \text{ s}^{-1}$.

As seen in Fig. 4.4, the addition of Si can also increase the flow stress of dilute Al-Fe-Si alloys. Raising the silicon content from 0.1 to 0.25 % in the Al-0.1Fe and Al-0.5Fe alloys increased the flow stress by 4 to 14% and 2 to 8%, respectively, over the range of deformation conditions applied. The results indicate that the influence of the Si content was more evident at a low Fe level. It appears that the impact of the individual alloy additions was more significant when the concentration of the other element was low.

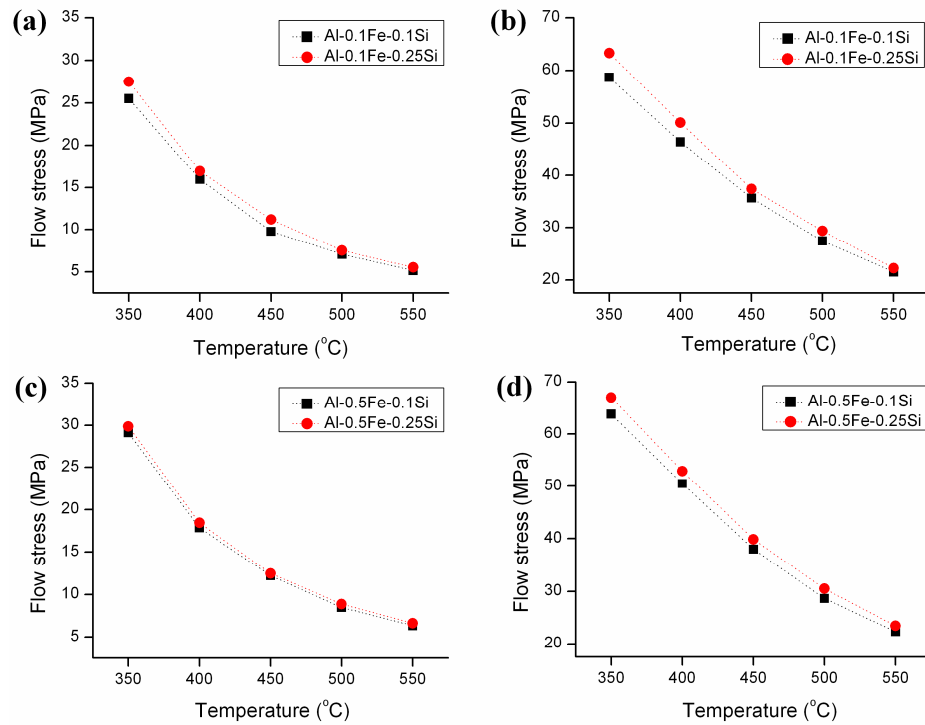


Fig.4.4. Effect of silicon on flow stress at strain of 0.8, (a) Al-0.1Fe-Si $\dot{\epsilon} = 0.01 \text{ s}^{-1}$, (b) Al-0.1Fe-Si $\dot{\epsilon} = 10 \text{ s}^{-1}$, (c) Al-0.5Fe-Si $\dot{\epsilon} = 0.01 \text{ s}^{-1}$ and (d) Al-0.5Fe-Si $\dot{\epsilon} = 10 \text{ s}^{-1}$.

4.3.2 Constitutive analysis

Constitutive equations are widely used to model the hot-deformation behavior of metals and alloys. At elevated temperature, the strain rate ($\dot{\epsilon}$) is related to the temperature and flow stress, by the Arrhenius type equation [7, 13, 24, 25].

$$\dot{\epsilon} = Af(\sigma)\exp\left(-\frac{Q}{RT}\right) \quad (4.1)$$

where $\dot{\epsilon}$ is the strain rate (s^{-1}), A is a constant, Q is the activation energy for hot deformation (KJ mol^{-1}), R is the universal gas constant ($8.314 \text{ J mol}^{-1} \text{ K}^{-1}$), T is the absolute temperature (K) and $f(\sigma)$ is the stress function which can be expressed as [5, 15, 26-28]:

$$f(\sigma) = \begin{cases} \sigma^{n_1} & \alpha\sigma < 0.8 \\ \exp(\beta\sigma) & \alpha\sigma > 1.2 \\ [\sinh(\alpha\sigma)]^n & \text{for all } \sigma \end{cases} \quad (4.2)$$

where σ is the flow stress (MPa), n_1 , β and n are material constant and $\alpha = \beta/n_1$ [26-28] is a stress multiplier. Generally, the power law equation break down at high stress values, and the exponential equation break down at low stress values. However, the hyperbolic-sine law proposed by Sellars and McTegart [12], is suitable for constitutive analysis over a wide range of temperatures and strain rates [3, 7, 13, 24, 25]. Furthermore, the effect of the temperature and the strain rate on the hot-deformation behavior could be represented by the Zener-Holloman parameter (Z) in an exponential equation [6, 7, 21, 29]:

$$Z = \dot{\epsilon} \exp\left(\frac{Q}{RT}\right) \quad (4.3)$$

Using the experimental results obtained from the hot-compression tests at various temperatures and strain rates, the material constants and activation energy of the above mentioned equations could be determined for all alloys investigated. The following is the solution procedure for determining the materials constants and activation energy, using an Al-0.1Fe-0.1Si alloy as an example. In this study, the value of σ is taken from the value of the flow curves at a true stain of 0.8.

For the low ($\alpha\sigma < 0.8$) and the high ($\alpha\sigma > 1.2$) stress levels, substituting suitable function (the power law and exponential law of $f(\sigma)$) into Eq. (4.1) leads to Eqs. (4.4) and (4.5), respectively:

$$\dot{\epsilon} = A_1 \sigma^{n_1} \quad (4.4)$$

$$\dot{\epsilon} = A_2 \exp(\beta\sigma) \quad (4.5)$$

where A_1 and A_2 are the material constants. Taking the natural logarithm of both sides of Eqs. (4.4) and (4.5) yields,

$$\ln(\sigma) = \frac{1}{n_1} \ln \dot{\epsilon} - \frac{1}{n_1} \ln A_1 \quad (4.6)$$

$$\sigma = \frac{1}{\beta} \ln \dot{\epsilon} - \frac{1}{\beta} \ln A_2 \quad (4.7)$$

Then, substituting the values of the flow stresses and corresponding strain rates into the Eqs. (4.6) and (4.7) gives the relationship between the flow stress and strain rate, as shown in figure 4.5. The value of β and n_1 could be obtained from the slope of the lines in the $\ln \dot{\epsilon} - \sigma$ and $\ln \dot{\epsilon} - \ln \sigma$ plots, respectively. The mean values of β and n_1 for the range of temperature studied were found to be 0.2841 and 5.8959, respectively. Consequently, the value of α was defined as $\alpha = \beta/n_1 = 0.048 \text{ MPa}^{-1}$.

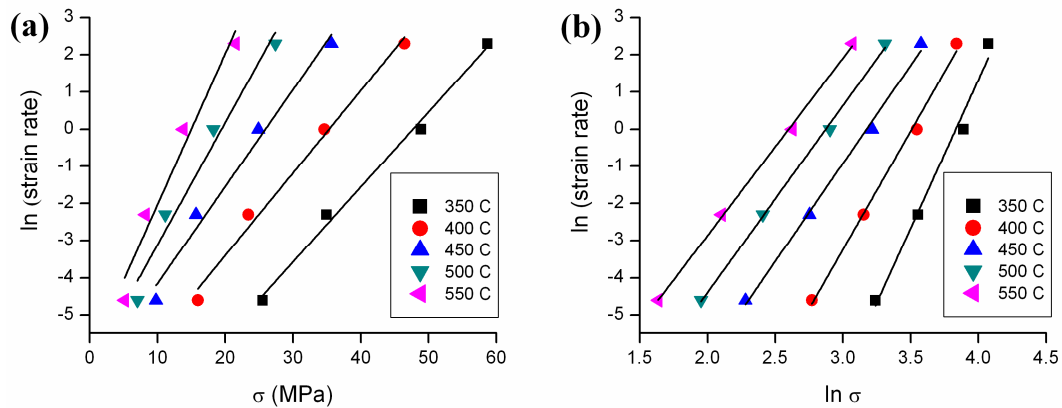


Fig.4.5. Plots of (a) $\ln \dot{\epsilon} - \sigma$ and (b) $\ln \dot{\epsilon} - \ln \sigma$ for Al-0.1Fe-0.1Si alloy.

For wide range of stress level, Eq. (4.1) could be represented as the hyperbolic sine law:

$$\dot{\epsilon} = A[\sinh(\alpha\sigma)]^n \exp\left(-\frac{Q}{RT}\right) \quad (4.8)$$

Differentiating Eq. (4.8) results in:

$$Q = R \left[\frac{\partial \ln \dot{\epsilon}}{\partial \ln[\sinh(\alpha\sigma)]} \right]_T \left[\frac{\partial \ln[\sinh(\alpha\sigma)]}{\partial (1000/T)} \right]_{\dot{\epsilon}} = RnS, \quad (4.9)$$

where R is a universal gas constant, n is the mean slope of $\ln \dot{\epsilon}$ vs. $\partial \ln[\sinh(\alpha\sigma)]$ at various temperatures and S is the mean slope of the $\partial \ln[\sinh(\alpha\sigma)]$ vs. $\partial(1000/T)$ at various strain rates. Figure 4.6 exhibits the relationship between $\ln \dot{\epsilon} - \partial \ln[\sinh(\alpha\sigma)]$ and $\partial \ln[\sinh(\alpha\sigma)] - \partial(1000/T)$ for the Al-0.1Fe-0.1Si alloy. Therefore, the values of n, S and Q of the Al-0.1Fe-0.1Si alloy can be obtained from Fig. 4.6 and Eq. 4.9. Combining Eq. (4.8) with Eq. (4.3) results in:

$$Z = \dot{\epsilon} \exp\left(\frac{Q}{RT}\right) = A[\sinh(\alpha\sigma)]^n \quad (4.10)$$

Taking the natural logarithm of both sides of Eq. (10) results in:

$$\ln Z = \ln A + n \ln[\sinh(\alpha\sigma)] \quad (4.11)$$

The linear correlation between $\ln Z$ and $\ln[\sinh(\alpha\sigma)]$ are shown in Figure 4.7. The value of $\ln A$ is the intercept of the plot of $\ln Z$ vs. $\ln[\sinh(\alpha\sigma)]$.

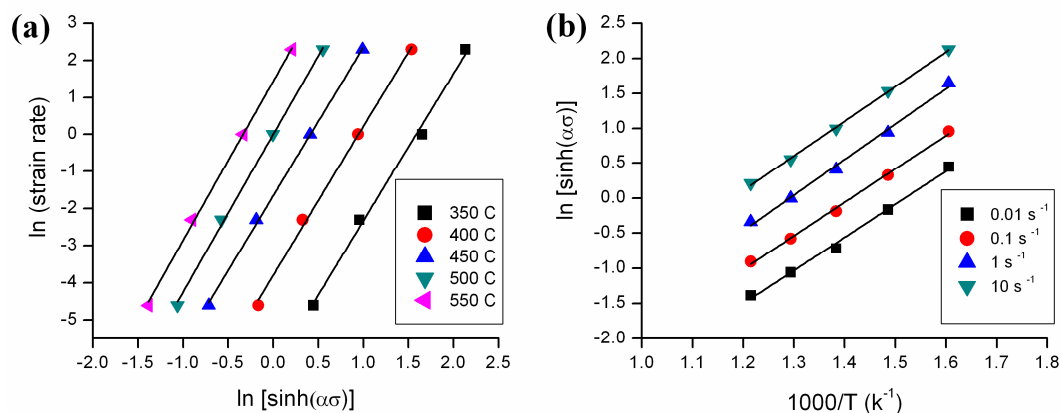


Fig.4.6. Plots of (a) $\ln\dot{\epsilon}$ vs. $\ln[\sinh(\alpha\sigma)]$ and (b) $\ln[\sinh(\alpha\sigma)]$ vs. $(1000/T)$ for Al-0.1Fe-0.1Si alloy.

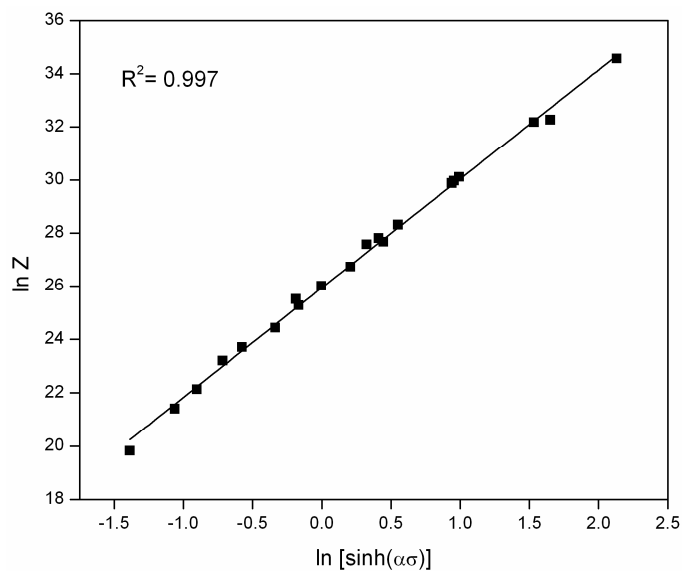


Fig.4.7. Plot of $\ln Z$ vs. $\ln[\sinh(\alpha\sigma)]$ for Al-0.1Fe-0.1Si alloy.

In a similar way, the values of the materials constants, α , n and A , as well as the activation energy, Q , can be computed for all of the other alloys. Table 4.2 presents the values of the materials constants and activation energies corresponding to all of the alloys

investigated. As can be seen, the value of α decreases as the values of n , A and Q increase with increasing Fe or Si contents. The calculated values of the activation energies of 1xxx alloys lie between 167 and 182 KJ/mol in this study, values which are in general agreement with those reported previously for commercially pure aluminum [3, 4, 19, 21, 30, 31].

Table 4.2. Values of material constants and activation energies of all experimental alloys.

Alloys	α (MP ⁻¹)	n	A (s ⁻¹)	Q (KJ/mol)
Al-0.1Fe-0.1Si	0.048	4.11	1.84E+11	167.2
Al-0.3Fe-0.1Si	0.046	4.36	5.75E+11	174.5
Al-0.5Fe-0.1Si	0.044	4.52	1.50E+12	181.2
Al-0.7Fe-0.1Si	0.043	4.48	1.55E+12	181.9
Al-0.1Fe-0.25Si	0.046	4.08	2.87E+11	171.3
Al-0.3Fe-0.25Si	0.043	4.30	1.16E+12	179.6
Al-0.5Fe-0.25Si	0.042	4.35	8.42E+11	177.8

4.3.3 Effect of chemical composition

So far, the constitutive equations have been employed to study the influences of deformation conditions such as the temperature and strain rate on the flow stress of individual alloys with a specific chemical composition. As can be seen, the effect of the chemical composition is not considered in Eqs. (4.1) and (4.3). In this section, the effects of the chemical composition on the materials constants and activation energy in the constitutive equations were also considered. Fulfilling this goal, the values of the materials constants and activation energy (α , n , $\ln A$ and Q) obtained from the constitutive equations are considered as a function of the Fe content. Figure 4.8 illustrates the variation in the materials constants and activation energy with differing Fe contents for both the low- and

high-Si series alloys. A second-order polynomial function, as shown in Eq. (4.12), was found to represent the influence of the Fe content with very good correlation and generalization (Fig. 4.8). The coefficients of the polynomial fit are provided in Tables 4.3 and 4.4 for the alloys containing 0.1 and 0.25 Si, respectively.

$$\begin{aligned}
 \alpha &= B_0 + B_1Fe + B_2Fe^2 \\
 Q &= C_0 + C_1Fe + C_2Fe^2 \\
 n &= D_0 + D_1Fe + D_2Fe^2 \\
 \ln A &= E_0 + E_1Fe + E_2Fe^2
 \end{aligned}
 \tag{4.12}$$

where Fe is the Fe content in wt%.

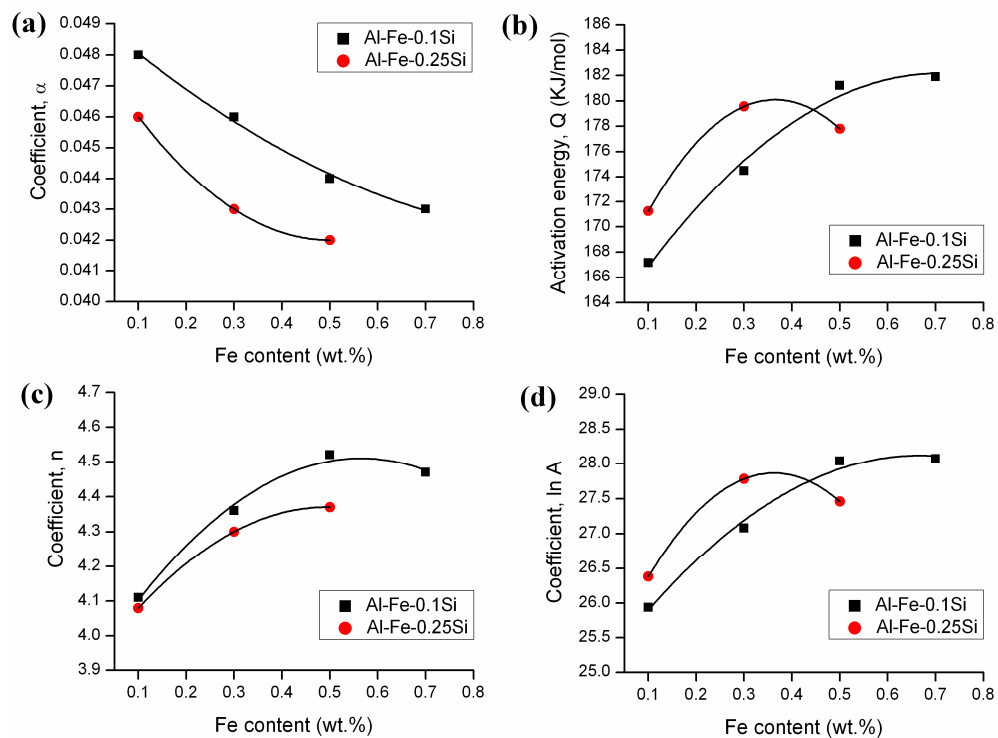


Fig.4.8. Relationship between (a) α (b) Q, (c) n and (d) $\ln A$ and Fe level by polynomial fit for both Al-Fe-0.1Si or Al-Fe-0.25Si alloys.

Table 4.3. Coefficients of the polynomial fit of α , Q, n and lnA for the Al-Fe-0.1Si alloy.

α		Q		n		ln A	
B ₀	0.0493	C ₀	161.44	D ₀	3.9108	E ₀	25.049
B ₁	-0.0135	C ₁	58.565	D ₁	2.12	E ₁	9.2095
B ₂	0.0063	C ₂	-41.313	D ₂	-1.875	E ₂	-6.9063

Table 4.4. Coefficients of the polynomial fit of α , Q, n and lnA for the Al-Fe-0.25Si alloy.

α		Q		n		ln A	
B ₀	0.0483	C ₀	163.34	D ₀	3.9063	E ₀	25.04
B ₁	-0.025	C ₁	91.85	D ₁	1.95	E ₁	15.595
B ₂	0.025	C ₂	-125.87	D ₂	-2.125	E ₂	-21.512

Figure 4.8 demonstrates that the polynomial function provides a good description of the relationship between the materials constants and the Fe level in 1xxx alloys. The value of α decreases with increasing Fe content, whereas the values of n and A increase with increasing Fe contents for both the low and high Si alloys. Moreover, the activation energy for hot deformation, Q, is an important indicator of the degree of difficulty of plastic deformation. The change in the hot deformation activation energy as a function of the Fe content for both the low and high Si series are shown in Fig. 4.8b. The Q values gradually increase with increasing Fe content in all of the alloys except for Al-0.5Fe-0.25Si. It is worth noting that the effect of the Fe content on the activation energy is more significant at low Fe levels. By increasing the Fe content from 0.1 to 0.5% in the low Si series alloys, the Q value increases from 167.2 to 181.2 kJ/mol, whereas its value only slightly increases from 181.2 to 181.9 kJ/mol as the Fe content increases from 0.5 to 0.7%. On the other hand, the value of the activation energy even slightly decreases from 179.6 to 177.8 kJ/mol in the high Si series alloys as the Fe content increases from 0.3 to 0.5 %.

From Eq. (4.10), the flow stress, σ , can be expressed as a function of the Zener-Hollomon parameter as follows:

$$\sigma = \frac{1}{\alpha} \ln \left\{ \left(\frac{Z}{A} \right)^{\frac{1}{n}} + \left[\left(\frac{Z}{A} \right)^{\frac{2}{n}} + 1 \right]^{\frac{1}{2}} \right\}. \quad (4.13)$$

After the relationship between the materials constants and the Fe content are well established, the flow stress of the 1xxx alloys with various compositions (Fe level) at any given deformation condition can be predicted by employing Eq. (4.13).

To verify the constitutive equations developed for dilute Al-Fe-Si alloys, the predicted flow stress values were plotted against the experimental flow stress measurements (Fig. 4.9). The correlation coefficients between the experimental and predicted results were greater than 99% for all of the alloys investigated. It can be seen that the proposed models could accurately predict the flow stress of 1xxx alloys through the entire range of Fe contents, temperatures and strain rates, which means that they can be used for numerical simulation of the hot deformation process and in choosing the proper deformation parameters in commercial practice.

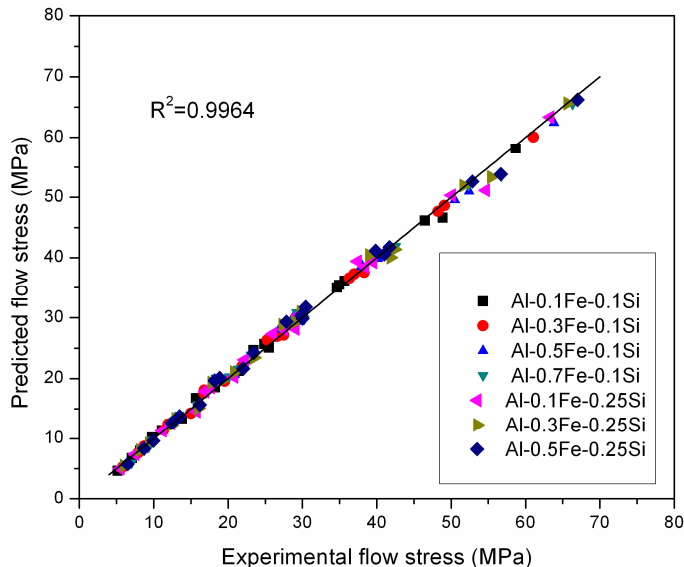


Fig.4.9. Correlation between the experimental and predicted flow stress of 1xxx alloys.

4.3.4 Microstructural evolution during hot deformation

Figure 4.10 illustrates optical micrographs of Al-0.1Fe-0.1Si and Al-0.5Fe-0.25Si alloys after homogenization. Because the solid solubility of iron in aluminum is very low (i.e., max. 0.05% at 650 °C), most of the iron combines with both aluminum and silicon to form secondary Fe-rich intermetallic phases [32, 33]. These Fe-rich intermetallic particles are distributed predominantly in the dendrite cell boundaries. In the homogenized microstructure, the dominant constituent phase was Al₃Fe in the low Si series alloys, whereas in the high Si series alloys, the major phase was α -AlFeSi. With increasing Fe content, the number of Fe-rich intermetallic particles increases. Increasing the Si content increases the amounts of the constituent particles and solute atoms simultaneously. A

detailed description of the Fe-rich intermetallic phases in dilute Al-Fe-Si alloys and the effects of homogenization were reported in our previous study [34].

To study the influence of the deformation conditions on the microstructural evolution of Al-Fe-Si alloys, the Al-0.1Fe-0.1Si composition was selected to be analyzed by EBSD, and the effect of the deformation conditions on the misorientation angle of the boundaries and the subgrain size were quantitatively evaluated. Figure 4.11 shows orientation imaging maps of the deformed microstructure under various deformation conditions for the Al-0.1Fe-0.1Si alloy after compression to a strain of 0.8. In hot-worked aluminum alloys, the original grain boundaries are generally characterized by high-angle boundaries ($> 15^\circ$), whereas low-angle boundaries ($1-5^\circ$) and medium-angle boundaries ($5-15^\circ$) form subgrain structures [22].

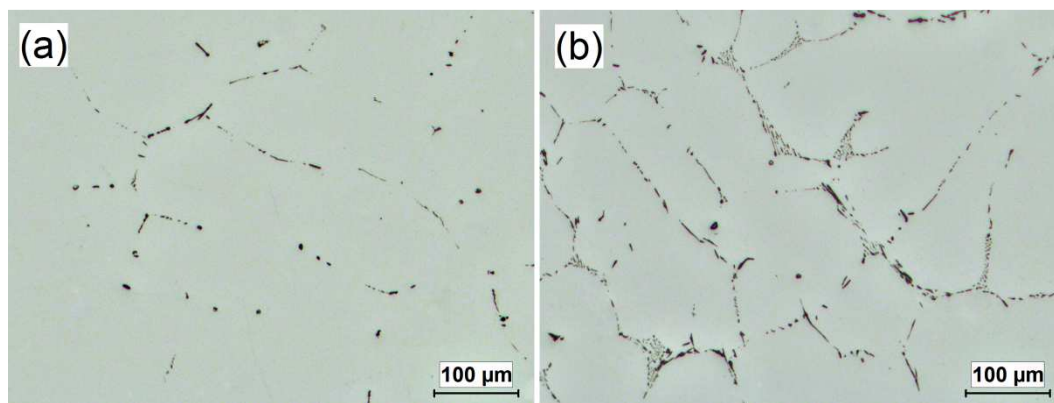


Fig. 4.10. As-homogenized microstructures of (a) Al-0.1Fe-0.1Si and (b) Al-0.5Fe-0.1Si.

During hot deformation, the original grains were elongated perpendicular to the compression direction. The deformation performed at a high Z condition (400 °C and 10 s^{-1}) resulted in a high density of low-angle boundaries and consequently a great number of small subgrains (Fig. 4.11(a)). Irregular deformation bands were observed inside the original grains (see arrows in Fig. 4.11(a)) due to the deformation occurring on a different slip system [22]. When the strain rate was reduced to 0.01 s^{-1} at a temperature of 400 °C, the deformation bands became less visible, and larger subgrains were formed with neatly arranged boundaries (Fig. 4.11(b)), thereby indicating an increased level of dynamic recovery due to the greater time for dislocation polygonization [22]. Furthermore, when the temperature increased to 500 °C at a strain rate of 0.01 s^{-1} , the substructure was further recovered, which involved the rearrangement and annihilation of dislocations, resulting in the presence of coarsened subgrains with higher-angle boundaries (Fig. 4.11(c)). The increased polygonization consisted of an enlargement of the subgrains and the rearrangement of the subboundary dislocations into neater networks [19].

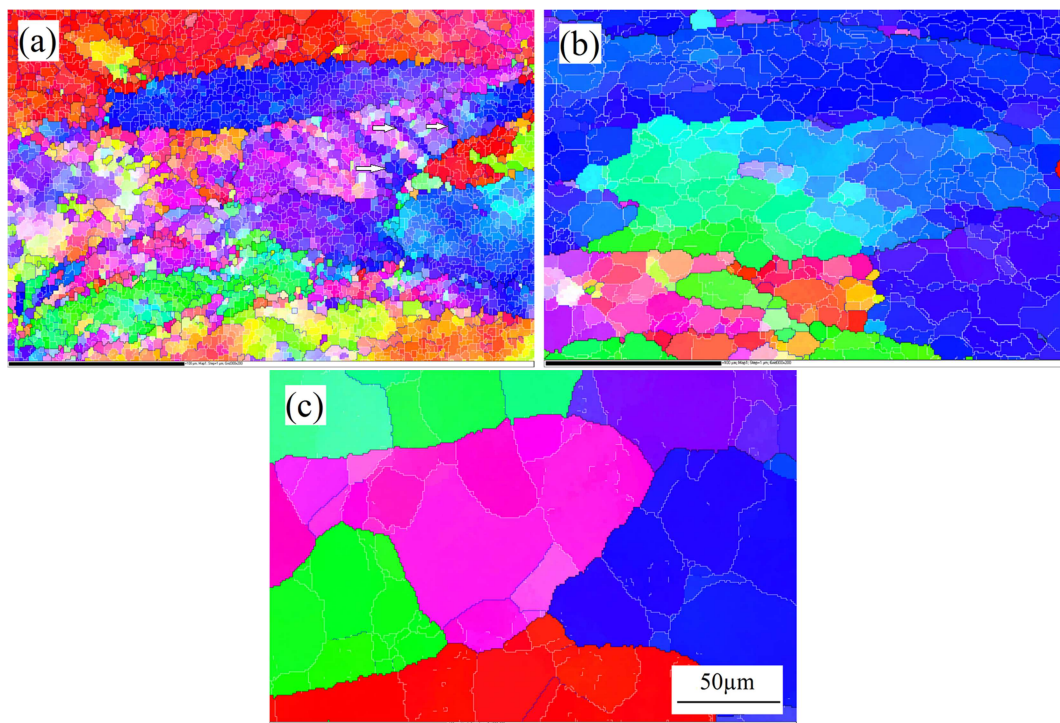


Fig.4.11. Orientation imaging maps of Al-0.1Fe-0.1Si alloy under various deformation conditions: (a) 10 s^{-1} , $400 \text{ }^{\circ}\text{C}$, (b) 0.01s^{-1} , $400 \text{ }^{\circ}\text{C}$ and (c) 0.01s^{-1} , $500 \text{ }^{\circ}\text{C}$. White lines $1\text{-}5^{\circ}$, blue lines $5\text{-}15^{\circ}$ and black lines $> 15^{\circ}$.

Table 4.5 shows the variation in the mean misorientation angle and the subgrain sizes with the deformation conditions in the Al-0.1Fe-0.1Si alloy. As the temperature increased and the strain rate decreased, both the mean misorientation angle of the boundaries and the subgrain size increased. This suggests a higher rate of dynamic recovery with increasing temperature and decreasing strain rate [21, 22], which is consistent with the microstructural observations shown in Fig. 4.11. Dynamic recovery is a thermally activated process, of which the level is improved as the temperature increases [22]. When the strain rate

decreases, the increased level of dynamic recovery is attributed to the increased time for subgrain coalescence [21, 22].

Table 4.5. Evolution of the mean misorientation angle and the subgrain size under various deformation conditions in the Al-0.1Fe-0.1Si alloy.

Deformation condition	Mean misorientation angle (°)	Subgrain size (μm)
400 °C / 10 s ⁻¹	7.42	3.58
400 °C / 0.01 s ⁻¹	9.27	7.29
500 °C / 0.01 s ⁻¹	13.27	16.52

To understand the effect of the Fe and Si content on the microstructural evolution of 1xxx alloys, a fixed deformation condition (500 °C and 0.01 s⁻¹) was selected to compare different alloys. Figure 4.12 illustrates the orientation imaging maps of the deformed samples with various Fe and Si contents. The impact of Fe on the subgrain structure can be seen from Fig. 4.11(c) and Figs. 4.12(a) and (b) as the Fe content increases from 0.1 via 0.3 to 0.5%. Generally, samples displayed a similar deformed microstructure, where only dynamic recovery occurred during hot deformation. However, the levels of the dynamic recovery of those samples varied with the Fe contents, as also shown in Figure 4.13. At a given Si content, both the mean misorientation angle of the boundaries and the subgrain size were continuously decreased with increasing Fe contents. For example, the Al-0.7Fe-0.1Si alloy displays the smallest mean misorientation angle and subgrain size among the four low-Si alloys, indicating a slowing of the dynamic recovery with increased Fe content. On the other hand, when comparing Fig. 4.11(c) with Fig. 4.12 (c) and Fig. 4.12(b) with Fig. 4.12(d), it is found that the high-Si alloys exhibited finer subgrain structures relative to

the low-Si alloys. At the same Fe content, the higher the Si level, the lower the mean misorientation angle and the smaller the subgrain size were (Fig. 4.13). These results indicate a decreased level of dynamic recovery as the Si content increases. To find a quantitative relationship between the average subgrain diameter and the deformation conditions, three alloys (Al-0.1Fe-0.1Si, Al-0.1Fe-0.25Si and Al-0.5Fe-0.1Si) were selected for analysis. Fig. 4.14(a) shows the relationship between the deformation conditions (Z) and the subgrain diameter (d). It is apparent that the subgrain size became smaller as the Zener-Hollomon parameter increased, and a good linear fit between the reciprocal subgrain diameter and the logarithm of the Zener-Hollomon parameter is found, as expressed in Eq. 4.14:

$$d^{-1} = 0.0193 \ln Z - 0.3598. \quad (4.14)$$

Figure 4.14(b) illustrates the relationship between the steady-state flow stress and the subgrain diameter. It is evident that the flow stress increases with decreasing subgrain diameter, and a linear function between the steady-state flow stress and the reciprocal subgrain diameter, based on the equation proposed by McQueen et al. [35] and Jonas et al. [36], is established (Eq. 4.15):

$$\sigma_s = 191.35d^{-1} - 7.53. \quad (4.15)$$

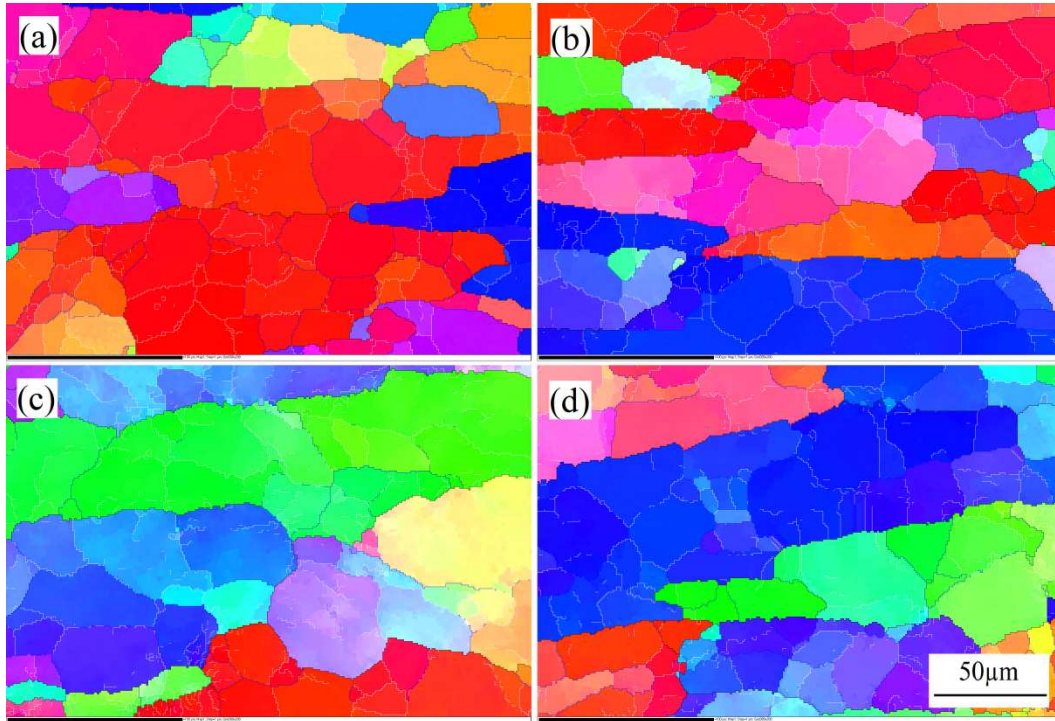


Fig.4.12. Orientation imaging maps of (a) Al-0.3Fe-0.1Si (b) Al-0.5Fe-0.1Si, (c) Al-0.1Fe-0.25Si and (d) Al-0.5Fe-0.25Si alloy deformed at 500 °C and 0.01s^{-1} .

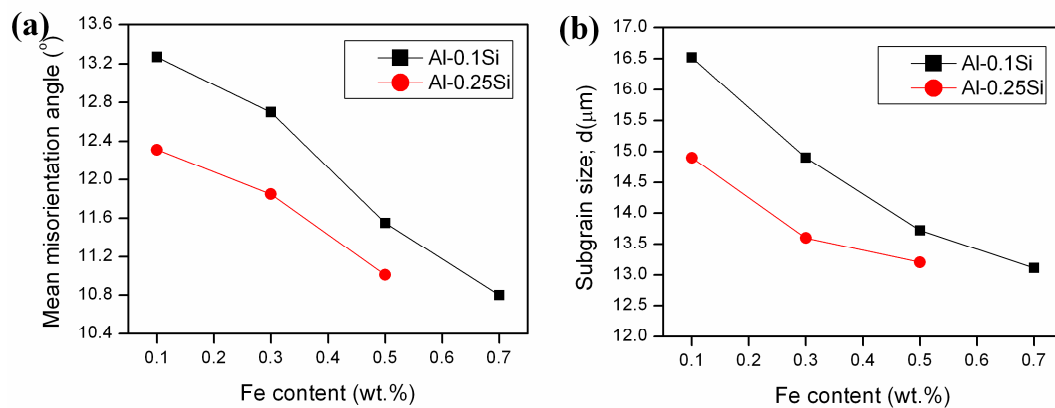


Fig.4.13. Effect of Fe and Si contents on (a) Mean misorientation angle, (b) subgrain size of 1xxx alloys deformed at 500 °C and 0.01s^{-1} .

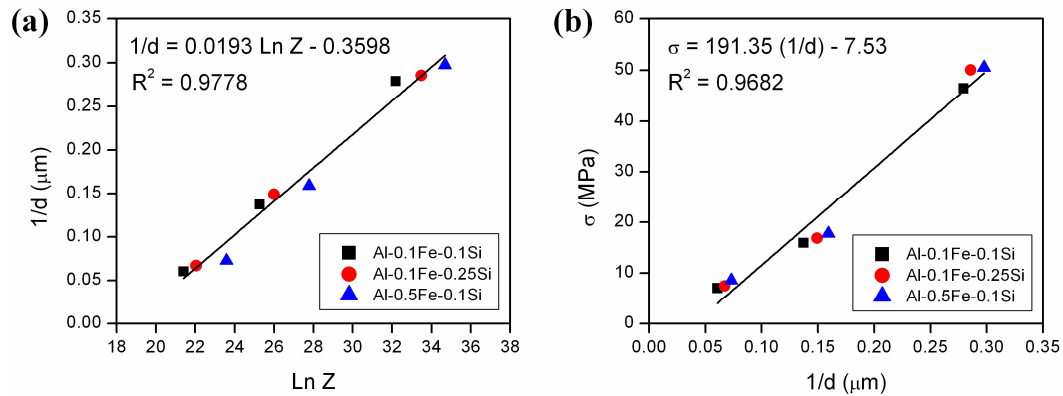


Fig. 4.14. Relationship between (a) the reciprocal subgrain diameter (d^{-1}) and logarithm of the Zener-Hollomon parameter (Z), (b) the steady-state flow stress (σ) and reciprocal subgrain diameter (d^{-1}).

The deformation conditions (Z), such as the temperature and strain rate define the steady-state subgrain size, which in turn determines the flow stress. As the temperature decreased and the strain rate increased, a high flow stress was induced as a result of the fine subgrain size generated during hot deformation. It should be mentioned that this relation could not be used at very high temperatures where the subgrain size becomes very large ($>25\mu\text{m}$).

Based on the microstructural observations in Figures 4.11 and 4.12, it is clear that dynamic recovery is the sole softening mechanism that operates during hot deformation of the dilute Al-Fe-Si alloys. The subgrain structures in these figures were the result of the mutual annihilation of many dislocations and the rearrangement of the remaining dislocation into regular low/medium-angle boundaries. This phenomenon is commonly observed during deformation in metals and alloys with high stacking fault energies [4, 18,

21]. The relatively high rate of dynamic recovery significantly offsets the work-hardening effect and reduces the driving force for dynamic recrystallization[21, 22]. It is evident that the level of dynamic recovery increases when the deformation temperature increases and the strain rate decreases, which is associated with an increase in the mean misorientation angle of the boundaries and the subgrain size (Table 4.5). Furthermore, the addition of Fe and Si enhances the strain hardening and impedes dynamic recovery during hot deformation, leading to a finer subgrain structure (Figs. 4.12 and 4.13). In the case of Fe addition, Fe-rich intermetallic particles greater than several μm in length cannot be sheared or bypassed by the moved dislocations [21]. The plastic deformation is performed by the flow of the aluminum matrix around them, which is associated with a local lattice rotation in the vicinity of the intermetallic particles [22]. This results in an increased deformation resistance and the formation of smaller subgrains near the intermetallic particles [21, 22]. With a higher Fe content, the increased amount of Fe-rich intermetallic particles acts as a stronger barrier to deformation and thus results in a further increase in the flow stress and a decrease in the overall subgrain size. On the other hand, Si addition increases both the amounts of Si solute atoms and intermetallic particles. The deformation resistance is increased due to the solute-drag effect and the enhanced barrier to plastic flow [21, 22, 37]. Therefore, at a given Fe addition, the alloy with a higher Si content demonstrates an increase in the flow stress and a decrease in the level of dynamic recovery.

The use of extruded 1xxx alloys is commercially important for the production of thin-walled tubing for refrigeration, heat transfer and conductor applications. Given the perceived simplicity of this alloy family, there is a surprisingly wide range of alloys in

commercial use just for extruded applications, including AA1050, AA1060, AA1235, AA1100 and AA1350, with many compositional variants within the registered AA specifications. Extrudability is a term used to capture the ability to process an alloy at high speed into thin-walled shapes; for 1xxx alloys, for which the extrusion ratios are high even with multistranding, this is primarily controlled by the flow stress. In general, this alloy family is considered to have good extrudability due to its dilute nature and high melting point. However, the current work has indicated that small changes in the iron and silicon content can have a significant impact on the flow stress and thus on the extrusion productivity and cost, which is an important aspect that should be considered for alloy selection and design.

4.4. Conclusions

In the present study, the hot-deformation behavior of dilute Al-Fe-Si alloys with a systematic variation in the Fe and Si contents was studied. From the results obtained, the following conclusions can be drawn.

- 1) Increasing the iron content increased the high temperature flow stress for all of the alloys studied. In the case of low Si (0.10%) alloys, increasing the iron level from 0.1 to 0.7% produced 11 to 32% increase in the flow stress over the range of deformation conditions investigated. However, for high Si (0.25%) alloys, by increasing the iron level from 0.1 to 0.5%, the flow stress increased only 4 to 16%.
- 2) The addition of silicon also increased the high-temperature flow stress. Increasing the silicon level from 0.1 to 0.25 % in the Al-0.1Fe and Al-0.5Fe alloys increased

the flow stress by 4-14% and 2-8%, respectively, over the range of deformation conditions investigated.

- 3) The materials constants and activation energies for hot-deformation as a function of the Fe content were determined from the experimental compression data obtained. The applied constitutive equations yielded an excellent predication of the flow stress over wide temperature and strain-rate ranges of 1xxx alloys with various Fe and Si contents.
- 4) The activation energy for hot deformation gradually increased with increasing Fe and Si contents. Increasing the Fe content from 0.1 to 0.7% in low-Si alloys increased the activation energy from 167.2 to 181.9 kJ/mol, whereas increasing the Si level from 0.1 to 0.25% in the Al-0.1Fe-Si alloy raised the activation energy from 167.2 to 171.2 kJ/mol.
- 5) Dynamic recovery is the sole softening mechanism operating during the hot deformation of dilute Al-Fe-Si alloys. The rate of the dynamic recovery increased with increasing deformation temperature and decreasing strain rate. Increasing the Fe and Si contents promoted the retardation of the dynamic recovery due to the increased amounts of intermetallic particles and Si solute atoms in the aluminum matrix.
- 6) The impact of small changes in the Fe and Si contents on the flow stress and resulting extrudability of 1xxx alloys is significant, and this fact should be considered in alloy selection and design for extruded applications.

References

- [1] J.R. Davis, Aluminum and aluminum alloys. Materials Park, OH, ASM International, 1993, pp. 59-87.
- [2] J.G. Kaufman, Introduction to aluminum alloys and tempers. Materials Park, OH, ASM International, 2000, pp. 87-118.
- [3] H.J. McQueen, N.D. Ryan, Constitutive analysis in hot working, Mater. Sci. Eng. A, 2002, 322, pp.43-63.
- [4] H.J. McQueen, E. Evangelista, N. Jin, M.E. Kassner, Energy dissipation efficiency in aluminum dependent on monotonic flow curves and dynamic recovery, Metall. Mater. Trans. A, 1995, 26, pp.1757-66.
- [5] H. Mirzadeh, A. Najafizadeh, M. Moazeny, Flow Curve Analysis of 17-4 PH Stainless Steel under Hot Compression Test, Metall. Mater. Trans. A, 2009, 40, pp.2950-8.
- [6] H.R. Rezaei Ashtiani, M.H. Parsa, H. Bisadi, Constitutive equations for elevated temperature flow behavior of commercial purity aluminum, Mater. Sci. Eng. A, 2012, 545, pp.61-7.
- [7] Y.C. Lin, Y.-C. Xia, X.-M. Chen, M.-S. Chen, Constitutive descriptions for hot compressed 2124-T851 aluminum alloy over a wide range of temperature and strain rate, Comput. Mater. Sci, 2010, 50, pp.227-33.
- [8] J. Luo, M. Li, X. Li, Y. Shi, Constitutive model for high temperature deformation of titanium alloys using internal state variables, Mech. Mater., 2010, 42, pp.157-65.
- [9] Y.C. Lin, Q.-F. Li, Y.-C. Xia, L.-T. Li, A phenomenological constitutive model for high temperature flow stress prediction of Al–Cu–Mg alloy, Mater. Sci. Eng. A, 2012, 534, pp.654-62.
- [10] S.B. Davenport, N.J. Silk, C.N. Sparks, C.M. Sellars, Development of constitutive equations for modelling of hot rolling, Mater. Sci. Technol., 2000, 16, pp.539-46.
- [11] G.R. Johnson, W.H. Cook, Fracture characteristics of three metals subjected to various strains, strain rates, temperatures and pressures, Eng. Fract. Mech., 1985, 21, pp.31-48.
- [12] C.M. Sellars, W.J. Mctegart, La relation entre la résistance et la structure dans la deformation à chaud, Mem. Sci. Rev. Met., 1966, 63, pp.731-46.
- [13] F.A. Slooff, J. Zhou, J. Duszczyk, L. Katgerman, Constitutive analysis of wrought magnesium alloy Mg–Al4–Zn1, Scripta Mater., 2007, 57, pp.759-62.
- [14] Y.-C. Lin, M.-S. Chen, J. Zhong, Constitutive modeling for elevated temperature flow behavior of 42CrMo steel, Comput. Mater. Sci, 2008, 42, pp.470-7.
- [15] Y.-C. Lin, M.-S. Chen, J. Zhang, Modeling of flow stress of 42CrMo steel under hot compression, Mater. Sci. Eng. A, 2009, 499, pp.88-92.

- [16] C. Shi, X.-G. Chen, Effect of Zr addition on hot deformation behavior and microstructural evolution of AA7150 aluminum alloy, *Mater. Sci. Eng. A*, 2014, 596, pp.183-93.
- [17] Q. Zhao, M. Slagvold, B. Holmedal, Comparison of the influence of Si and Fe in 99.999% purity aluminum and in commercial-purity aluminum, *Scripta Mater.*, 2012, 67, pp.217-20.
- [18] H.J. McQueen, W. Blum, Dynamic recovery: sufficient mechanism in the hot deformation of Al, *Mater. Sci. Eng. A*, 2000, 290, pp.95-107.
- [19] H. McQueen, J. Hockett, Microstructures of aluminum compressed at various rates and temperatures, *Metall. Trans.*, 1970, 1, pp.2997-3004.
- [20] F.J. Humphreys, Review Grain and subgrain characterisation by electron backscatter diffraction, *J. Mater. Sci.*, 2001, 36, pp.3833-54.
- [21] H.J. McQueen, S. Spigarelli, M.E. Kassner, E. Evagelista, Hot deformation and processing of aluminum alloys, Florida, CRC Press, 2011, pp. 87-190.
- [22] F.J. Humphreys, M. Hatherly, Recrystallization and related annealing phenomena, Second ed. Oxford, Elsevier Ltd., 2004, pp. 169-213 and 415-450.
- [23] H.J. McQueen, Metal forming: Industrial, mechanical computational and microstructural, *J Mater Process Technol*, 1993, 37, pp.3-36.
- [24] S. Banerjee, P.S. Robi, A. Srinivasan, L. Praveen Kumar, High temperature deformation behavior of Al–Cu–Mg alloys micro-alloyed with Sn, *Mater. Sci. Eng. A*, 2010, 527, pp.2498-503.
- [25] S.B. Brown, K.H. Kim, L. Anand, An internal variable constitutive model for hot working of metals, *Int. J. Plast.*, 1989, 5, pp.95-130.
- [26] S. Mandal, V. Rakesh, P.V. Sivaprasad, S. Venugopal, K.V. Kasiviswanathan, Constitutive equations to predict high temperature flow stress in a Ti-modified austenitic stainless steel, *Mater, Sci, Eng, A*, 2009, 500, pp.114-21.
- [27] Z.Y. Chen, S.Q. Xu, X.H. Dong, Deformation behavior of AA6063 aluminium alloy after removing friction effect under hot working conditions, *Acta Metall, Sin.*, 2008, 21, pp.451-8.
- [28] W. Li, H. Li, Z. Wang, Z. Zheng, Constitutive equations for high temperature flow stress prediction of Al–14Cu–7Ce alloy, *Mater. Sci. Eng. A*, 2011, 528, pp.4098-103.
- [29] A. Marandi, A. Zarei-Hanzaki, N. Haghdadi, M. Eskandari, The prediction of hot deformation behavior in Fe–21Mn–2.5Si–1.5Al transformation-twinning induced plasticity steel, *Mater. Sci. Eng. A*, 2012, 554, pp.72-8.
- [30] C.M. Sellar, W.J.M. Tegart, Hot workability, *Int. Met. Rev.*, 1972, 17, pp.1-24.
- [31] H.J. McQueen, P. Sakaris, Influence of stress multiplier in SINH equation on constitutive constants for Al alloys with Mg and dispersoids, *Aluminum alloys: Their*

Physical and Mechanical Properties (ICAA3), Vol.2, L. Arnberg, E. Nes, O. Lohne, N. Ryum, Eds., Trondheim, Norway, 1992, p 179-184.

[32] P. Liu, T. Thorvaldsson, G.L. Dunlop, Formation of intermetallic compounds during solidification of dilute Al-Fe-Si alloys, *Mater. Sci. Technol.*, 1986, 2, pp.1009-18.

[33] P. Skjerpe, Intermetallic phases formed during DC-casting of an Al-0.25 Wt Pct Fe-0.13 Wt Pct Si alloy, *Metall. Trans. A*, 1987, 18, pp.189-200.

[34] M. Shakiba, N. Parson, X.-G.Chen, Effect of homogenization treatment and silicon content on the microstructure and hot workability of dilute Al-Fe-Si alloys, *Mater. Sci. Eng. A*, 2014, 619, pp.180-9.

[35] H.J. McQueen, W.A. Wong, J.J. Jonas, Deformation of aluminium at high temperatures and strain rates, *Can. J. Phys.*, 1967, 45, pp.1225-34.

[36] J.J. Jonas, D.R. Axelrad, J.L. Uvira, On substructure strengthening and the high temperature deformation of cubic metals, *Trans. Japan Inst. Met.*, 1968, 9, pp.257-67.

[37] J. Zhang, F. Pan, R. Zuo, C. Bai, The low temperature precipitation in commercial-purity aluminium sheets for foils, *J. Mater. Process. Technol.*, 2008, 206, pp.382-7.

CHAPTER 5

HOT DEFORMATION BEHAVIOR AND RATE CONTROLLING

MECHANISM IN DILUTE AL-FE-SI ALLOYS WITH MINOR

ADDITIONS OF MN AND CU

CHAPTER 5

HOT DEFORMATION BEHAVIOR AND RATE CONTROLLING MECHANISM IN DILUTE AL-FE-SI ALLOYS WITH MINOR ADDITIONS OF MN AND CU

Abstract

The hot deformation behavior of dilute Al-Fe-Si alloys containing various amounts of Mn (0.1-0.2 wt%) and Cu (0.05-0.31 wt%) was investigated by hot compression tests conducted over a range of deformation temperatures (400-550 °C) and strain rates (0.01-10 s⁻¹). Both Mn and Cu in a solid solution have a significant influence on the hot workability of dilute Al-Fe-Si alloys. On a wt% basis, Mn exhibits a stronger strengthening effect compared with Cu. The activation energies for hot deformation were calculated from the experimental flow stress data obtained using a hyperbolic sine constitutive equation for all of the alloys investigated. The activation energy increased from 161 kJ/mol for the low-Fe base alloy to 181 kJ/mol for the alloy containing 0.2 wt% Mn, while the addition of Cu up to 0.31 wt% only slightly increased the activation energy to 166 kJ/mol. The solute diffusion acted as the deformation rate-controlling mechanism in these dilute alloys. Mn containing alloys have a higher flow stress and higher activation energy due to the considerably lower diffusion rate of Mn in aluminum compared with Cu containing alloys.

Dynamic recovery was the sole softening mechanism associated with the hot deformation of all of the alloys investigated. The addition of Mn and Cu retarded the dynamic recovery and decreased the subgrain size and mean misorientation angle of the grain boundaries.

5.1 Introduction

Al-Fe-Si (1xxx) wrought alloys are used in a wide range of applications where excellent formability, corrosion resistance, and electrical and thermal conductivity are desirable. Typical applications include foil and strip for packaging and heat-exchanger tubing, cable sheathing and fin stock [1, 2]. Generally, the levels of iron and silicon in a specific alloy are controlled to yield the required material properties, such as strength, formability and corrosion resistance. The effects of iron and silicon contents on the hot workability of the 1xxx alloys have previously been reported by Shakiba et al. [3]. Increasing both the iron and silicon content generally increases the high temperature flow stress, which can negatively impact the hot workability [3]. Consequently, there is a trade-off between room temperature mechanical properties and hot workability. An alternate approach to increase the room temperature strength is to add minor alloying elements, such as manganese and copper, for solid solution strengthening, which is the case in the widely used AA1100 alloys.

Mn is normally added to aluminum in order to control the dynamic softening processes. Generally, Mn in presence of iron and silicon, forms coarse constituent particles and fine dispersoids that serve as obstacles against grain boundary migration and dislocation movement [4, 5]. Mn also has a significant influence on the strength of

aluminum alloys when present in a solid solution [4]. Copper is often added to improve the strength of aluminum [1, 6]. However, addition of Cu more than 1.1% results in the formation of coarse intermetallics during casting, which act as initiation sites for corrosion. Compared with the negative effect of copper-containing large intermetallics on corrosion, the research work [7] shows rather a favorable influence on corrosion resistance while the copper remains in a solid solution.

A significant amount of work has been reported on the solid solution strengthening of materials [4, 8-10]. Solute additions result in a retardation of dislocation movement, an enhanced rate of dislocation multiplication and a restriction of dynamic softening processes [10, 11]. The size and shear modulus differences between solute atoms and a solvent matrix both have significant impact on the strengthening effect of solute elements [8, 12, 13]. Normally, the size effect is strong, which produces an attractive force between the solute atoms and the dislocation cores [13]. The shear modulus difference becomes significant when the solvent and solute atoms show similar sizes [13]. Spittel et al. [12] showed that 1% Mg with a higher atomic radius difference increases the flow stress of aluminum more significantly than 1% Cu with a smaller atomic radius difference. Ryen et al. [4] revealed that both Mg and Mn in a solid solution give a nearly linear concentration dependence of strength for commercially pure aluminum alloys. Due to the clustering effect between Mn and trace elements in a solid solution, Mn gave a considerably higher hardening effect per atom compare with Mg. Furu et al. [5] showed that an addition of 1% Mg produces a solute drag effect during the hot deformation of aluminum resulting in a smaller subgrain size and a lower misorientation angle. Sherby et al. [14] studied the effect

of additions of trace amounts of iron on the creep behavior of pure aluminum and found that the creep rate is controlled by the rate of the solute atom diffusion in the subgrain boundary region.

The present investigation was conducted to assess the impact of minor Mn and Cu additions on the hot workability of commercial 1xxx alloys with the long term view of optimizing alloy design in terms of strength and hot processability. Hence, the hot deformation behavior of dilute Al-Fe-Si alloys with different levels of Mn and Cu was investigated by a hot compression test conducted at various temperatures and strain rates. The experimental data were employed to derive constitutive equations correlating flow stress, deformation temperature and strain rate. The values of the activation energy and other material constants were calculated for each alloy using a hyperbolic sine type constitutive equation. The effects of Mn and Cu additions on the microstructural evolution associated with the dynamic softening process were also studied.

5.2 Experimental procedure

Commercially pure aluminum (99.7%), Al-20%Fe, Al-50%Si, Al-25%Mn and Al-50%Cu master alloys were employed to prepare the experimental alloys. All alloy compositions in this study are in wt% unless otherwise indicated. The chemical compositions of the experimental alloys are presented in Table 5.1. The additions of 0.1 and 0.2 % Mn were made to two different base alloys (Al-0.1Fe-0.1Si and Al-0.5%Fe-0.1Si). Three different amounts of Cu (0.05, 0.18 and 0.3%) were added to the low-Fe base alloy (Al-0.1Fe-0.1Si). For each composition, approximately 5 kg of materials was melted

in an electrical resistance furnace and then cast into a rectangular permanent steel mold measuring 30 x 40 x 80 mm³. Prior to casting, the melts were grain-refined by an addition of 0.015% Ti in the form of an Al-5Ti-1B master alloy. The cast ingots were homogenized at 550 °C for 6 h, followed by water quenching at ambient temperature, which gives the lowest flow stress in the dilute Al-Fe-Si alloys [15].

Cylindrical samples of 10 mm in diameter and 15 mm in height were machined from the homogenized ingots. The uniaxial hot compression tests were conducted using a Gleeble 3800 thermomechanical testing unit at strain rates of 0.01, 0.1, 1 and 10 s⁻¹ and temperatures of 400, 450, 500 and 550 °C. Specimens were heated at a rate of 2 °C/s and maintained for 120 s at the desired temperature to ensure a homogeneous temperature distribution. The specimens were deformed to a total true strain of 0.8 and then immediately water-quenched to retain the deformed microstructure.

The deformed samples were sectioned parallel to the compression axis along the centerline direction and then prepared by an argon ion-beam cross-section polisher (JEOL SM-09010) for electron backscatter diffraction (EBSD) analysis under a scanning electron microscope (JEOL JSM -6480LV). In EBSD analysis, the boundaries of grains and subgrains are defined as low angle boundaries, medium-angle boundaries and high-angle boundaries with misorientation angles of 1-5°, 5-15° and greater than 15°, respectively [16]. The step size between the scanning points was set as 1.0 μm. The line intercept method was used to measure the subgrain size in the deformed samples. To ensure statistical reliability, more than 100 subgrains were measured in each sample. All misorientation angles larger than 15° were ignored in calculating the mean misorientation

angle because they were assumed to be the original high angle grain boundaries. Thin foil samples were examined on the JEM-2100 transmission electron microscope (TEM) operated at 200 kV after electropolishing the samples in a solution of 30% nitric acid and 70% methanol at 15 V and at -22 °C

Table 5.1. Chemical compositions of experimental alloys (wt%)

Alloys	Si	Fe	Cu	Mn	Cr	Ni	Ti	Zr	V
Al-0.1Fe-0.1Si (A0)	0.10	0.12	0.002	0.001	0.001	0.007	0.016	0.0015	0.0012
Al-0.1Fe-0.1Si-0.1Mn (AM1)	0.11	0.13	0.003	0.11	0.001	0.007	0.015	0.0015	0.012
Al-0.1Fe-0.1Si-0.2Mn (AM2)	0.11	0.13	0.003	0.21	0.001	0.007	0.014	0.0016	0.012
Al-0.1Fe-0.1Si-0.05Cu (AC1)	0.10	0.12	0.051	0.001	0.001	0.007	0.016	0.0014	0.0012
Al-0.1Fe-0.1Si-0.15Cu (AC2)	0.11	0.13	0.181	0.001	0.001	0.007	0.015	0.0014	0.0013
Al-0.1Fe-0.1Si-0.31Cu (AC3)	0.11	0.13	0.31	0.00	0.001	0.007	0.015	0.0014	0.0012
Al-0.5Fe-0.1Si (B0)	0.10	0.49	0.004	0.002	0.001	0.007	0.017	0.0014	0.012
Al-0.5Fe-0.1Si-0.1Mn (BM1)	0.11	0.5	0.00	0.11	0.001	0.007	0.014	0.0014	0.012
Al-0.5Fe-0.1Si-0.2Mn (BM2)	0.11	0.5	0.00	0.22	0.001	0.007	0.015	0.0015	0.012

5.3 Results and discussion

5.3.1 Flow stress behavior

Figures 5.1 and 5.2 illustrate the series of typical true stress-true strain curves obtained during the hot compression of dilute Al-Fe-Si alloys containing various amounts of Mn and Cu, respectively. Generally, all of the alloys exhibited similar deformation behavior. In most cases, the peak flow stresses reached a plateau at a certain strain, indicating a dynamic

balance between softening and work hardening. In the case of high Z deformation conditions, the flow stress continued to increase with progressive straining, indicating that the work hardening rate was higher than the softening rate. Normally, both flow behaviors are characteristic for hot working conditions, where dynamic recovery (DRV) is the dominant softening mechanism [17, 18]. In all cases, the flow stress increased with the increasing strain rate and decreasing deformation temperature, which is in good agreement with previously reported results [19-22]. Furthermore, increasing the Mn and Cu contents enhanced the deformation resistance of dilute Al-Fe-Si alloys at all of the combinations of temperature and strain rate.

Figure 5.3 illustrates the effect of Mn and Cu additions on the flow stress at a strain of 0.8 as a function of temperature at two extremes of strain rates (0.01 and 10 s^{-1}). As shown, both Mn and Cu additions increase the flow stress of dilute Al-Fe-Si alloys significantly for a given deformation condition. However, the influence of Mn on the flow stress was more evident when the iron level remained low (0.1%). For example, in the low Fe alloy (Al-0.1Fe-0.1Si), the addition of 0.2% Mn increased the flow stress from 16 to 21 MPa (a 31% increase) at $T=400 \text{ }^\circ\text{C}$ and $\dot{\epsilon} = 0.01 \text{ s}^{-1}$ (Fig. 5.3a) and from 47 to 54 MPa (a 15% increase) at $T=400 \text{ }^\circ\text{C}$ and $\dot{\epsilon} = 10 \text{ s}^{-1}$ (Fig. 5.3b), respectively. On the other hand, in the high Fe alloy (Al-0.5Fe-0.1Si), the 0.2% Mn raised the flow stress from 18 to 22 MPa (a 22% increase) at $T=400 \text{ }^\circ\text{C}$ and $\dot{\epsilon} = 0.01 \text{ s}^{-1}$ (Fig. 5.3c) and from 51 to 55 MPa (a moderate 8% increase) at $T=400 \text{ }^\circ\text{C}$ and $\dot{\epsilon} = 10 \text{ s}^{-1}$ (Fig. 5.3d), respectively. As seen in Figs. 5.3e and f, the addition of Cu also increases the flow stress in the dilute Al-0.1Fe-0.1Si alloy. Raising the Cu content to 0.3% increased the flow stress by 19 and 13% at both deformation conditions

($T= 400\text{ }^{\circ}\text{C}$, $\dot{\epsilon} = 0.01\text{ s}^{-1}$ and $T= 400\text{ }^{\circ}\text{C}$, $\dot{\epsilon} = 10\text{ s}^{-1}$, respectively). The results indicate that the influence of Cu addition on the high temperature flow stress is rather weaker than the influence of Mn addition.

To have a better comparison between the Mn and Cu effect at a given deformation condition, the flow stress as a function of the alloying element addition (wt%) is plotted in Figure 5.4 at a temperature of $400\text{ }^{\circ}\text{C}$ and four strain rates (0.01 s^{-1} to 10 s^{-1}). It is evident that on a wt% basis, the Mn addition has a more significant impact than the copper addition on the flow stress of the Al-0.1Fe-0.1Si alloy, especially at lower strain rates (0.01 and 0.1 s^{-1}). For instance, at a given deformation condition, $T= 400\text{ }^{\circ}\text{C}$ and $\dot{\epsilon} = 0.01\text{ s}^{-1}$, the additions of 0.3% Cu and 0.2% Mn increased the flow stress in Al-0.1Fe-0.1Si alloy from 16 to 19 and 21.3 MPa, respectively. At higher strain rates (1 s^{-1} to 10 s^{-1}), both Mn and Cu have a more or less comparable effect on the flow stress.

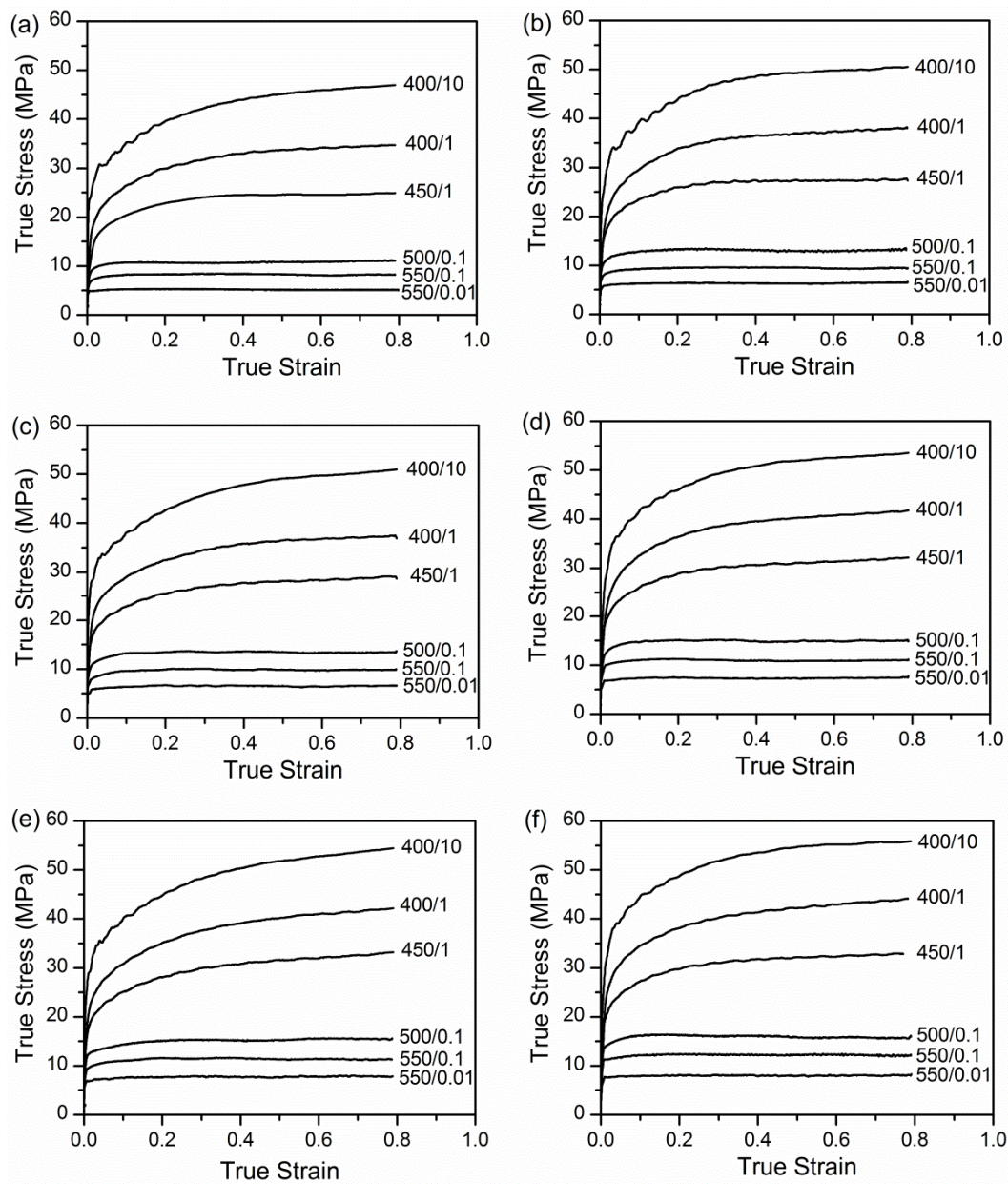


Fig.5.1. Typical true stress-true strain curves of: (a) Al-0.1Fe-0.1Si, (b) Al-0.5Fe-0.1Si, (c) Al-0.1Fe-0.1Si-0.1Mn, and (d) Al-0.5Fe-0.1Si-0.1Mn, (e) Al-0.1Fe-0.1Si-0.2Mn and (f) Al-0.5Fe-0.1Si-0.2Mn alloys.

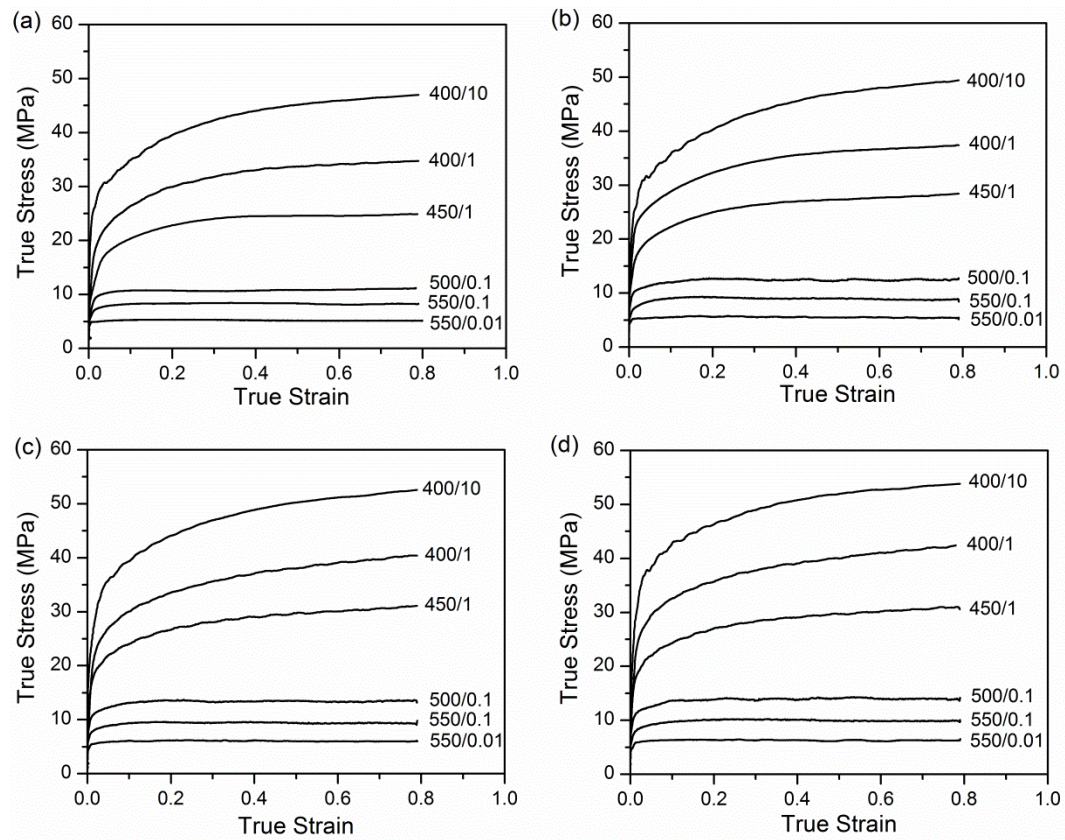


Fig.5.2. Typical true stress-true strain curves of: (a) Al-0.1Fe-0.1Si, (b) Al-0.1Fe-0.1Si-0.05Cu, (c) Al-0.1Fe-0.1Si-0.18Cu and (d) Al-0.1Fe-0.1Si-0.31Cu alloys.

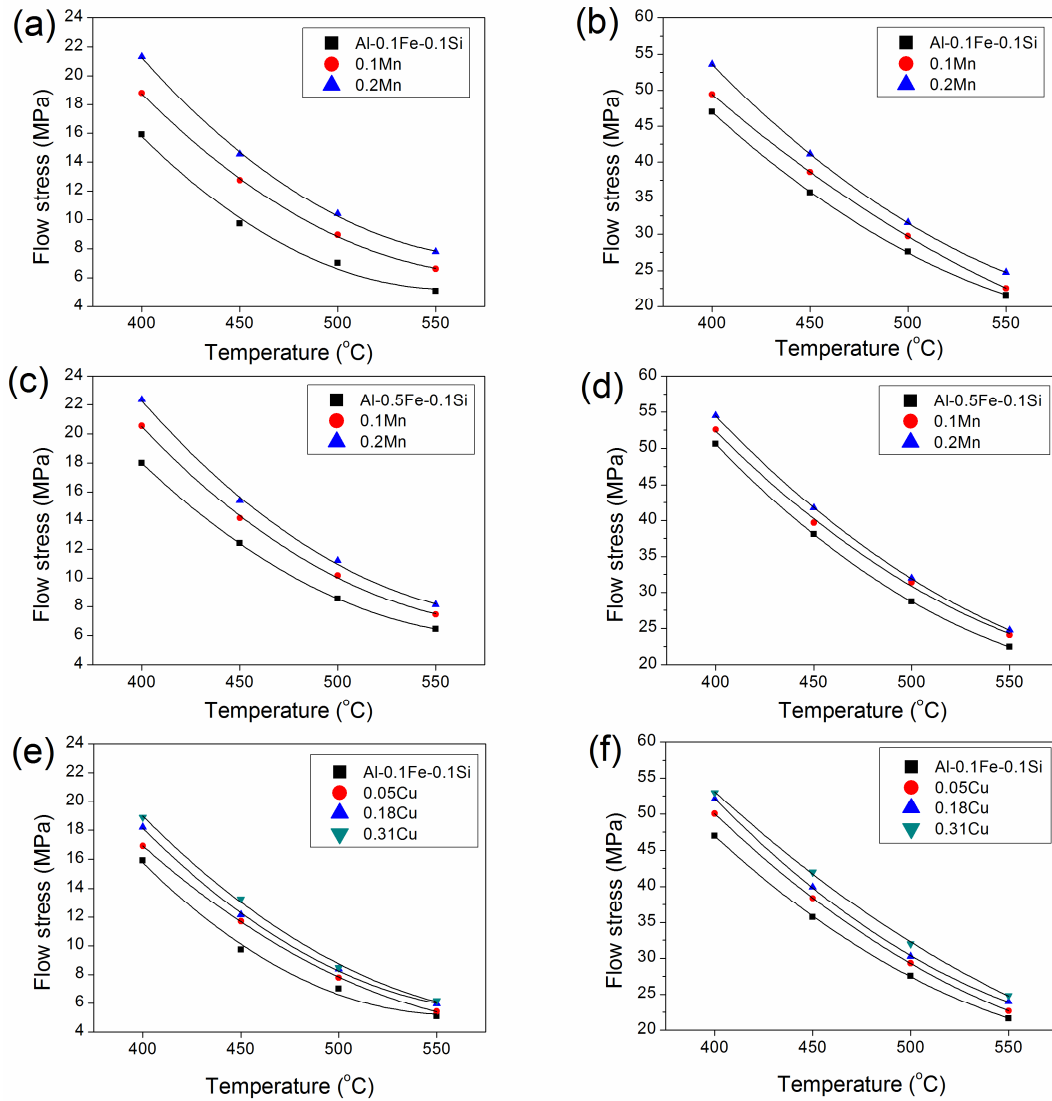


Fig.5.3. Effect of Mn and Cu on the flow stress at a strain of 0.8: (a) Al-0.1Fe-0.1Si-Mn, $\dot{\epsilon} = 0.01 \text{ s}^{-1}$, (b) Al-0.1Fe-0.1Si-Mn, $\dot{\epsilon} = 10 \text{ s}^{-1}$, (c) Al-0.5Fe-0.1Si-Mn, $\dot{\epsilon} = 0.01 \text{ s}^{-1}$, (d) Al-0.5Fe-0.1Si-Mn, $\dot{\epsilon} = 10 \text{ s}^{-1}$, (e) Al-0.1Fe-0.1Si-Cu, $\dot{\epsilon} = 0.01 \text{ s}^{-1}$ and (f) Al-0.1Fe-0.1Si-Cu, $\dot{\epsilon} = 10 \text{ s}^{-1}$.

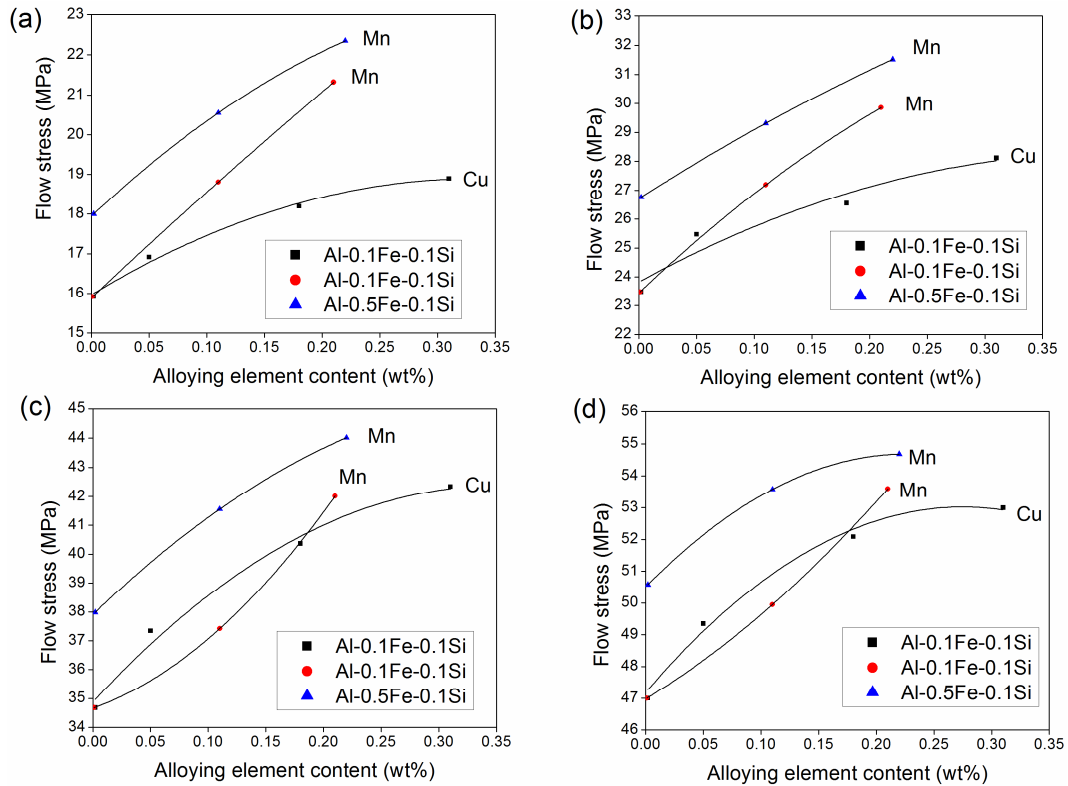


Fig.5.4. Effect of Mn and Cu contents on the flow stress at a strain of 0.8 for temperature of 400 °C, and four strain rate: (a) $\dot{\epsilon} = 0.01 \text{ s}^{-1}$, (b) $\dot{\epsilon} = 0.1 \text{ s}^{-1}$, (c) $\dot{\epsilon} = 1 \text{ s}^{-1}$ and (d) $\dot{\epsilon} = 10 \text{ s}^{-1}$.

5.3.2 Constitutive analyses

Constitutive equations are developed to demonstrate the influences of the deformation parameters on the state of flow stress. The hyperbolic sine Arrhenius type equation proposed by Sellars and McTegart [23], is widely used for constitutive analysis over wide range of temperatures and strain rates [21, 24-27]:

$$Z = A[\sinh(\alpha\sigma)]^n = \dot{\epsilon} \exp\left(\frac{Q}{RT}\right) \quad (5.1)$$

where Z is a Zener-Hollomon parameter, $\dot{\epsilon}$ is the strain rate (s^{-1}), A and n are constants, α is a stress multiplier, σ is the flow stress (MPa), Q is the activation energy for hot deformation ($kJ\ mol^{-1}$), R is the universal gas constant ($8.314\ J\ mol^{-1}\ K^{-1}$) and T is the absolute temperature (K).

The material constants and activation energy in the Eq. (5.1) could be determined for all of the alloys investigated by using the experimental data obtained from the hot compression tests at different deformation conditions. The following is the solution procedure for determining the material constants and activation energy using the experimental data obtained for AM2 (Al-0.1Fe-0.1Si-0.2Mn) alloy as an example. In this study, the value of σ is taken from the value of the flow curves at a true strain of 0.8. The value of stress multiplier α can be calculated from $\alpha = \beta/n_1$, where the value of β and n_1 obtained from the slope of the lines in the $\ln \dot{\epsilon} - \sigma$ and $\ln \dot{\epsilon} - \ln \sigma$ plots, respectively (Fig. 5.5). The mean values of β and n_1 at different temperatures were calculated to be 0.2924 and 6.41, respectively. Consequently, the value of α was defined as $\alpha = \beta/n_1 = 0.046\ MPa^{-1}$.

Differentiating Eq. (5.1) results in:

$$Q = R \left[\frac{\partial \ln \dot{\epsilon}}{\partial \ln[\sinh(\alpha\sigma)]} \right]_T \left[\frac{\partial \ln[\sinh(\alpha\sigma)]}{\partial (1/T)} \right]_{\dot{\epsilon}} = RnS \quad (5.2)$$

where R is a universal gas constant, n is the mean slope of the $\ln \dot{\epsilon}$ vs. $\partial \ln[\sinh(\alpha\sigma)]$ plot at various temperatures and S is the mean slope of the $\partial \ln[\sinh(\alpha\sigma)]$ vs. $\partial(1000/T)$ plot at different strain rates. Figure 5.6 exhibits the relationship between $\ln \dot{\epsilon} - \partial \ln[\sinh(\alpha\sigma)]$ and

$\partial \ln[\sinh(\alpha\sigma)] - \partial(1000/T)$. Therefore, the mean values of n and S can be obtained from Fig. 5.6 (a) and (b), respectively. The activation energy could then be calculated from Eq. (5.2).

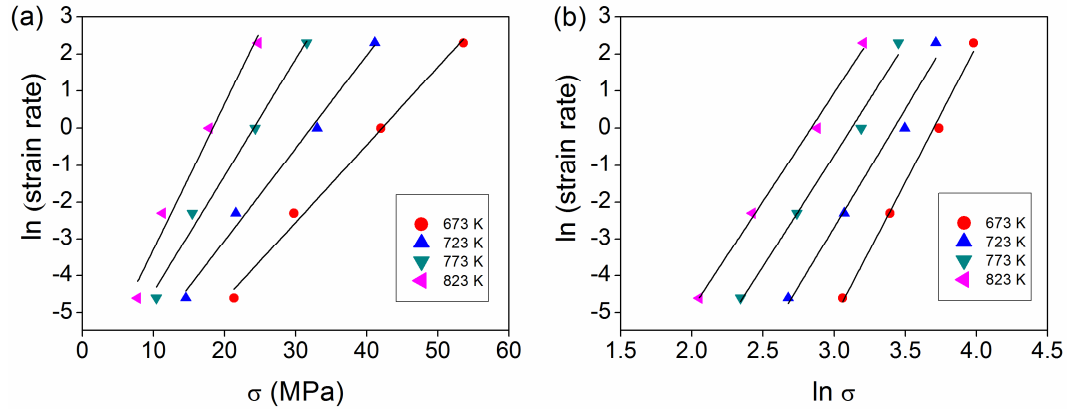


Fig.5.5. plots of (a) $\ln \dot{\epsilon} - \sigma$ and (b) $\ln \dot{\epsilon} - \ln \sigma$.

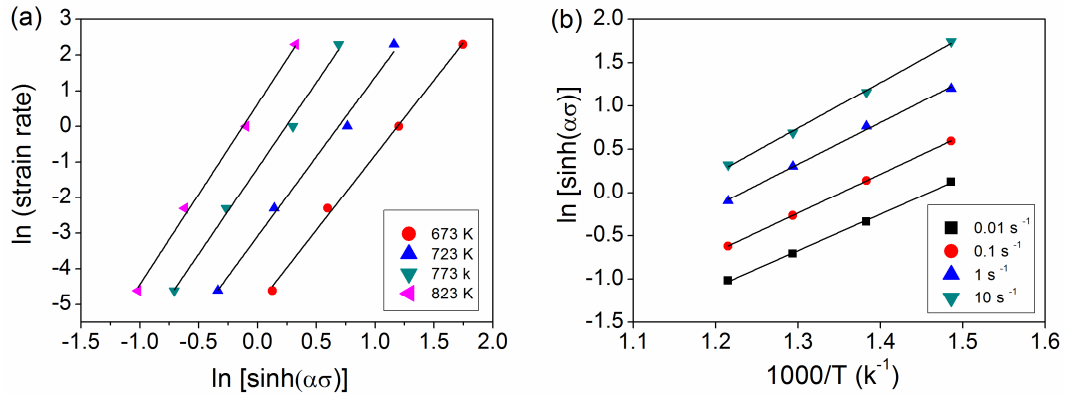


Fig.5.6. Plots of (a) $\ln \dot{\epsilon}$ vs. $\ln[\sinh(\alpha\sigma)]$ and (b) $\ln[\sinh(\alpha\sigma)]$ vs. $(1000/T)$.

Taking the natural logarithm of both sides of Eq. (5.1) results in:

$$\ln Z = \ln A + n \ln[\sinh(\alpha\sigma)] \tag{5.3}$$

The linear correlation between $\ln Z$ and $\ln[\sinh(\alpha\sigma)]$ are shown in Figure 5.7. The value of $\ln A$ could be obtained from the intercept of the plot of $\ln Z$ vs. $\ln[\sinh(\alpha\sigma)]$ plot.

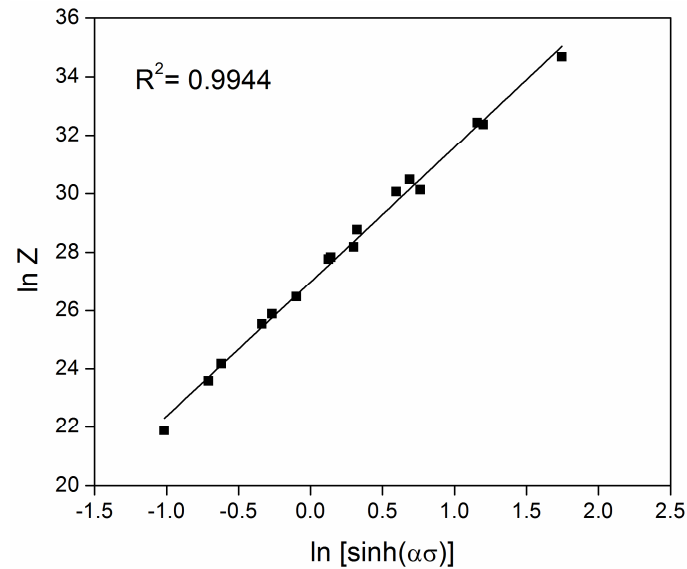


Fig.5.7. Plot of $\ln Z$ vs. $\ln[\sinh(\alpha\sigma)]$.

In a similar way, the values of material constants, α , n , A , and the activation energy, Q , were computed out for all the alloys studied. These values are presented in Table 5.2. The variation in the hot deformation activation energy as a function of alloy additions is illustrates in Figure 5.8.

Table 5.2. Values of material constants and activation energies of all the experimental alloys at strain 0.8.

Alloys	α (MP ⁻¹)	n	A(s ⁻¹)	Q (kJ/mol)
Al-0.1Fe-0.1Si (A0)	0.057	3.84	3E+10	161.22
Al-0.1Fe-0.1Si-0.1Mn (AM1)	0.050	4.36	1.62E+11	173.14
Al-0.1Fe-0.1Si-0.2Mn (AM2)	0.046	4.61	5.23E+11	181.12
Al-0.1Fe-0.1Si-0.05Cu (AC1)	0.053	3.90	4.15E+10	163.9
Al-0.1Fe-0.1Si-0.18Cu (AC2)	0.050	3.88	2.92E+10	162.51
Al-0.1Fe-0.1Si-0.31Cu (AC3)	0.048	3.92	4.93E+10	165.61
Al-0.5Fe-0.1Si (B0)	0.052	4.25	2.58E+11	176.04
Al-0.5Fe-0.1Si-0.1Mn (BM1)	0.047	4.54	4.11E+11	181.57
Al-0.5Fe-0.1Si-0.2Mn (BM2)	0.044	4.84	3.25E+12	191.71

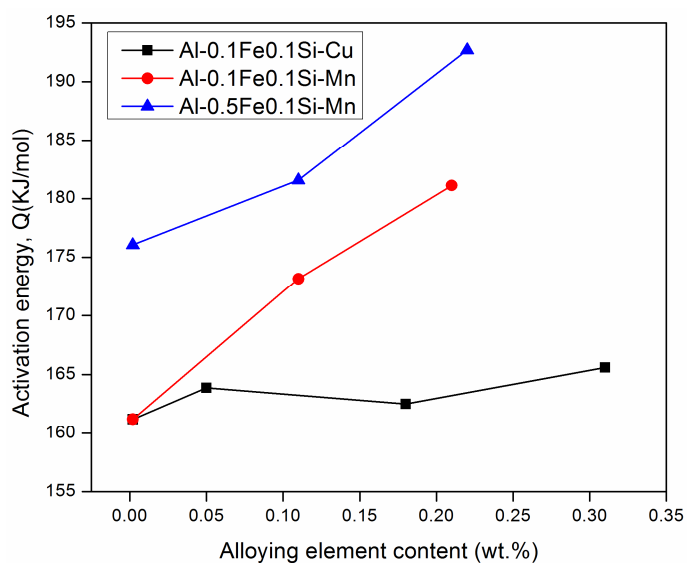


Fig.5.8. Activation energy of dilute Al-Fe-Si alloys as a function of alloying addition.

Activation energy is an important physical parameter serving as an indicator of the degree of difficulty of plastic deformation. The values of the activation energy calculated for two base alloys (i.e., Al-0.1Fe-0.1Si and Al-0.5Fe-0.1Si) are in general agreement with

those reported previously for commercially pure aluminum [10, 19, 24, 28-30]. The increases of activation energy in these two base alloys compared with the high purity pure aluminum (142 kJ/mol) [31] could be attributed to the pinning effect of iron-rich intermetallic particles in the dislocation movement. By increasing the iron content, the density of Al_3Fe intermetallic particles increases, which result on the enhanced deformation resistance and higher activation energy [10].

In addition, Mn has a significant influence on the activation energy of both low and high iron base alloys. The addition of 0.2% Mn to the Al-0.1Fe-0.1Si and Al-0.5Fe-0.1Si alloys increased their activation energies from 161 and 176 to 181 and 193 kJ/mol, respectively. In contrast, the addition of Cu only moderately increases the activation energy. The 0.31% Cu addition to the low iron base alloy (Al-0.1Fe-0.1Si) increased the activation energy from 161 to 166 kJ/mol.

5.3.3 Microstructural evolution during hot deformation

The solid solubility of Mn and Cu in aluminum are approximately 0.45% and 5.7%, respectively, at 550 °C [4, 12], and hence the additions of Mn and Cu up to 0.22% and 0.31%, respectively, in this study are expected to remain in the solid solution after homogenization at 550°C for 6 h. Studying the microstructure of the homogenized Al-0.1Fe-0.1Si-0.2Mn, Al-0.5Fe-0.1Si-0.2Mn and Al-0.1Fe-0.1Si-0.31Cu alloys also confirmed that these elements did not undergo any precipitation reactions during homogenization. The homogenized structures of all of the alloys contained uniform equiaxed grains with an average size of 110 to 125 μm and the iron-containing intermetallic

particles (i.e., Al_3Fe) distributed along aluminum dendrite boundaries [3, 15]. The phase transformation from the Al_mFe as-cast to the Al_3Fe after homogenization intermetallic phase was observed during the homogenization treatment, which is consistent with our previous work [15]. The size and distribution of the iron-containing intermetallic particles were found to remain approximately unchanged after the addition of either Mn or Cu in both low and high iron alloys. The volume fraction of iron-containing intermetallic particles was increased by increasing the iron level from approximately 0.1% (Al-0.1Fe-0.1Si) to 0.5% (Al-0.5Fe-0.1Si).

Results of TEM examination confirmed that both Mn and Cu additions do not cause the formation of any dispersoids after homogenization at 550 °C. Furthermore, Mn addition up to 0.1% did not form any dispersoids during hot deformation while some fine Fe and Mn bearing dispersoids were formed in samples containing 0.2% Mn (AM2 and BM2) by dynamic precipitation. In contrast, no dynamic precipitation was observed in the copper containing alloys. Figure 5.9 shows TEM images of the Al-0.1Fe-0.1Si-0.2Mn and Al-0.5Fe-0.1Si-0.2Mn alloys after hot deformation at $T = 400\text{ °C}$, $\dot{\epsilon} = 0.01\text{ s}^{-1}$ and $\epsilon = 0.8$. A small amount of fine dispersoid particles were found to be randomly distributed within the grains and at the grain boundaries. The energy dispersive X-ray spectrometer (TEM-EDX) analysis showed that the particles were composed of Al, Mn, Fe and Si, which most likely belonged to $\alpha\text{-Al(FeMn)Si}$ type dispersoids. It was reported [32, 33] that in the aluminum alloys containing Fe, Mn and Si, $\alpha\text{-Al(FeMn)Si}$ dispersoids are a very common type of dispersoids precipitated during heating and annealing.

Fine dispersoid particles with a sufficient number density could stabilize the substructure, retard dynamic softening processes and increase the rate of strain hardening [10, 22]. However, at high deformation temperatures (i.e., $>400^{\circ}\text{C}$) the presence of a low volume fraction of dispersoid particles has a diminished pinning effect as dislocations can climb around them [10]. As seen in Figure 5.9 (with images showing the regions of highest particle density), the dispersoid particles were relatively large and their number density was low. Therefore, in the current situation, the overall pinning effect of those dispersoids is limited because of their low number density and large interparticle spacing.

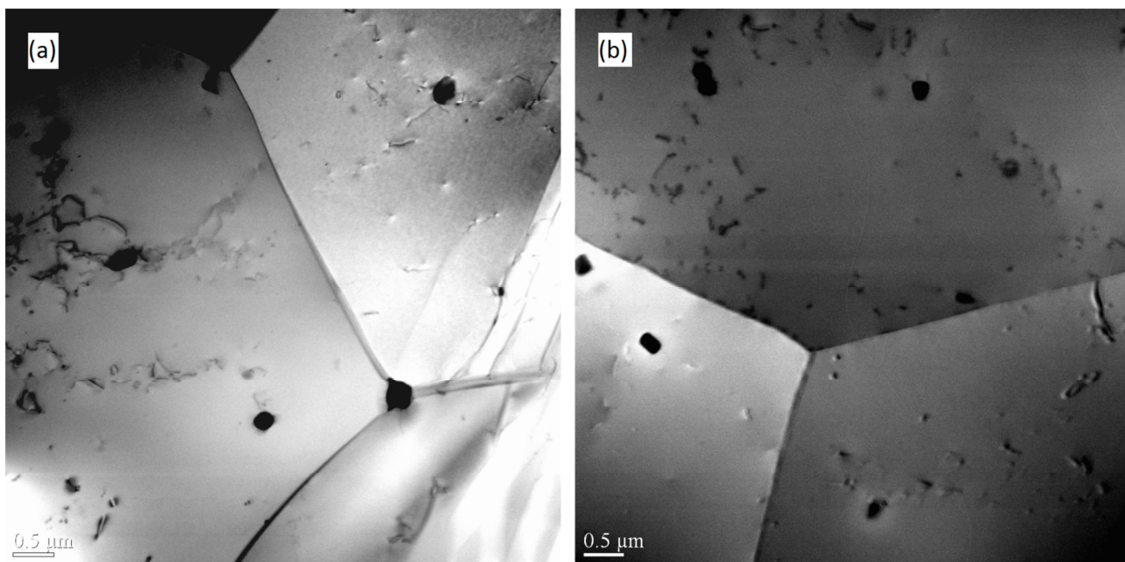


Fig.5.9. TEM microimages of the deformed samples at $T= 400^{\circ}\text{C}$ and $\dot{\epsilon} = 1 \text{ s}^{-1}$ (a) Al-0.1Fe-0.1Si-0.2Mn (b) Al-0.5Fe-0.1Si-0.2Mn

Other factors, such as grain size and second phase particles formed during solidification, may also have significant impact on the hot deformation behavior of

aluminum alloys. However, microstructural observations showed that the variation of the second phase particle distribution and grain size was negligible for the alloys studied. From the observations described above, it could be concluded that solid solution strengthening is the dominant mechanism influencing the hot deformation in the alloys with minor additions of Mn and Cu investigated in this study, and the solute content is considered as the major factor between different alloys.

To understand the effect of Mn and Cu additions on the microstructural evolution of dilute Al-Fe-Si alloys, five deformed alloy samples (Al-0.1Fe-0.1Si, Al-0.1Fe-0.1Si-0.31Cu, Al-0.1Fe-0.1Si-0.2Mn, Al-0.5Fe-0.1Si and Al-0.5Fe-0.1Si-0.2Mn deformed at 500 °C and $\dot{\epsilon} = 0.01 \text{ s}^{-1}$) were selected and analyzed by EBSD analysis. Figure 5.10 shows the orientation imaging maps of the deformed samples after compression at $T = 500^\circ\text{C}$ and $\dot{\epsilon} = 0.01 \text{ s}^{-1}$ to a strain of 0.8.

All five deformed samples had a characteristic recovered structure. DRV occurs when dislocations have sufficient mobility and the rate of dislocation removal is equal to their production, which involves dislocation annihilation and rearrangement into low and medium angle subgrain boundaries. As a result of DRV, a subgrain structure develops inside the deformed grains and the dislocation energy decreases [34, 35]. As seen in Figure 5.10, the microstructures of all five samples exhibited well defined subgrains with low and medium angle boundaries inside the elongated initial grains.

To have a quantitative analysis of the DRV rate, the deformed microstructures were characterized by subgrain size and misorientation angle, and the results are given in Table

5.3. The results revealed that both the mean boundary misorientation angle and the average subgrain size were reduced with the addition of Mn and Cu. This reduction indicates a retardation of DRV, which is consistent with the microstructural observations in Fig. 5.10. The addition of Mn resulted in a greater decrease in subgrain size and mean misorientation angle compared with an addition of Cu, which suggested a stronger restriction of dynamic recovery by the former. Furthermore, when the iron content was increased from 0.1 to 0.5%, the addition of 0.2 % Mn resulted in a lower decrease in subgrain size and mean misorientation angle, indicating a less strong effect of Mn on retardation of DRV in the Al-0.5Fe-0.1Si-0.2Mn alloy.

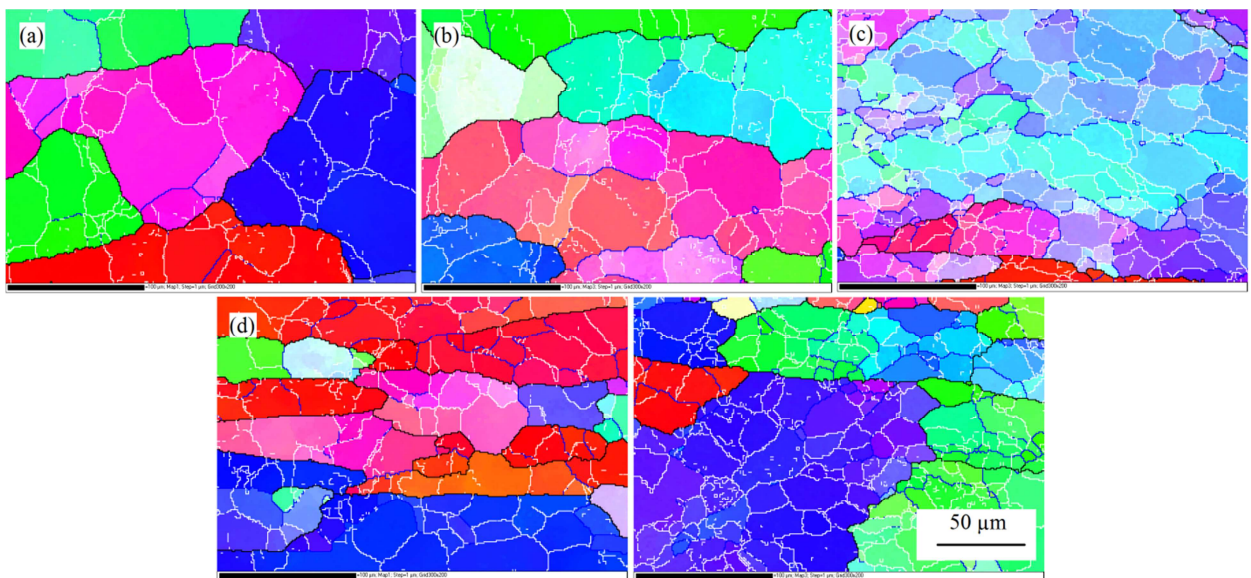


Fig.5.10. Orientation imaging maps of (a) Al-0.1Fe-0.1Si, (b) Al-0.1Fe-0.1Si-0.31Cu, (c) Al-0.1Fe-0.1Si-0.2Mn, (d) Al-0.5Fe-0.1Si and (e) Al-0.5Fe-0.1Si-0.2Mn samples deformed at 500°C and $\dot{\epsilon} = 0.01 \text{ s}^{-1}$. White lines 1-5°, blue lines 5-15° and black lines > 15°.

Table 5.3. Subgrain size and mean misorientation angle of deformed samples at $T = 500^{\circ}\text{C}$ and $\dot{\epsilon} = 0.01 \text{ s}^{-1}$ to strain of 0.8.

Alloy	Subgrain size (μm)	Mean misorientation angle
Al-0.1Fe-0.1Si (A0)	16.55	4.73
Al-0.1Fe-0.1Si-0.31Cu (AC3)	15.06	3.97
Al-0.1Fe-0.1Si-0.2Mn (AM2)	12.03	3.88
Al-0.5Fe-0.1Si (B0)	13.72	4.02
Al-0.5Fe-0.1Si-0.2Mn (BM2)	11.54	3.28

5.3.4 Discussion

The effects of Mn and Cu additions on the hot deformation behavior of dilute Al-Fe-Si alloys were investigated. In terms of microstructure, no additional precipitation was produced when up to 0.31% Cu was added, whereas adding 0.2% Mn resulted in dynamic precipitation of a low volume fraction of α -Al(FeMn)Si dispersoids. However, the pinning effect of these dispersoids is very limited due to their low density and relatively large interparticle spacing (as shown in Fig. 5.9) [10]. Hence, solid solution strengthening could be considered as the dominant mechanism in these alloys.

Small additions of Mn (0.1 and 0.2%) increased the flow stress of the Al-Fe-Si alloys significantly. Constitutive analysis indicated that Mn has a significant influence on the activation energy of both low and high iron containing alloys (Fig. 5.8). Conversely, the Cu addition is found to have a lower effect on the flow stress compared to Mn (Figs 5.3 and 5.4), and the values of the activation energy for the Cu containing alloys only increased slightly with increasing Cu content (Fig. 5.8).

The stronger effects of Mn addition compare with Cu addition can be interpreted as being due to the higher relative differences in atom size and shear modulus of Mn with aluminum than those for Cu with aluminum. However, in the case of atom size difference, it is the Cu atoms that have the larger size difference compared with Mn (Table. 5.4), which results in larger interaction forces between dislocations and Cu atoms than between dislocations and Mn atoms [4, 12]. Spittle et al. [12] claimed that Cu has a stronger impact than Mn on the hot flow stress of pure aluminum due to the larger difference in atomic radii between Cu and Al compared with the difference between Mn and Al. Conversely, as seen in Table 5.4, the modulus misfit of Mn with aluminum is higher than that of Cu with aluminum. This may explain the observed difference between Mn and Cu effects, but it is difficult to clearly distinguish the effects of both elements on hot deformation behavior based on these two traditional criteria. It was suggested by Ryen et. al. [4] that despite the larger atomic radius differences between Mg and Al compare with Mn and Al, for the commercially pure aluminum grades, Mn has a stronger hardening effect per atom than Mg because of the clustering effect between Mn and trace elements in solid solution. However, this theory cannot explain the more significant impact of Mn on the flow stress at lower strain rates.

The stronger effect of the Mn atoms compared with the Cu atoms in the high temperature flow behavior of Al-0.12Fe-Si alloy, which is demonstrated in this study, may be explained by the dislocation climb model proposed by Sherby et.al. [14, 36]. This model involves solute atom diffusion as the rate-controlling deformation process. Both solute atoms (Mn or Cu) can segregate at subgrain boundaries during the early stages of hot

deformation. In this step, the stress field from the subgrain boundary dislocations is balanced by the stress field from the pile-up dislocations under the applied shear stress. Then, the opposing stress fields from subgrain boundaries and from pile-up dislocation are cyclically relaxed by the diffusion of solute atoms in the subgrain boundary. The release of energy leads to the unpinning of the lead dislocation from the pile-up and allows the dislocation to glide past the boundary, which results in the deformation of the alloy [14, 36]. The solute-diffusion-controlled hot deformation mechanism suggests that the deformation resistance of dilute solid solution aluminum alloys is inversely proportional to the diffusion coefficient of the solute atoms in the aluminum matrix [36].

Figure 5.11 shows the diffusion coefficient of Mn and Cu in aluminum as a function of temperature. As shown, Mn has a much lower diffusion rate than that for aluminum self-diffusion, while the Cu diffusion rate in aluminum is much close to that for aluminum self-diffusion [31].

Table 5. 4. Atomic radius and shear modulus of alloying elements of aluminum [12].

Element	Atomic Radius $r(\text{Å})$	Shear modulus G (GPa)
Al	1.43	26.2
Cu	1.28	48.3
Mn	1.30	66.8

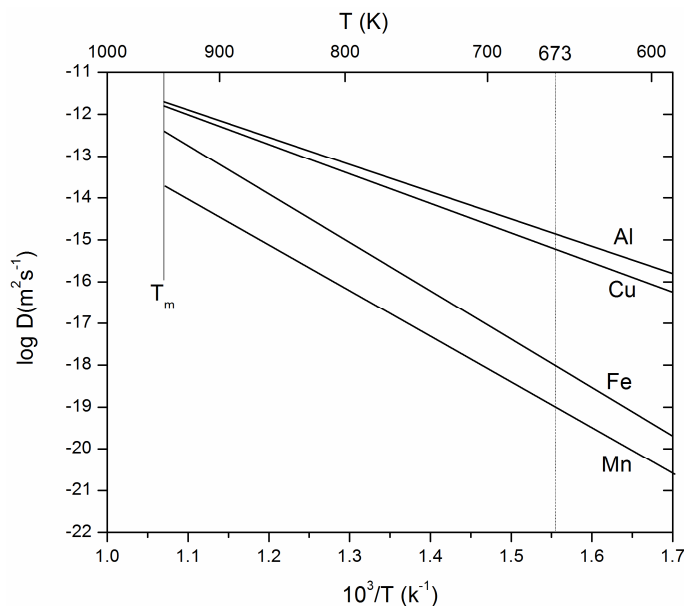


Fig.5.11. The diffusion rate of various solutes in aluminum as a function of reciprocal temperature [31].

In the case of deformation of Mn containing alloys, due to the low diffusion rate of Mn atoms, the pile-up dislocations could not easily pass through the subgrain boundaries, and their movement was strongly hindered at the subgrain boundaries. This hindering of movement led to an enhanced dislocation multiplication rate, which acted as a barrier to further dislocation movement and resulted in a higher work hardening rate [14]. Furthermore, due to the presence of Mn solutes, dynamic recovery was restrained, which led to a finer subgrain structure and smaller misorientation angle compared with the base alloys as observed in Figures 5.10 (c) and (e) and Table 5.3. This fine substructure was stabilized by the Mn solutes, which acted as effective barriers to dislocation motion [14, 36]. Hence, the flow stress of Al-Fe-Si-Mn alloys increases significantly due to enhanced work hardening, restrained dynamic recovery and an increased subgrain strengthening rate.

The alloys Al-0.1Fe-0.1Si-0.2Mn and Al-0.5Fe-0.1Si-0.2Mn, which contain 0.2% Mn, had the activation energies for hot deformation of 181 and 193 kJ/mol, respectively, and these values are close to the activation energy for Mn solute diffusion in aluminum of 203 kJ/mol [31]. These results suggest that the hot deformation process involved manganese solute diffusion acted as the deformation rate-controlling mechanism. Similar results have been observed during the creep processing of aluminum alloys containing 0.054% Fe and 1.0% Mn [14, 36].

In the case of Cu addition, due to the small difference between the diffusivity of Cu in aluminum and aluminum self-diffusion [31], Cu containing alloys exhibited a weaker solute effect at high deformation temperatures compared with the Mn containing alloys. Furthermore, the activation energy for Cu solute diffusion in aluminum is similar to the activation energy for aluminum self-diffusion (142 kJ/mol) [31], indicating a similar energy barrier to dislocation motion for the pure aluminum and solute Cu containing aluminum alloys. The comparable values of activation energies for hot deformation between Cu containing alloys and the base alloy also can give support for the solute diffusion rate-controlling mechanism. In terms of the microstructural evolution of Al-Fe-Si-Cu alloys, due to a still lower diffusion rate of copper in aluminum than the aluminum self-diffusion, the pile-up dislocations had some degree of difficulty passing through the subgrain boundaries compared with the base alloy, resulting in a decreased level of dynamic recovery during hot compressive deformation. Moreover, Cu solutes in the aluminum matrix retarded the dislocation motion due to the solute drag effect [34, 37, 38]. By increasing the Cu content, the increased amount of solute atoms produced a stronger

pinning effect, leading to a lower rate of DRV and consequently a moderate increase in flow stress.

The more remarkable impact of Mn addition on the flow stress than Cu addition, particularly at low strain rates (i.e., 0.01 s^{-1}) as shown in Fig. 5.4, also can be explained by the dislocation climb model. Subgrain boundaries developed during hot deformation of aluminum alloys are a natural barrier to dislocation motion and plastic flow. Previously, McQueen et al. [35] and Jonas et al. [36] showed that the flow stress of a specific alloy at a given deformation condition is a function of the subgrain size. In the early stages of deformation, clean subgrain boundaries are created in the deformed grains that are free of solute atoms. In this condition, aluminum diffusion controls the deformation rate. Then, solute atoms start to be absorbed by the core of the edge dislocations within the boundaries. Therefore, solute atom diffusion rates become the dominant controlling mechanism. When the strain rate is low, solute atoms have enough time to segregate in the subgrain boundaries, and consequently they have a more significant influence on controlling the deformation rate. By increasing the strain rate toward 10 s^{-1} , the number of solute atoms that can segregate on the subgrain boundaries is largely reduced due to limited time, which leads to the diminished effect of the solute diffusion rate on the flow stress of dilute alloys. Therefore, both alloys containing Mn solute and alloys containing Cu solute exhibit more comparable values of flow stress at high strain rate conditions (Fig 5.4 (b)).

5.4 Conclusions

In this study, the effects of Mn and Cu additions on the hot workability of dilute Al-Fe-Si alloys were investigated. The following conclusions can be drawn:

1. Additions of Mn and Cu increase the flow stress of dilute Al-Fe-Si alloys for a given deformation condition. On a wt% basis, the addition of Mn has a more significant impact on the flow stress compared with that addition of Cu.
2. The activation energies for hot deformation increased from 161 and 176 for low-Fe and high-Fe base alloys to 181 and 192 kJ/mol, respectively, for the alloys containing 0.2% Mn, while the addition of Cu up to 0.31% to the low-Fe base alloy raised the activation energy only slightly from 161 to 166 kJ/mol.
3. The solute-diffusion acted as the deformation rate-controlling mechanism in these dilute aluminum alloys. The hot deformation resistance is inversely proportional to the diffusion coefficient of the solute atoms and increase with an increasing amount of the Mn and Cu solutes in the aluminum.
4. Additions of Mn and Cu promote the retardation of the dynamic recovery, which leads to a finer subgrain structure and a smaller misorientation angle after hot deformation. The addition of Mn results in a greater decrease in subgrain size and mean misorientation angle compared with the addition of Cu.

References

- [1] J.R. Davis, Aluminum and aluminum alloys. Materials Park, OH, ASM International, 1993, pp. 59-87.

- [2] J.G. Kaufman, Introduction to aluminum alloys and tempers. Materials Park, OH, ASM International, 2000, pp. 87-118.
- [3] M. Shakiba, N. Parson, X.-G. Chen, Effect of iron and silicon content on the high-temperature flow behavior of dilute Al-Fe-Si alloys, *J. Mater. Eng. Perform.*, 2014, DOI: 10.1007/s11665-014-1302-3.
- [4] Ø. Ryen, B. Holmedal, O. Nijs, E. Nes, E. Sjölander, H.-E. Ekström, Strengthening mechanisms in solid solution aluminum alloys, *Metall. Mat. Trans. A*, 2006, 37, pp.1999-2006.
- [5] T. Furu, R. Rsund, E. Nes, Substructure evolution during different hot deformation processes of commercial non-heat treatable aluminium alloys, *Mater. Sci. Eng. A*, 1996, 214, pp.122-32.
- [6] M.M.R. Jaradeh, T. Carlberg, Solidification Studies of 3003 Aluminium Alloys with Cu and Zr Additions, *J. Mater. Sci. Technol.*, 2011, 27, pp.615-27.
- [7] R. Benedictus, S.D. Meijers, A.J.W. And, J.H.W.D. Wit, Influence of alloying additions on corrosion behavior of aluminum brazing sheet, In: Sato T, editor, 6th International Conference on Aluminum Alloys, ICAA-6. Japan: The Japan Institute of Light Metals; 1998. pp. 1577-82.
- [8] P. Haasen. Physical metallurgy. In: R.W. Chan, P. Haasen, editors, Physical metallurgy. 4th ed. ed: Elsevier ltd.; 1996, pp. 2009-68.
- [9] R.L. Fleischer, W.R. Hibbard, The relation between the structure and mechanical properties of metals. London: H.M. Stationery Off.; 1963. pp. 262-94.
- [10] H.J. Mcqueen, S. Spigarelli, M.E. Kassner, E. Evagelista, Hot deformation and processing of aluminum alloys. Florida, CRC Press, 2011.
- [11] C.O. Schmidt, Modelling the solute strengthening-deformation strengthening interaction, *Int. J. Eng. Sci.*, 1984, 22, pp.1055-63.
- [12] M. Spittel, T. Spittel. Flow stress of light metal alloys. In:H. Warlimont , editor, Part 2: Non-ferrous Alloys - Light Metals: Springer Berlin Heidelberg; 2011, pp. 19-53.
- [13] B. Verlinden, J. Driver, I. Samajdar, R.D. Doherty, Thermo-mechanical processing of metallic materials. Oxford, UK, Elsevier, 2007.
- [14] O.D. Sherby, A. Goldberg, O.A. Ruano, Solute-diffusion-controlled dislocation creep in pure aluminium containing 0.026 at.% Fe, *Philos. Mag.*, 2004, 84, pp.2417-34.
- [15] M. Shakiba, N. Parson, X.-G.Chen, Effect of homogenization treatment and silicon content on the microstructure and hot workability of dilute Al-Fe-Si alloys, *Mater. Sci. Eng. A*, 2014, 619, pp.180-9.
- [16] F.J. Humphreys, Review Grain and subgrain characterisation by electron backscatter diffraction, *J. Mater. Sci.*, 2001, 36, pp.3833-54.

- [17] H.J. McQueen, W. Blum, Dynamic recovery: sufficient mechanism in the hot deformation of Al, *Mater. Sci. Eng. A*, 2000, 290, pp.95-107.
- [18] H.J. McQueen, Metal forming: Industrial, mechanical computational and microstructural, *J. Mater. Process. Technol.*, 1993, 37, pp.3-36.
- [19] H.J. McQueen, E. Evangelista, N. Jin, M.E. Kassner, Energy dissipation efficiency in aluminum dependent on monotonic flow curves and dynamic recovery, *Metall. Mater. Trans. A*, 1995, 26, pp.1757-66.
- [20] H.R. Rezaei Ashtiani, M.H. Parsa, H. Bisadi, Constitutive equations for elevated temperature flow behavior of commercial purity aluminum, *Mater. Sci. Eng. A*, 2012, 545, pp.61-7.
- [21] S. Banerjee, P.S. Robi, A. Srinivasan, L. Praveen Kumar, High temperature deformation behavior of Al–Cu–Mg alloys micro-alloyed with Sn, *Mater. Sci. Eng. A*, 2010, 527, pp.2498-503.
- [22] H. Zhang, E.V. Konopleva, H.J. McQueen, Effects of Mn dispersoid on hot working of Al–1Mn, *Mater. Sci. Eng. A*, 2001, 319–321, pp.711-5.
- [23] C.M. Sellars, W.J. Mctegart, La relation entre la résistance et la structure dans la deformation à chaud, *Mem. Sci. Rev. Met.*, 1966, 63, pp.731-46.
- [24] H.J. McQueen, N.D. Ryan, Constitutive analysis in hot working, *Mater. Sci. Eng. A*, 2002, 322, pp.43-63.
- [25] Y.C. Lin, Y.-C. Xia, X.-M. Chen, M.-S. Chen, Constitutive descriptions for hot compressed 2124-T851 aluminum alloy over a wide range of temperature and strain rate, *Comput. Mater. Sci.*, 2010, 50, pp.227-33.
- [26] F.A. Slooff, J. Zhou, J. Duszczyk, L. Katgerman, Constitutive analysis of wrought magnesium alloy Mg–Al4–Zn1, *Scripta Mater.*, 2007, 57, pp.759-62.
- [27] S.B. Brown, K.H. Kim, L. Anand, An internal variable constitutive model for hot working of metals, *Int. J. Plast.*, 1989, 5, pp.95-130.
- [28] H. McQueen, J. Hockett, Microstructures of aluminum compressed at various rates and temperatures, *Metall. Trans.*, 1970, 1, pp.2997-3004.
- [29] C.M. Sellar, W.J.M. Tegart, Hot workability, *Int. Met. Rev.*, 1972, 17, pp.1-24.
- [30] H.J. McQueen, P. Sakaris, Influence of stress multiplier in SINH equation on constitutive constants for Al alloys with Mg and dispersoids In: L. Arnberg, E. Nes, O. Lohne, N. Ryum, editors, *Aluminum alloys: Their Physical and Mechanical Properties - Proceedings ICAA3*. Trondheim, Norway, pp. 179-84.
- [31] G. Neumann, C. Tuijn, Self-diffusion and impurity diffusion in pure metals: Handbook of experimental data, Elsevier Ltd., 2009.

- [32] Yj Li, E. Al, Proceedings of 12th international conference on aluminum alloys., In: Proceedings of 12th international conference on aluminum alloys, Yokohama, Japan, Institute of Light Metals, 2010.
- [33] Q. Du, W.J. Poole, M.A. Wells, N.C. Parson, Microstructure evolution during homogenization of Al–Mn–Fe–Si alloys: Modeling and experimental results, *Acta Mater.*, 2013, 61, pp.4961-73.
- [34] F.J. Humphreys, M. Hatherly, Recrystallization and related annealing phenomena, Second ed. Oxford, Elsevier Ltd., 2004.
- [35] H. Zhang, F. Jiang, X. Shang, L. Li, Flow stress and microstructural evolution of the horizontal continuous casting Al–0.96Mn–0.38Si–0.18Fe alloy during hot compression, *Mater. Sci. Eng. A*, 2013, 571, pp.25-32.
- [36] O.D. Sherby, O.A. Ruano, Rate-controlling processes in creep of subgrain containing aluminum materials, *Mater. Sci. Eng. A*, 2005, 410–411, pp.8-11.
- [37] R. Le Gall, J.J. Jonas, Solute drag effects during the dynamic recrystallization of nickel, *Acta Mater.*, 1999, 47, pp.4365-74.
- [38] O.D. Sherby, E.M. Taleff, Influence of grain size, solute atoms and second-phase particles on creep behavior of polycrystalline solids, *Mater. Sci. Eng. A*, 2002, 322, pp.89-99.

CHAPTER 6

MODELING THE EFFECTS OF CU CONTENT AND DEFORMATION VARIABLES ON THE HIGH-TEMPERATURE FLOW BEHAVIOR OF AL-FE-SI ALLOYS USING AN ARTIFICIAL NEURAL NETWORK

CHAPTER 6

**MODELING THE EFFECTS OF CU CONTENT AND
DEFORMATION VARIABLES ON THE HIGH-TEMPERATURE
FLOW BEHAVIOR OF AL-FE-SI ALLOYS USING AN ARTIFICIAL
NEURAL NETWORK**

Abstract

The hot deformation behavior of Al-0.12Fe-0.1Si alloys with varied amounts of Cu (0.002-0.31 wt%) was investigated by uniaxial compression tests conducted at different temperatures (400-550 °C) and strain rates (0.01-10 s⁻¹). The results demonstrated that flow stress decreased with increasing deformation temperature and decreasing strain rate, while flow stress increased with increasing Cu content for all deformation conditions studied due to the solute drag effect. Based on the experimental data, an artificial neural network model was developed to study the relationship between chemical composition, deformation variables and high-temperature flow behavior. A three-layer feed-forward back-propagation artificial neural network with 20 neurons in a hidden layer was established in this study. The input parameters were Cu content, temperature, strain rate and strain, while the flow stress was the output. The performance of the proposed model was evaluated using various standard statistical parameters. An excellent agreement between experimental and predicted

results was obtained. Sensitivity analysis indicated that the strain rate is the most important parameter, while the Cu content exhibited a modest but significant influence on the flow stress. The ANN model proposed in this study can accurately predict the hot deformation behavior of Al-0.12Fe-0.1Si alloys.

6.1 Introduction

1xxx series wrought aluminum alloys are used in a wide range of applications and product forms, such as foil and strips for packaging and heat-exchanger tubing, cable sheathing and fin stock, where excellent formability, corrosion resistance and electrical and thermal conductivity are required [1, 2]. Typically, the levels of iron and silicon in a specific alloy are controlled to provide the required performance characteristics, such as strength, formability or corrosion resistance, which resulting in many commercial variants within a given AA specification. The effects of iron and silicon levels on hot workability in 1xxx alloys were reported in our previous work [3]. Increasing both iron and silicon contents generally increases the high-temperature flow stress, which can negatively impact the hot workability [3]. For example, the extrusion speed and corresponding productivity of thin-wall tubing can be reduced. Thus, there is a trade-off between room temperature mechanical properties and hot workability. An alternate approach to increase room temperature strength is to add copper for solution strengthening, as is the case in the widely utilized AA1100 alloys. In the current work, the impact of copper content on hot workability is assessed with the long-term view of optimizing 1xxx alloy design for both strength and hot processability.

The flow behavior of aluminum alloys during hot deformation is complex. The work hardening and dynamic softening mechanisms are both significantly affected by a number of factors, such as chemical composition, forming temperature, strain rate and strain [4, 5]. Therefore, prediction of the hot deformation behavior of metals and alloys under various thermomechanical conditions is of great technical interest. Constitutive models are extensively employed to describe high-temperature flow behavior. These models are either analytical [6-8] or phenomenological [9-11]. Analytical constitutive models are based on the physical aspects of a material's behavior and require comprehensive understanding of the underlying mechanisms that control the material's deformation. In addition, there are many independent parameters in analytical constitutive equations that require experimental determination. These features make this type of model difficult to apply. Phenomenological constitutive models serve as the classical approach for modeling forming processes of materials at elevated temperatures. These models describe the flow behavior based upon empirical observations using mathematical functions to consider the influence of deformation variables on the flow stress. Phenomenological models often lack physical background and are typically restricted to certain processing domains where a specific deformation mechanism operates. In the approaches described above, material constants are defined by experimental results via regression analysis on the basis of analytical or phenomenological constitutive equations. As the response of deformation behavior at high temperatures is highly nonlinear, accurate prediction of the flow stress by these methods is difficult, and the applicable range of these models is limited.

In recent years, artificial neural networks (ANNs) have provided a fundamentally different approach for material modeling and material processing control techniques [12]. The most important advantage of ANNs is that they do not require postulation of a mathematical model at the outset or the identification of its parameters. ANNs learn from examples and recognize patterns in a series of input and output data without the need for any prior assumptions about their nature and interrelations [13, 14]. Recently ANNs have been successfully applied to model the high-temperature flow behavior of stainless steels [14], aluminum alloys [15, 16], magnesium alloys [17], titanium alloys [18, 19] and Al-base metal matrix composites [20]. However, to date, no ANN model has been developed to simultaneously include the effect of both chemical composition and deformation variables in aluminum alloys.

In the present study, the capability of the ANN approach to predict the high-temperature flow behavior of Al-0.12Fe-0.1Si-Cu alloys was examined as a function of chemical composition and process parameters. An ANN model has been proposed to predict the flow behavior of Al-0.12Fe-0.1Si alloys with various levels of Cu addition (0.002-0.31 wt%) under different deformation conditions. Sensitivity analysis was carried out to quantify the relative importance of Cu addition and individual deformation variables on the flow stress.

6.2 Experimental procedures

Al-0.12Fe-0.1Si alloys with different Cu contents ranging from 0.002 to 0.31% were investigated (all alloy compositions in this study are given in wt% unless otherwise

indicated). Materials were prepared from commercially pure aluminum (99.7%), Al-50%Si and Al-50%Cu master alloys. Table 6.1 provides the chemical compositions of the experimental alloys used. For each composition, approximately 3 kg of material was melted in an electrical resistance furnace and then cast into a rectangular permanent steel mold. Prior to casting, the melts were grain-refined by the addition of 0.015% Ti in the form of an Al-5Ti-1B master alloy. The cast ingots of these alloys were homogenized at 550 °C for 6 h, and then water quenched to room temperature.

Table 6.1. Chemical compositions of alloys (wt%)

Alloys	Si	Fe	Cu	Mn	Cr	Ni	Ti	Co	Zr	V
Base alloy	0.10	0.12	0.002	0.001	0.001	0.007	0.016	0.0003	0.0015	0.012
Al-0.12Fe-0.1Si- 0.05Cu	0.10	0.12	0.051	0.001	0.001	0.007	0.016	0.0003	0.0014	0.012
Al-0.12Fe-0.1Si- 0.18Cu	0.11	0.13	0.181	0.001	0.001	0.007	0.015	0.0003	0.0014	0.013
Al-0.12Fe-0.1Si- 0.31Cu	0.11	0.13	0.31	0.00	0.001	0.007	0.015	0.0003	0.0014	0.012

Cylindrical samples (10 mm diameter and 15 mm height) were machined from the homogenized ingots. Uniaxial hot compression tests were conducted using a Gleeble 3800 thermomechanical testing unit at strain rates of 0.01, 0.1, 1 and 10 s⁻¹ and temperatures of 400, 450, 500 and 550 °C. Specimens were deformed to a total true strain of 0.8 and then immediately water-quenched to room temperature.

6.3 Results and discussion

6.3.1 Effect of Cu content on flow stress behavior

Hot compression tests of four Al-0.12Fe-0.1Si alloys with various levels of Cu were conducted at different strain rates (0.01 to 10 s⁻¹) and temperatures (400 to 550 °C). Figure

6.1 illustrates the resulting series of true stress-true strain curves obtained during hot deformation. In general, the peak flow stress was followed by a steady state region. However, in some cases, the flow stress continued to increase until the end of straining. The former case occurs when dynamic softening is in balance with work hardening, while the latter phenomenon is indicative of work hardening being stronger than dynamic softening during deformation. Both flow behaviors are normal characteristics of hot working where dynamic recovery (DRV) is the dominant softening mechanism [21, 22]. Flow stress increased with increasing strain rate and decreasing deformation temperature for all alloys studied, which is in agreement with previously reported results [5, 23, 24]. Furthermore, flow stress significantly increased with increasing Cu content.

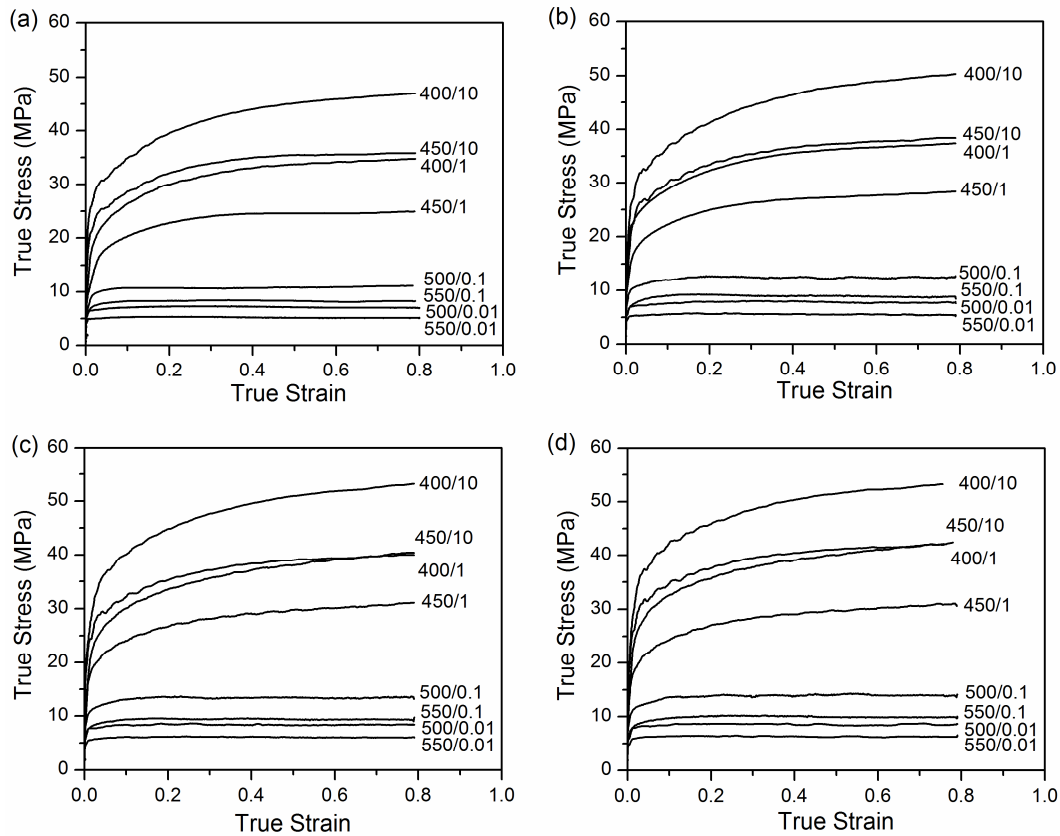


Fig. 6.1. Typical true stress-true strain curves of: (a) Base alloy, (b) 0.05% Cu, (c) 0.18% Cu and (d) 0.31% Cu.

Figure 6.2 presents the evolution of flow stress with varying amounts of Cu at a true strain of 0.4 as a function of temperature at different strain rates. It is evident that increasing the Cu content increases the flow stress over the applied range of deformation conditions. For example, at a given deformation condition ($T = 400\text{ }^{\circ}\text{C}$, $\dot{\epsilon} = 1\text{ s}^{-1}$), increasing the Cu level from 0.002% to 0.05%, 0.18%, and 0.31% increased the flow stress from 33 to 35.5, 37 and 39 MPa, respectively. These results indicate that the addition of Cu gradually enhances the deformation resistance of the dilute Al-Fe-Si alloy. As Cu has a relatively high solid solubility in aluminum (5.7% at 548 $^{\circ}\text{C}$ [25]), all of the added Cu up to 0.31% is

expected to be in the solid solution after homogenization and at the deformation temperature. Microstructural examination of the Cu-containing deformed samples confirmed that Cu did not form any precipitates or dispersoids and that all of the added Cu remained in solid solution. The Cu solute atoms interact with mobile dislocations and retard dynamic recovery, which leads to significant increases in flow stress during hot deformation [26, 27].

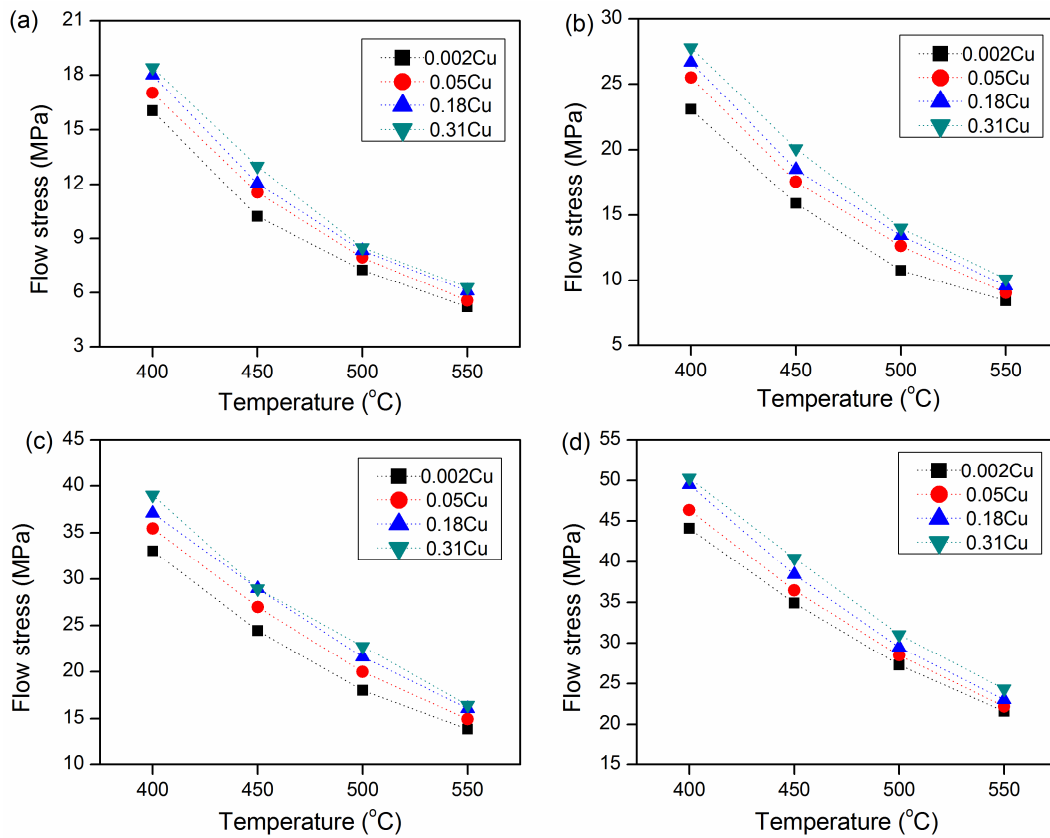


Fig. 6.2. Effect of Cu content on flow stress of Al-0.12Fe-0.1Si alloy at strain of 0.4; (a) $\dot{\epsilon} = 0.01 \text{ s}^{-1}$, (b) $\dot{\epsilon} = 0.1 \text{ s}^{-1}$, (c) $\dot{\epsilon} = 1 \text{ s}^{-1}$ and (d) $\dot{\epsilon} = 10 \text{ s}^{-1}$.

6.3.2 Development of artificial neural network model

A multilayer perceptron (MLP) based feed-forward artificial neural network with a back-propagation (BP) learning algorithm was employed to study the high-temperature flow behavior of Al-0.12Fe-0.1Si-Cu alloys. A general scheme of the three layer network with one hidden layer is given in Figure 6.3.

A differentiable logistic sigmoid function, given by Equation 1, was employed as the activation function in the present model:

$$F(x) = \frac{1}{1 + \exp(-x)} \quad (6.1)$$

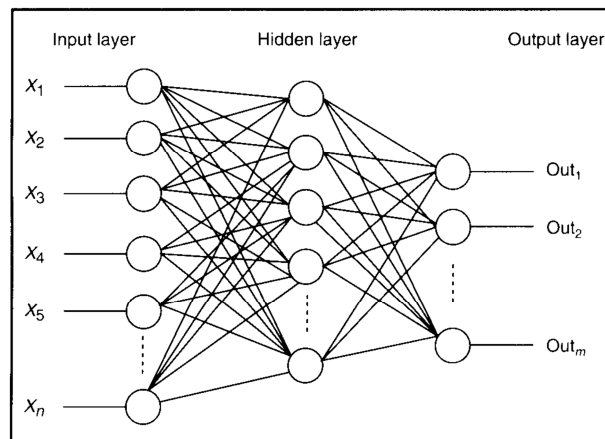


Fig. 6.3. The architecture of the ANN model.

In this study, the input parameters of the neural network are: Cu content, strain (ϵ), temperature (T) and strain rate ($\dot{\epsilon}$). The output is flow stress (σ). A total of 960

experimental data points were selected from the true stress–true strain curves (with an interval of 0.05 between true strains of 0.05 and 0.75) and were employed to train and test the ANN model. To ensure the learning efficiency of the algorithm and prevent a specific factor from dominating learning for the model, both input and output data were normalized within the range of 0-1. The following equation is widely utilized for unification [15, 28].

$$X' = 0.1 + 0.8 \times \left(\frac{X - X_{\min}}{X_{\max} - X_{\min}} \right) \quad (6.2)$$

where X is the original data, X_{\min} and X_{\max} are the minimum and maximum value of X , and X' is the unified data corresponding to X . In this work, Equation (6.2) was utilized to unify the Cu level, temperature and stress values. The strain rate changes greatly from 0.01 to 10 s^{-1} ; therefore, the normalized value of $\dot{\epsilon}$ is too small to learn by ANN, and the following equation was adopted to unify its value [15].

$$\dot{\epsilon}' = 0.1 + 0.8 \times \left(\frac{\log \dot{\epsilon} - \log \dot{\epsilon}_{\min}}{\log \dot{\epsilon}_{\max} - \log \dot{\epsilon}_{\min}} \right) \quad (6.3)$$

The ϵ values are already in the range of 0 to 1 and therefore do not need further unification. The three layer network with one hidden layer was found to be fully sufficient for this study. To define the number of neurons in the hidden layer, mean square error (MSE) values obtained using Equation (6.4) were employed as the indices to evaluate the capability of a given network [18]:

$$MSE = \frac{1}{N} \sum_{i=1}^N [E_i - P_i]^2 \quad (6.4)$$

where E_i is the experimental value and P_i is the predicted value obtained from the ANN. N is the total number of data employed in the study. Neurons in the hidden layer were varied from 4 to 26. It was observed that a network with 20 hidden neurons gives a minimal MSE with very good correlation (Fig. 6.4).

The datasets obtained from compression tests were randomly divided into two groups: 80% of the datasets were used to train the network model (training dataset), and the remaining 20% were applied to test the model performance (test dataset). The work was accomplished by using the neural network toolbox available with MATLAB 7.6.0.324 software.

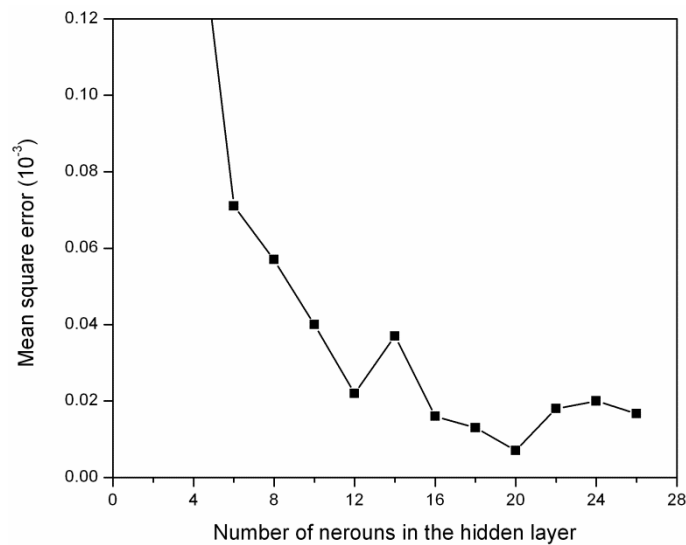


Fig. 6.4. Performance of the network with different levels of hidden neurons.

6.3.2.1 Effect of Cu addition

The ANN model was employed to evaluate the effect of Cu content on high-temperature flow behavior. Figure 6.5 shows the variations in flow stress at a true strain of 0.4 as a function of Cu content for various deformation conditions. The ANN model exhibits good tracking of the experimental data. The increase in flow stress with the addition of Cu is attributed to the solid solution strengthening effect of Cu, which is a result of interactions between the mobile dislocations and the solute atoms. The presence of Cu solutes increases the high-temperature flow stress and decreases the dynamic recovery rate due to the solute drag effect on dislocation movement [25-27]. With an increase in Cu content, the Cu solutes produced a stronger solute-drag effect and further decreased the dynamic recovery level and subsequently increased flow stress.

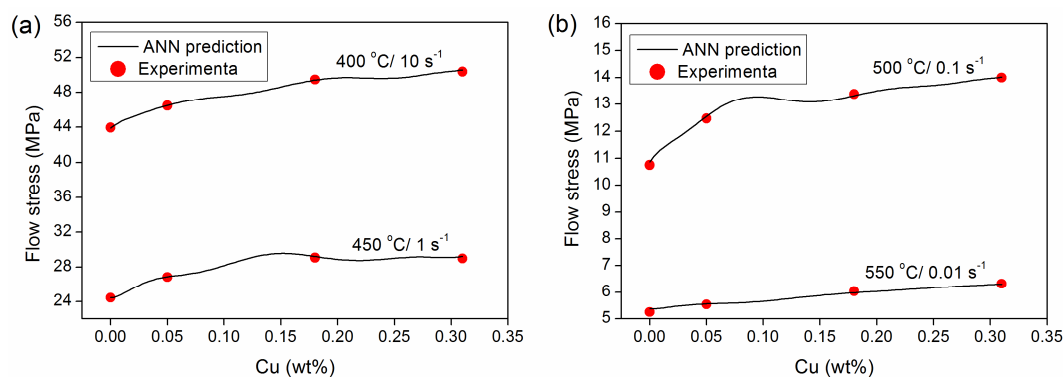


Fig. 6.5. Effect of Cu content on the flow stress at a strain of 0.4 (a) for 400 °C/10 s⁻¹ and 450 °C/1 s⁻¹ and (b) for 500 °C/0.1 s⁻¹ and 550 °C/0.01 s⁻¹.

6.3.2.2 Effect of temperature

The effects of deformation temperature on high-temperature flow behavior were simulated using the developed ANN model. Representative results are illustrated in Figure 6.6. The simulated flow stress values exhibited good agreement with the corresponding measured data for a range of strain rates and Cu contents. The flow stress decreased over the range of tested strain rates with increasing deformation temperature for all of the alloys investigated. It is well known that dynamic softening is a thermally activated process [29, 30]. Hence, as the temperature increases, the available thermal activation energy increases, which leads to a higher level of dynamic softening and a reduced flow stress.

6.3.2.3 Effect of strain rate

Figure 6.7 shows plots of σ versus $\log \dot{\epsilon}$ comparing the experimental data with the ANN predicted values at varied forming temperatures. The trained network is able to accurately predict the influence of strain rate on flow stress. Increasing the strain rate results in increased flow stress, as expected. Increasing the strain rate at a given temperature causes an increased dislocation multiplication rate and increased formation of tangled dislocation structures that act as barriers to dislocation movement. Consequently, the flow stress is augmented [29]. It worth to mention that the predicted curves in the σ -T σ - $\log \dot{\epsilon}$ plots are calculated by the developed ANN in many points between each two experimental results with interval of 5°C and 0.1 s⁻¹. Therefore, some maximum and minimum points might be appeared on the predicted curves, which are different from the curves obtained form the conventional regression methods. Due to the nature of artificial

neural network calculation and highly nonlinear relationship between the flow stress and temperature and strain rate, the developed ANN method can precisely predicted the experimental results (as showed in Fig 6.8).

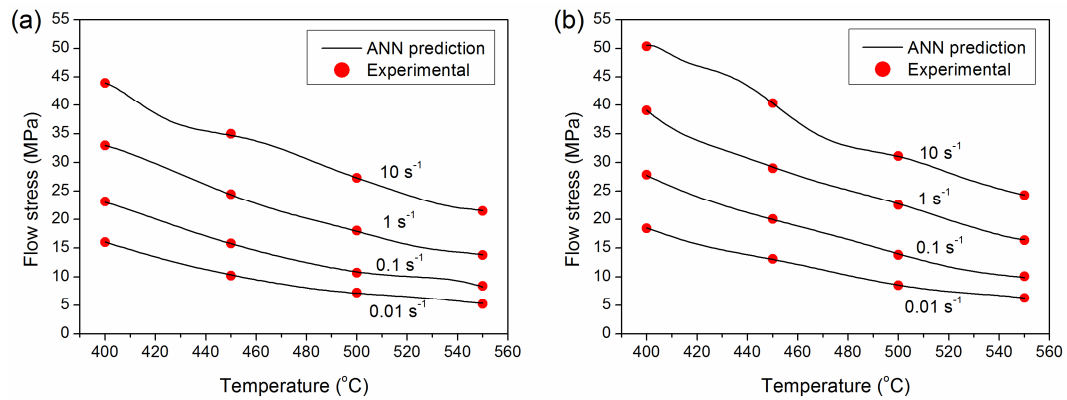


Fig. 6.6. Effect of deformation temperature on the flow stress of experimental alloys at a strain of 0.4; (a) base alloy and (b) 0.31% Cu.

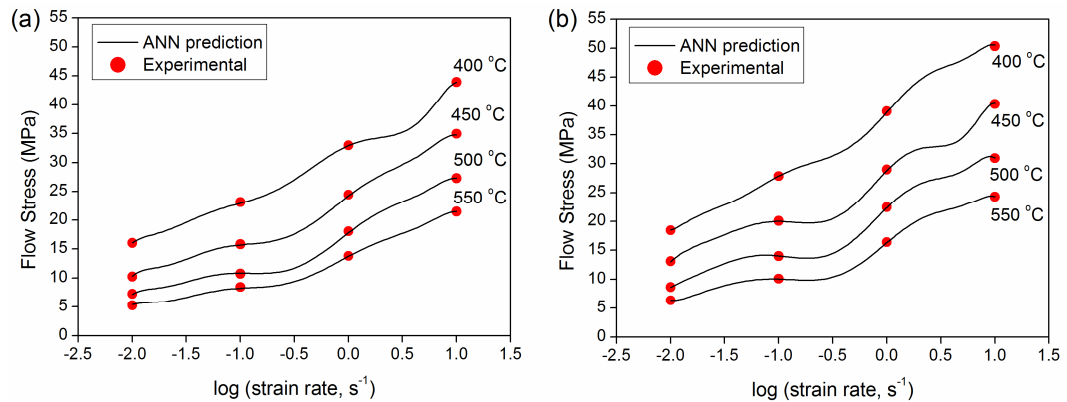


Fig. 6.7. Effect of deformation strain rate on the flow stress of experimental alloys at a strain of 0.4; (a) base alloy and (b) 0.31% Cu.

6.3.2.4 Assessment of the proposed model

The predictability of high-temperature flow stress of Al-0.12Fe-0.1Si-Cu alloys at selected deformation conditions in comparison with experimental data is illustrated in Figure 6.8. Excellent agreement was found over the full range of data that demonstrates the capability of the proposed ANN model to predict hot deformation behavior. Therefore, the model appears to offer significant potential compared to the phenomenological or analytical approaches, which are typically utilized to predict the flow behavior of a given chemical composition.

To assess the statistical significance of the model, the predictability of the proposed network was quantified in terms of correlation coefficient (R), average absolute relative error ($AARE$) and root mean square error ($RMSE$), expressed as [14, 16, 18, 28]:

$$R = \frac{\sum_{i=1}^N (E_i - \bar{E})(P_i - \bar{P})}{\sqrt{\sum_{i=1}^N (E_i - \bar{E})^2 \sum_{i=1}^N (P_i - \bar{P})^2}} \quad (6.5)$$

$$AARE(\%) = \frac{1}{N} \sum_{i=1}^N \left| \frac{E_i - P_i}{E_i} \right| \times 100 \quad (6.6)$$

$$RMSE = \sqrt{\frac{1}{N} \sum_{i=1}^N (E_i - P_i)^2} \quad (6.7)$$

where E_i and P_i have the same meaning as stated earlier; \bar{E} and \bar{P} are the mean values of E_i and P_i , respectively; and N is the total number of data employed in the study. The correlation coefficient (R) is a commonly utilized statistical parameter to examine the

strength of a linear relationship between experimental and predicted values. A higher R value does not always necessarily indicate better performance of the model, due to the tendency of a model to be biased towards higher or lower values [31]. The average absolute relative error ($AARE$) is a measure of relative overall fit and expresses the accuracy and predictability of a model[32]. This measure is easy to understand because it provides the error in terms of percentages. The root mean square error ($RMSE$) is another measure of the differences between the experimental and the predicted values[14], which has the same units as the predicted quantity (MPa, in this study). Both $AARE$ and $RMSE$ are statistical measures of a model's accuracy. The mean differences between the experimental and predicted values are computed through a term-by-term comparison and are therefore unbiased statistical parameters [32]. Lower values of $AARE$ (%) and $RMSE$ indicate stronger predictability of a model. The performance of the proposed model is reported in Table 6.2. The results obviously indicate excellent predictability and reliability of the proposed ANN model.

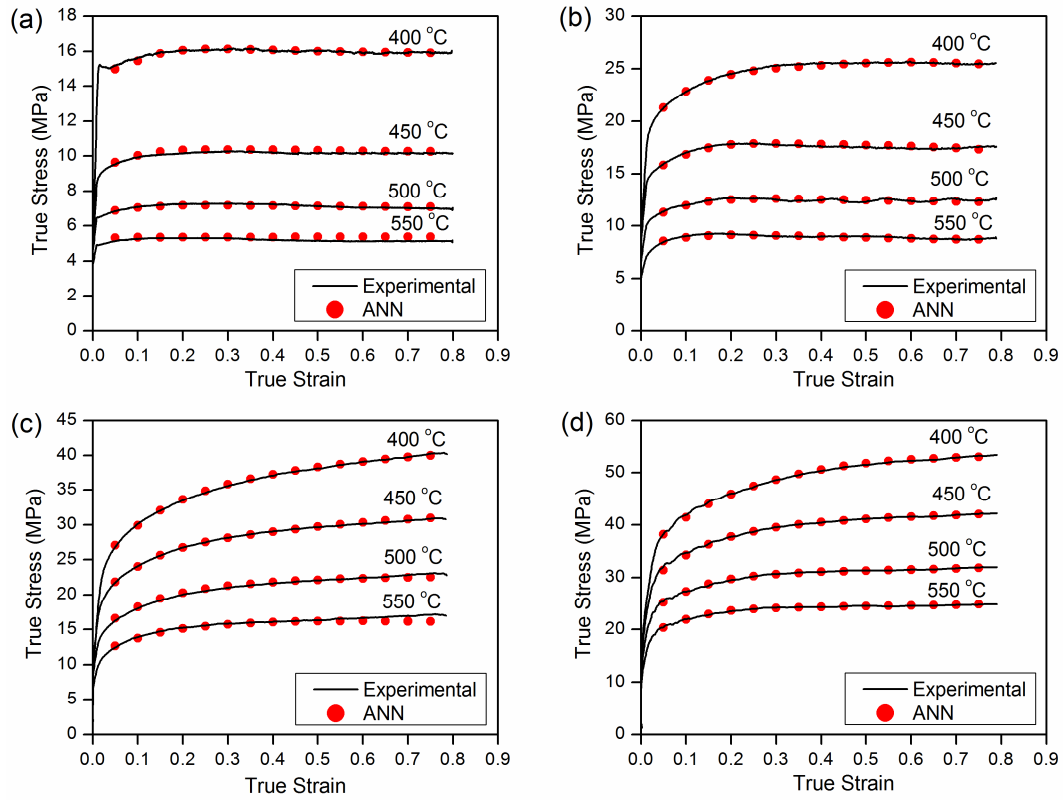


Fig. 6.8. Comparison between predicted ANN model and measured flow stress curves of (a) base alloy at $\dot{\epsilon} = 0.01 \text{ s}^{-1}$, (b) 0.05% Cu alloy at $\dot{\epsilon} = 0.1 \text{ s}^{-1}$, (c) 0.18% Cu alloy at $\dot{\epsilon} = 1 \text{ s}^{-1}$, and (d) 0.31% Cu alloy at $\dot{\epsilon} = 10 \text{ s}^{-1}$.

Table 6.2. The values of R , $AARE$ and $RMSE$ for the proposed ANN model.

Statistical index	R	$AARE$ (%)	$RMSE$ (MPa)
ANN model	0.9998	0.91	0.19

6.3.2.5 Sensitivity analysis

A sensitivity analysis was carried out to statistically assess the contributions of the input variables in the neural network. Although different methods can be used to quantify the relative importance of input parameters [33, 34], the algorithm proposed by Garson [35] is found to be the most robust method. This method includes partitioning hidden-output connection weights into components that are associated with each input neuron using absolute values of connection weights (see Appendix 6.A).

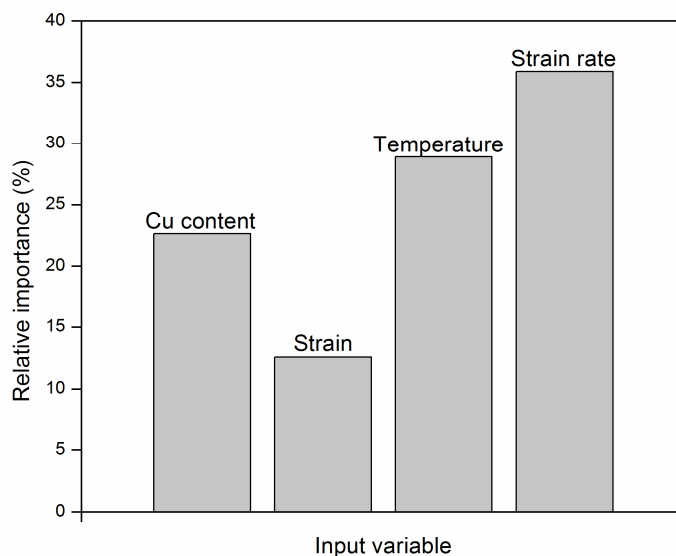


Fig. 6.9. Relative importance of individual input parameters.

Figure 6.9 shows the relative importance of Cu content and deformation parameters on the flow stress of Al-0.12Fe-0.1Si-Cu alloys. The results revealed that both the strain rate and forming temperature have the most significant effect on the flow stress of the

investigated alloys, while strain has a minimal effect. The contribution of strain arises primarily at high Z conditions where the rate of work hardening is greater than dynamic softening. At low Z conditions, the flow stress generally remained constant with changes in strain. The Cu content exhibits a moderate influence on the flow behavior of Al-0.12Fe-0.1Si-Cu alloys.

6.4 Conclusions

A set of uniaxial hot compression tests were carried out on Al-0.12Fe-0.1Si alloys with varied Cu contents at various temperatures (400–550 °C) and strain rates (0.01–10 s⁻¹). The results showed that increasing Cu content increases the flow stress over the applied range of deformation conditions due to solid solution strengthening. Based on the experimental results, a three-layer feed-forward artificial neural network model with a back-propagation learning algorithm was developed to predict the high-temperature flow behavior of the Al-0.12Fe-0.1Si-Cu alloys. It was found that the ANN model with one hidden layer consisting of 20 neurons gives the best performance. The simulated results demonstrated excellent agreement with corresponding experimental results. The predictability of the proposed model was also assessed using various standard statistical parameters. It is confirmed that the ANN model is an accurate and reliable tool to predict the high-temperature flow behavior of Al-0.12Fe-0.1Si-Cu alloys as a function of alloy composition and deformation variables. Furthermore, sensitivity analysis indicates that both the strain rate and the temperature have the most significant impact on the high-temperature flow stress, while the Cu content exhibits a moderate influence.

Appendix 6.A: Example illustrating Garson's algorithm

This example describes the procedure to determine the relative importance of input parameters using Garson's algorithm [33, 35].

As an example, consider an ANN with four input neurons, two hidden neurons and one output neuron with the connection weight as shown in Figure 6.A.1.

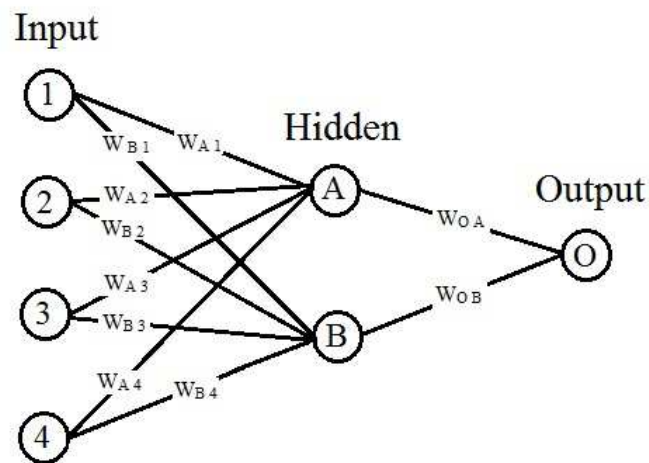


Fig.6.A.1. The structure of a 4-2-1 artificial neural network.

1) Matrix containing input-hidden and hidden-output neuron connection weights.

	Hidden A	Hidden B
Input 1	$W_{A1} = 1.40$	$W_{B1} = 0.82$
Input 2	$W_{A2} = -1.02$	$W_{B2} = 0.62$
Input 3	$W_{A3} = -2.98$	$W_{B3} = 1.04$
Input 4	$W_{A4} = 3.99$	$W_{B4} = -2.26$
Output	$W_{OA} = -3.17$	$W_{OB} = -1.21$

2) Contribution of each input neuron to the output via each hidden neuron calculated as the product of the input-hidden connection and the hidden-output connection:

e.g., $C_{A1} = W_{A1} \times W_{O_A} = 1.4 \times -3.17 = -4.44$

	Hidden A	Hidden B
Input 1	$C_{A1} = -4.44$	$C_{B1} = -0.99$
Input 2	$C_{A2} = 3.23$	$C_{B2} = -0.75$
Input 3	$C_{A3} = 9.45$	$C_{B3} = -1.26$
Input 4	$C_{A4} = 12.65$	$C_{B4} = 2.73$

3) Relative contribution of each input neuron to the outgoing signal of each hidden neuron:

e.g., $r_{A1} = |C_{A1}| / (|C_{A1}| + |C_{A2}| + |C_{A3}| + |C_{A4}|) = 4.44 / (4.44 + 3.23 + 9.45 + 12.65) = 0.15$

and sum of input neuron contributions:

e.g., $S_1 = r_{A1} + r_{B1} = 0.15 + 0.17 = 0.32$

	Hidden A	Hidden B	Sum
Input 1	$r_{A1} = 0.15$	$r_{B1} = 0.17$	$S_1 = 0.32$
Input 2	$r_{A2} = 0.11$	$r_{B2} = 0.13$	$S_2 = 0.24$
Input 3	$r_{A3} = 0.32$	$r_{B3} = 0.22$	$S_3 = 0.54$
Input 4	$r_{A4} = 0.42$	$r_{B4} = 0.48$	$S_4 = 0.9$

4) Relative importance of each input variable:

e.g., $RI_1 = S_1 / (S_1 + S_2 + S_3 + S_4) \times 100 = 0.32 / (0.32 + 0.24 + 0.54 + 0.9) \times 100 = 16\%$

	Relative importance (%)
Input 1	16
Input 2	12
Input 3	27
Input 4	45

References

- [1] J.R. Davis, Aluminum and aluminum alloys. Materials Park, OH, ASM International, 1993, pp. 59-87.
- [2] J.G. Kaufman, Introduction to aluminum alloys and tempers. Materials Park, OH, ASM International, 2000, pp. 87-118.
- [3] M. Shakiba, N. Parson, X.-G. Chen, Effect of iron and silicon content on the high-temperature flow behavior of dilute Al-Fe-Si alloys, *J. Mater. Eng. Perform.*, 2014, DOI: 10.1007/s11665-014-1302-3.
- [4] H.J. McQueen, N.D. Ryan, Constitutive analysis in hot working, *Mater. Sci. Eng. A*, 2002, 322, pp.43-63.
- [5] H.J. McQueen, E. Evangelista, N. Jin, M.E. Kassner, Energy dissipation efficiency in aluminum dependent on monotonic flow curves and dynamic recovery, *Metall. Mater. Trans. A*, 1995, 26, pp.1757-66.
- [6] J. Luo, M. Li, X. Li, Y. Shi, Constitutive model for high temperature deformation of titanium alloys using internal state variables, *Mech. Mater.*, 2010, 42, pp.157-65.
- [7] F.J. Zerilli, R.W. Armstrong, Dislocation-mechanics-based constitutive relations for material dynamics calculations, *J. Appl. Phys.*, 1987, 61, pp.1816-25.
- [8] G.Z. Voyiadjis, A.H. Almasri, A physically based constitutive model for fcc metals with applications to dynamic hardness, *Mech. Mater.*, 2008, 40, pp.549-63.
- [9] Y.C. Lin, Q.-F. Li, Y.-C. Xia, L.-T. Li, A phenomenological constitutive model for high temperature flow stress prediction of Al-Cu-Mg alloy, *Mater. Sci. Eng. A*, 2012, 534, pp.654-62.
- [10] S.B. Davenport, N.J. Silk, C.N. Sparks, C.M. Sellars, Development of constitutive equations for modelling of hot rolling, *Mater. Sci. Technol.*, 2000, 16, pp.539-46.
- [11] G.R. Johnson, W.H. Cook, A constitutive model and data for metals subjected to large strains, high strain rates and high temperatures, *Proceedings of the 7th international symposium on ballistics*, Netherlands, Hague, 1983, pp. 541-3.
- [12] Y.C. Lin, X.-M. Chen, A critical review of experimental results and constitutive descriptions for metals and alloys in hot working, *Mater. Des.*, 2011, 32, pp.1733-59.
- [13] M. Sumantra, P.V. Sivaprasad, S. Venugopal, K.P.N. Murthy, Constitutive flow behaviour of austenitic stainless steels under hot deformation: artificial neural network modelling to understand, evaluate and predict, *Model. Simul. Mater. Sci. Eng.*, 2006, 14, pp.1053-70.
- [14] S. Mandal, P.V. Sivaprasad, S. Venugopal, K.P.N. Murthy, Artificial neural network modeling to evaluate and predict the deformation behavior of stainless steel type AISI 304L during hot torsion, *Appl. Soft Comput.*, 2009, 9, pp.237-44.

- [15] N. Haghdadi, A. Zarei-Hanzaki, A.R. Khalesian, H.R. Abedi, Artificial neural network modeling to predict the hot deformation behavior of an A356 aluminum alloy, *Mater. Des.*, 2013, 49, pp.386-91.
- [16] S. Toros, F. Ozturk, Flow curve prediction of Al–Mg alloys under warm forming conditions at various strain rates by ANN, *Appl. Soft Comput.*, 2011, 11, pp.1891-8.
- [17] Y.J. Qin, Q.L. Pan, Y.B. He, W.B. Li, X.Y. Liu, X. Fan, Artificial Neural Network Modeling to Evaluate and Predict the Deformation Behavior of ZK60 Magnesium Alloy During Hot Compression, *Mater. Manuf. Process.*, 2010, 25, pp.539-45.
- [18] Y. Sun, W. Zeng, X. Ma, B. Xu, X. Liang, J. Zhang, A hybrid approach for processing parameters optimization of Ti-22Al-25Nb alloy during hot deformation using artificial neural network and genetic algorithm, *Intermetallics*, 2011, 19, pp.1014-9.
- [19] Y. Sun, W.D. Zeng, Y.Q. Zhao, Y.L. Qi, X. Ma, Y.F. Han, Development of constitutive relationship model of Ti600 alloy using artificial neural network, *Comput. Mater. Sci.*, 2010, 48, pp.686-91.
- [20] I.S. Jalham, Modeling capability of the artificial neural network (ANN) to predict the effect of the hot deformation parameters on the strength of Al-base metal matrix composites, *Compos. Sci. Technol.*, 2003, 63, pp.63-7.
- [21] H.J. McQueen, W. Blum, Dynamic recovery: sufficient mechanism in the hot deformation of Al, *Mater. Sci. Eng. A*, 2000, 290, pp.95-107.
- [22] H.J. McQueen, Metal forming: Industrial, mechanical computational and microstructural, *J. Mater. Process. Technol.*, 1993, 37, pp.3-36.
- [23] H.R. Rezaei Ashtiani, M.H. Parsa, H. Bisadi, Constitutive equations for elevated temperature flow behavior of commercial purity aluminum, *Mater. Sci. Eng. A*, 2012, 545, pp.61-7.
- [24] S. Banerjee, P.S. Robi, A. Srinivasan, L. Praveen Kumar, High temperature deformation behavior of Al–Cu–Mg alloys micro-alloyed with Sn, *Mater. Sci. Eng. A*, 2010, 527, pp.2498-503.
- [25] M. Spittel, T. Spittel. Flow stress of light metal alloys. In: H. Warlimont, editor, Part 2: Non-ferrous Alloys - Light Metals: Springer Berlin Heidelberg; 2011, pp. 19-53.
- [26] R. Le Gall, J.J. Jonas, Solute drag effects during the dynamic recrystallization of nickel, *Acta Mater.*, 1999, 47, pp.4365-74.
- [27] Ø. Ryen, B. Holmedal, O. Nijs, E. Nes, E. Sjölander, H.-E. Ekström, Strengthening mechanisms in solid solution aluminum alloys, *Metall. Mater. Trans. A*, 2006, 37, pp.1999-2006.
- [28] Z. Lu, Q. Pan, X. Liu, Y. Qin, Y. He, S. Cao, Artificial neural network prediction to the hot compressive deformation behavior of Al–Cu–Mg–Ag heat-resistant aluminum alloy, *Mech. Res. Commun.*, 2011, 38, pp.192-7.

- [29] H.J. McQueen, S. Spigarelli, M.E. Kassner, E. Evagelista, Hot deformation and processing of aluminum alloys. Florida, CRC Press, 2011.
- [30] F.J. Humphreys, M. Hatherly, Recrystallization and related annealing phenomena, Second ed. Oxford, Elsevier Ltd., 2004.
- [31] M.P. Phaniraj, A.K. Lahiri, The applicability of neural network model to predict flow stress for carbon steels, J. Mater. Process. Technol., 2003, 141, pp.219-27.
- [32] S. Srinivasulu, A. Jain, A comparative analysis of training methods for artificial neural network rainfall–runoff models, Appl. Soft Comput., 2006, 6, pp.295-306.
- [33] J.D. Olden, D.A. Jackson, Illuminating the “black box”: a randomization approach for understanding variable contributions in artificial neural networks, Ecol. Model., 2002, 154, pp.135-50.
- [34] J.D. Olden, M.K. Joy, R.G. Death, An accurate comparison of methods for quantifying variable importance in artificial neural networks using simulated data, Ecol. Model., 2004, 178, pp.389-97.
- [35] G.D. Garson, Interpreting neural network connection weights, Arti. Intel. Expert, 1991, 6, pp.46-51.

CHAPTER 7

CONCLUSIONs & RECOMMENDATIONS

CHAPTER 7

CONCLUSIONS & RECOMMENDATIONS

7.1 Conclusions

This research was carried out to study the effect of homogenization and alloying elements on the hot deformation behavior of 1xxx series aluminum alloys. The microstructural evolution of two dilute Al-Fe-Si alloys containing 0.3% Fe and either 0.1 or 0.25 % Si during homogenization was studied using optical and electron microscopy as well as electric conductivity measurements. The effect of Fe and Si contents as well as Mn and Cu minor additions on the hot deformation behavior of dilute Al-Fe-Si alloys was studied by hot compression tests conducted at various deformation temperatures and strain rates. The experimental stress-strain data were employed to drive constitutive equations correlating flow stress, deformation temperature and strain rate. Furthermore, the capability of the ANN approach to simulate the high-temperature flow behavior of dilute Al-Fe-Si alloys was examined as a function of chemical composition and process parameters. Based on the experimental data an ANN model has been developed to predict the flow behavior of Al-0.12Fe-0.1Si alloys with various levels of Cu addition (0.002-0.31 wt%) under different deformation conditions. Based on the results from Chapter 3 to Chapter 6, the following conclusions could be drawn:

Part I: Effect of homogenization treatment and silicon content on the microstructure and hot workability of dilute Al-Fe-Si alloys

- 1) The as-cast microstructures of two dilute Al-Fe-Si alloys (Al-0.3Fe-0.1Si and Al-0.3Fe-0.25Si) consisted of α -Al dendrites and metastable Al_mFe and α -AlFeSi, as well as equilibrium Al_3Fe intermetallic particles. The proportion of α -AlFeSi intermetallic increased with a higher silicon content.
- 2) Homogenization promoted the phase transformation from the metastable Al_mFe or α -AlFeSi phase to the equilibrium Al_3Fe phase via a dissolution-reprecipitation mechanism. The Al_mFe dissolved and transformed completely at 550°C in both alloys. The α -AlFeSi was transformed at 590°C in the low Si alloy (Al-0.3Fe-0.1Si), whereas it began to decompose and transform to Al_3Fe at 630°C in the high Si alloy (Al-0.3Fe-0.25Si).
- 3) Homogenization at 550°C significantly reduced the solid solution levels in both alloys due to the elimination of the supersaturation originating from the cast ingot. Above 550°C, the solid solution levels progressively increased.
- 4) The flow stress behavior of dilute Al-Fe-Si alloys was primarily controlled by the solute levels of Fe and Si. Homogenization at 550°C produced the lowest flow stress for all of the deformation conditions studied. An increase in the homogenization temperature from 550 to 630°C increased the flow stress by 10 to 23% and 15 to 45% for the low Si and high Si alloys, respectively, which is commercially significant in terms of the productivity during hot forming processes.

- 5) An increase in the silicon content from 0.10 to 0.25% in dilute Al-0.3Fe-Si alloys increased the solid solution levels for all of the homogenized conditions studied, which resulted in an increase in the overall flow stress by 4 to 11%.

Part II: Effect of iron and silicon content on the hot compressive deformation behavior of dilute Al-Fe-Si alloys.

- 1) Increasing the iron content increased the high temperature flow stress for all of the alloys studied. In the case of low Si (0.10%) alloys, increasing the iron level from 0.1 to 0.7% produced 11 to 32% increase in the flow stress over the range of deformation conditions investigated. However, for high Si (0.25%) alloys, by increasing the iron level from 0.1 to 0.5%, the flow stress increased only 4 to 16%.
- 2) The addition of silicon also increased the high-temperature flow stress. Increasing the silicon level from 0.1 to 0.25 % in the Al-0.1Fe and Al-0.5Fe alloys increased the flow stress by 4-14% and 2-8%, respectively, over the range of deformation conditions investigated.
- 3) The materials constants and activation energies for hot-deformation as a function of the Fe content were determined from the experimental compression data obtained. The applied constitutive equations yielded an excellent predication of the flow stress over wide temperature and strain-rate ranges of 1xxx alloys with various Fe and Si contents.
- 4) The activation energy for hot deformation gradually increased with increasing Fe and Si contents. Increasing the Fe content from 0.1 to 0.7% in low-Si alloys increased the activation energy from 167.2 to 181.9 kJ/mol, whereas increasing the Si level from 0.1

to 0.25% in the Al-0.1Fe-Si alloy raised the activation energy from 167.2 to 171.2 kJ/mol.

- 5) Dynamic recovery is the sole softening mechanism operating during the hot deformation of dilute Al-Fe-Si alloys. The rate of dynamic recovery increased with increasing deformation temperature and decreasing strain rate. Increasing the Fe and Si contents promoted retardation of the dynamic recovery due to the increased amounts of intermetallic particles and Si solute atoms in the aluminum matrix.
- 6) The impact of small changes in the Fe and Si contents on the flow stress and resulting extrudability of 1xxx alloys is significant, and this fact should be considered in alloy selection and design for extruded applications.

Part III: Hot deformation behavior and rate controlling mechanism in dilute Al-Fe-Si alloys with minor additions of Mn and Cu

- 1) Additions of Mn and Cu increase the flow stress of dilute Al-Fe-Si alloys for a given deformation condition. On a wt% basis, the addition of Mn has a more significant impact on the flow stress compared to Cu.
- 2) The activation energies for hot deformation increased from 161 and 176 for low-Fe and high-Fe base alloys to 181 and 192 kJ/mol for the alloys containing 0.2% Mn, respectively, while the addition of Cu up to 0.31% to the low-Fe base alloy raised the activation energy only slightly from 161 to 166 kJ/mol.
- 3) Solute-diffusion acted as the deformation rate-controlling mechanism in these dilute aluminum alloys. The hot deformation resistance is inversely proportional to the

diffusion coefficient of the solute atoms and increase with an increasing amount of the Mn and Cu solutes in the aluminum.

- 4) Additions of Mn and Cu promote the retardation of the dynamic recovery which led to a finer subgrain structure and a smaller misorientation angle after hot deformation. The addition of Mn results in a greater decrease in subgrain size and mean misorientation angle compared to the addition of Cu.

Part IV: Modeling the effects of Cu content and deformation variables on the high-temperature flow behavior of Al-Fe-Si alloys using an artificial neural network

A set of uniaxial hot compression tests were carried out on Al-0.12Fe-0.1Si alloys with varied Cu contents at various temperatures (400–550 °C) and strain rates (0.01-10 s⁻¹). The results showed that increasing Cu content increases the flow stress over the applied range of deformation conditions due to solid solution strengthening. Based on the experimental results, a three-layer feed-forward artificial neural network model with a back-propagation learning algorithm was developed to predict the high-temperature flow behavior of the Al-0.12Fe-0.1Si-Cu alloys. It was found that the ANN model with one hidden layer consisting of 20 neurons gives the best performance. The simulated results demonstrated excellent agreement with corresponding experimental results. The predictability of the proposed model was also assessed using various standard statistical parameters. It is confirmed that the ANN model is an accurate and reliable tool to predict the high-temperature flow behavior of Al-0.12Fe-0.1Si-Cu alloys as a function of alloy composition and deformation variables. Furthermore, sensitivity analysis indicates that both

the strain rate and the temperature have the most significant impact on the high-temperature flow stress, while the Cu content exhibits a moderate influence.

7.2 Recommendations

In this study the effect of homogenization conditions (temperature from 550 to 630 °C and time from 2 to 12 h) on the microstructure and hot workability of 1xxx series aluminum alloys was investigated. Moreover, the effect of main alloying contents (Fe and Si) as well as Mn and Cu minor additions was assessed on the hot workability of commercial 1xxx alloys with the long term view of optimizing alloy design for strength and hot processability. The influence of chemical composition (normally one specific alloying element such as Fe and Cu) and thermomechanical parameters on the flow stress has been modeled using the modified hyperbolic-sine constitutive equations as well as ANN. Based on the present study following recommendations can be made for future work:

1. Studying the effect of homogenization condition as well as Fe and Si contents on the static softening behavior of dilute Al-Fe-Si alloys.
2. Comparing the effect of Mn and Cu additions on the hot deformation behavior of pure aluminum (99.99%) and commercially pure aluminum to better understanding the effect of impurities on the strengthening mechanism of Mn and Cu additions.
3. Studying the effect of other alloying elements such as Mg and Ni on the hot deformation behavior of dilute Al-0.1-Fe-0.1Si alloy.

4. Modeling the combined effect of various alloying element contents (Fe, Si, Mn and Cu) as well as process variables on the flow stress and dynamic recovery behavior of 1xxx alloys using artificial neural network.